

Deformation and failure of woven and 3D composites

Citation for published version (APA):

Schormans, J. M. J. (2018). *Deformation and failure of woven and 3D composites*. Technische Universiteit Eindhoven.

Document status and date:

Published: 11/10/2018

Document Version:

Publisher's PDF, also known as Version of Record (includes final page, issue and volume numbers)

Please check the document version of this publication:

- A submitted manuscript is the version of the article upon submission and before peer-review. There can be important differences between the submitted version and the official published version of record. People interested in the research are advised to contact the author for the final version of the publication, or visit the DOI to the publisher's website.
- The final author version and the galley proof are versions of the publication after peer review.
- The final published version features the final layout of the paper including the volume, issue and page numbers.

[Link to publication](#)

General rights

Copyright and moral rights for the publications made accessible in the public portal are retained by the authors and/or other copyright owners and it is a condition of accessing publications that users recognise and abide by the legal requirements associated with these rights.

- Users may download and print one copy of any publication from the public portal for the purpose of private study or research.
- You may not further distribute the material or use it for any profit-making activity or commercial gain
- You may freely distribute the URL identifying the publication in the public portal.

If the publication is distributed under the terms of Article 25fa of the Dutch Copyright Act, indicated by the "Taverne" license above, please follow below link for the End User Agreement:

www.tue.nl/taverne

Take down policy

If you believe that this document breaches copyright please contact us at:

openaccess@tue.nl

providing details and we will investigate your claim.

Deformation and failure of woven and 3D composites

PROEFSCHRIFT

ter verkrijging van de graad van doctor aan de Technische Universiteit
Eindhoven, op gezag van de rector magnificus prof.dr.ir. F.P.T.
Baaijens, voor een commissie aangewezen door het College voor
Promoties, in het openbaar te verdedigen op donderdag 11 oktober 2018
om 11:00 uur.

Door

Jim Marcel Jan Schormans

Geboren te Heerlen

Dit proefschrift is goedgekeurd door de promotoren en de samenstelling van de promotiecommissie is als volgt:

voorzitter:	prof.dr. L.P.H. De Goey
1 ^e promotor:	prof.dr.ir. V.S. Deshpande
copromotor:	dr.ir J.J.C. Remmers
leden:	prof.dr. P.M.P.R. de Castro Carmanho (Universidade do Porto) prof.dr. S. Hallett (University of Bristol) prof.dr.ir. A.S.J. Suiker
overig lid:	prof.dr.ir. L.E. Govaert (Universiteit Twente)
adviseur:	dr. C. Ayas (Technische Universiteit Delft)

Het onderzoek of ontwerp dat in dit proefschrift wordt beschreven is uitgevoerd in overeenstemming met de TU/e Gedragscode Wetenschapsbeoefening.

© Jim Schormans, 2018

Cover photograph by Jeroen Knippenberg

A catalogue record is available from the Eindhoven University of Technology Library
ISBN: 978-90-386-4598-8

Samenvatting

Koolstofvezel versterkte kunststoffen (CFRPs) zijn composiet materialen bestaande uit koolstofvezels in een polymere matrix. CFRPs worden in toenemende mate gebruikt in lichtgewicht toepassingen vanwege hun hoge soortelijke sterkte en stijfheid. Er is een breed scala aan configuraties mogelijk wat betreft de opbouw van de CFRPs. In toenemende mate van complexiteit zijn er uni-directionele, twee dimensionaal geweven en drie dimensionaal geweven CFRPs. In dit proefschrift wordt de nadruk gelegd op dikke twee dimensionaal geweven CFRPs en drie dimensionaal niet-gevlochten orthogonaal georiënteerde (3DNOOBED) CFRPs.

Een kenmerkende eigenschap van dikke composieten is dat falen veroorzaakt wordt door materiaal falen, en niet door structureel falen zoals bijvoorbeeld knik. De vorming van knik banen in de microstructuur wordt geacht het meest dominante faal mechanisme te zijn. Knik banen ontstaan bij compressieve belastingen, als de polymere matrix tussen de vezels gaat vloeien. De vezels kunnen dan gaan roteren, waarna zij uiteindelijk zullen breken.

Het voornaamste doel van dit proefschrift is de ontwikkeling van numerieke modellen die in staat zijn het compressieve falen van dikke composieten te voorspellen. Met dit doel worden ten eerste 2D-geweven composieten gemodelleerd op de schaal waar de knik banen ontstaan: de micro schaal. Een model op de micro schaal wordt gepresenteerd waarin individuele koolstofvezels worden gemodelleerd. Omdat het model gebruik maakt van isotrope vezels en een elastisch-perfect-plastische polymere matrix, is dit model in staat een gedetailleerd beeld te vormen van het ontstaan en de groei van knik banen. Het model wordt vervolgens gebruikt om parameter studies uit te voeren om zo doende de eigenschappen te identificeren die de grootste invloed hebben op de sterkte en stijfheid van het composiet. Een voorbeeld van de bestudeerde parameters is de fase verschuiving tussen lagen in het laminaat.

Een meso scopische homogenisatie aanpak, gebaseerd op Hill's anisotropisch plasticiteits model, is vervolgens ontwikkeld om de vezels en de polymere matrix te homogeniseren in een enkel constitutief model voor de vezel bundels. Als gevolg van de homogenisatie, gaat de geometrie van de individuele vezels verloren, en daardoor de buig effecten van de vezels. De grote van de knik baan, die nu afhangt van discretisatie gebruikt voor de eindige elementen methode, wordt gecalibreerd aan de hand van een simulatie op de micro schaal. Aangezien de homogenisatie van de vezelbundels impliceert dat het volstaat om individuele vezelbundels te modelleren, is de vereiste rekenkracht aanzienlijk minder. De methode kan nu toegepast worden in drie dimensionale simulaties op een coupon schaal. Hiervan gebruik makende, worden compressie testen op doorboorde coupons van weefsels met een platbinding gesimuleerd. De simulaties geven aan dat twee dimensionaal geweven composieten relatief ongevoelig zijn

voor de grootte van gaten in de coupon en dat de lengteschaal geïntroduceerd door de afmetingen van de vezelbundels geen invloed heeft op gevoeligheid van de sterkte ten opzichte van het gat. De reden dat twee dimensionaal geweven composieten met een platbinding relatief ongevoelig zijn voor de grootte van een gat, is dat er een plastisch vervormde zone ontstaat aan de rand van het gat. De plastische zone heeft een splijtende werking en verlicht de spannings concentratie.

De voor het compressieve falen ontwikkelde homogenisatie methode van vezelbundels wordt ook getest voor andere belastingen. In tegenstelling tot compressieve belastingen, waarbij de deformaties buiten de geknikte zones klein blijven, kunnen de deformaties en rotaties onder andere belastingen groot zijn.

Onder trekbelastingen hebben de vezelbundels de neiging om te strekken, wat grote lokale rotaties in de vezelbundels ten gevolge heeft. Aangezien de homogenisatie gebaseerd op Hill plasticiteit de structuur van de vezelbundels niet in acht neemt, wordt deze rotatie niet goed beschreven en wordt de methode onnauwkeurig. Op eenzelfde manier als de methode gebaseerd op Hill plasticiteit, worden de buig effecten van de vezels verwaarloosd in model gebaseerd op kristal plasticiteit. Echter, in tegenstelling totz de aanpak gebaseerd op Hill plasticiteit, is het in een model dat gebruikt maakt van kristal plasticiteit wel mogelijk om de structuur van een vezelbundel te beschrijven. De gepresenteerde homogenisatie van vezelbundels op basis van kristal plasticiteit is wel in staat lokale rotaties van vezels te beschrijven.

In het tweede deel van het proefschrift wordt de homogenisatie aanpak gebaseerd op kristal plasticiteit gebruikt om het falen van 3DNOOBED composieten onder afschuiving en compressie te simuleren. Vanwege de structuur van de vezelbundels in de 3DNOOBED composieten, is het beschrijven van de structuur van de vezelbundels van vitaal belang om de spanning-rek karakteristieken van het materiaal nauwkeurig te bepalen en te vergelijken met experimenteel verkregen waarden. Het modelleren van de structuur van de vezelbundels is nodig, aangezien deze strijdige faalmechanismen veroorzaken die tot een opbouw van hydrostatische spanningen leiden.

Het faalgedrag van 3DNOOBED monsters belast onder afschuiving kan met een grotere nauwkeurigheid worden voorspeld dan het faalgedrag van monsters die worden gecompriëerd. De compressieve sterkte en stijfheid van 3DNOOBED monsters is sterk afhankelijk van imperfecties in de vezelbundels op de micro schaal. De golving van de vezels in de bundels wordt niet gemodelleerd, terwijl deze een significante invloed heeft op de sterkte en stijfheid van monsters.

Abstract

Carbon fiber reinforced plastics (CFRPs) are composite materials that consist of carbon fibers in a polymer matrix. CFRPs are increasingly used in light weight applications due to their high specific strength and stiffness. Many different configurations of CFRPs are possible, ranging from uni-directional CFRPs, to 3D woven CFRPs. In this work the emphasis is on the failure properties of thick, 2D woven and 3D non-interlacing orthogonally orienting & binding (3DNOOBED) composites.

A characteristic of *thick* composites is that they fail due to *material* failure in stead of *structural* failure, i.e. buckling. The most dominant failure mechanism in thick composites is considered to be the formation of kink-bands. Kink-bands originate under compressive loading when the polymer in between the fibers start to yield. The fibers start to rotate and eventually they fracture.

The main goal of this thesis is to develop numerical models that are able to predict the compressive failure behavior of thick composite materials. First, kink-bands in a 2D plain weave geometry are modeled at the scale where the kink-bands originate and develop: the micro-scale. A micro-scale plane strain model is made where individual fibers in the warp tow are modeled. Using isotropic fibers and an elastic perfectly-plastic matrix, this type of model is capable of describing the formation and growth of a kink-band in detail. The model is then used to perform parameter studies to identify the properties that determine the compressive strength of a woven composite. Among other parameters, the effect of phase shifts between the layers of a laminate on the compressive strength and stiffness is studied.

A meso-scale homogenization scheme based on Hill anisotropic plasticity is developed to homogenize the fibers and the matrix into a single constitutive model for the tows. As a result of the homogenization, the geometry and therefore bending effects of individual fibers are lost. The mesh-dependent magnitude of the kink-bands is calibrated using the micro-scale simulations. As the homogenization implies that individual tows need to be modeled in stead of individual fibers, the computational costs are reduced significantly. In fact, it allows to perform 3D simulations on a coupon level. Open hole compression simulations are performed on a plain weave geometry. The simulations indicate that 2D woven composites are relatively notch insensitive and that the length scale introduced by the tow does not have an effect on the notch sensitivity. The reason that 2D plain woven composites are relatively notch insensitive, is that the plasticity that originates near the hole acts as a splitting mechanism, alleviating the stress concentration.

The homogenization scheme developed for the simulation of the compressive failure in 2D woven composites is also tested under other loading conditions. In contrast to the compressive load case, where deformations outside of the kinked regions remain

small, deformations and rotation may be large in other load cases. Under tensile loading, tows in woven composites tend to stretch, causing large local rotations in the tows. As the Hill plasticity based tow-level homogenization does not take into account the texture of the fibers in a tow, this rotation is not well captured and the method becomes inaccurate. Similar to the Hill plasticity based homogenization scheme, a Crystal Plasticity model does not include fiber bending effects. However, in contrast to the Hill plasticity based tow-level homogenization, a Crystal Plasticity model is able to take a description into account of the texture of the fibers in the tows. The Crystal Plasticity based tow-level homogenization describes the stretching of a tow in tension, and the local material rotations accurately.

In the second part of the thesis, the tow-level homogenization based on Crystal Plasticity is used to simulate shear and compressive failure experiments of 3DNOOBED composites. Due to the way the tows are organized in a 3DNOOBED composite, capturing the texture of individual tows is vital in accurately predicting the stress-strain response as observed in experiments. The modeling of the texture of the fibers in the tows is necessary as they cause incompatible failure modes which in turn lead to the buildup of hydrostatic pressure in the material.

The failure of 3DNOOBED specimens loaded in shear is predicted with more accuracy than the failure under compressive loading. The compressive strength and stiffness of the 3DNOOBED samples is highly dependent on imperfections present in the tows on the micro-scale. The waviness of the fibers is not modeled explicitly, whilst it is a dominant parameter in determining the compressive strength and stiffness of a sample.

Contents

Abstract	iii
1 Introduction	1
1.1 Design strategies	2
1.2 Goal of this research	3
1.3 Approach and structure of the Thesis	3
2 A micro-scale model to study the compressive strength of woven carbon-fiber reinforced plastics	5
2.1 Introduction	5
2.2 Method	7
2.3 Results	10
2.4 Discussion	18
2.5 Conclusion	20
3 Notch sensitivity in woven carbon-fiber reinforced plastics	21
3.1 Introduction	21
3.2 Methods	23
3.3 Results	27
3.4 Discussion	30
3.5 Conclusion	33
4 Application of the meso-scale model to tensile failure	35
4.1 Plain weave model	35
4.2 Tensile loading with Hill plasticity	35
4.3 Crystal plasticity	38
4.4 Tensile loading with Crystal Plasticity	39
4.5 Conclusion	40
5 Shear failure in 3D non-woven carbon fibre composites	43
5.1 Introduction	43
5.2 Experiments	45
5.3 Computational modeling	55
5.4 Numerical results	61
5.5 Implications for Homogenized Models	68
5.6 Summary	69

6	On the enhanced ductility of 3DNOOBED composites under compressive loadings	71
6.1	Fabrication and Microstructure	71
6.2	Experimental methods	72
6.3	Computational modeling	76
6.4	Simulation results	82
6.5	Kink-bands	89
6.6	Conclusion	90
7	Conclusions and recommendations	91
7.1	Conclusion	91
7.2	Recommendations	92
A	3DNOOBED shear sensitivities	95
B	Quantifying waviness	97
	Acknowledgements	108

Chapter 1

Introduction

Structural carbon fibers were invented in the 1960s and are often used in combination with a polymer matrix to form carbon fiber reinforced plastics (CFRPs). CFRPs are increasingly used in engineering applications. Due to their high specific strength and stiffness they are an excellent candidate for lightweight applications such as aerospace and automotive components.

Traditionally, CFRP components are manufactured using a layered approach. Multiple layers, or plies, are stacked to optimize the mechanical properties of the component. The carbon fibers can be placed in the ply in different configurations. The most basic one is a uni-directional (UD) configuration as shown in Figure 1.1a. A UD is a thin sheet, typically around 0.1 mm thick, where all fibers are oriented in the same direction. As a result, these plies offer extremely good mechanical properties such as strength and stiffness in the fiber direction, but are relatively weak and compliant in the direction transverse to the fiber orientation and in the in-plane shear direction.

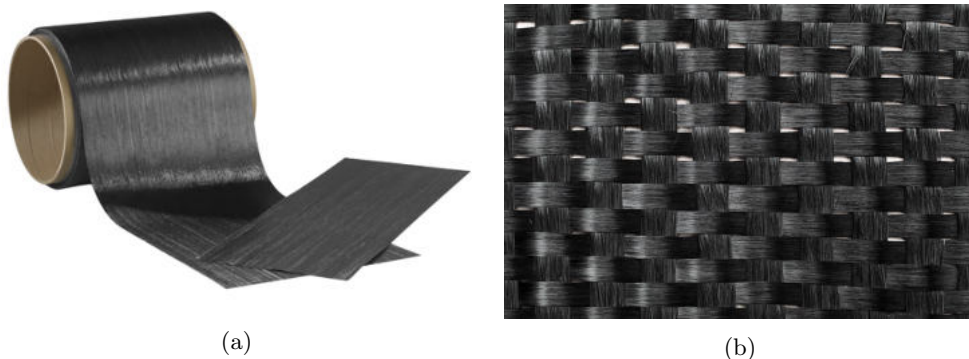


Figure 1.1: Examples of a UD and woven architectures. A tape of UD material can be seen in (a) and a woven configuration can be seen in (b).

To increase these in-plane transverse mechanical properties, textile configurations can be used. In textile configurations, fiber bundles, called tows, are woven in two principal directions. The tows, often denoted as warp and weft tows, can contain different numbers of fibers in the different directions. In addition, different weave patterns can be used to control the mechanical properties in both weave and weft

direction such as plain, twill and satin weaves. If an equal amount of fibers are placed in each direction, the fabric is called a balanced weave. An example of a balanced twill weave is shown in Figure 1.1b.

Obviously, the stiffness of CFRPs is largely determined by the number of fibers in the two directions. A prediction of the strength of the ply under different loading conditions is less straight forward. Failure in composite materials is a complex series of different mechanisms on the microscale, such as fiber breakage, matrix cracking, fiber debonding and fiber kinking. Depending on the properties of the fibers and the matrix material, the fiber architecture and the stress state, a combination of these mechanisms will ultimately lead to failure of the ply.

An additional failure mechanism is introduced by stacking several plies into a single laminate. As the connection between the plies is the relatively weak matrix, it can fail and cause the plies to delaminate. One way to prevent this delamination, is to use a 3D weaving technique. In 3D weaving, tows are also applied in the out of plane direction. Similar to the difference between UD and textile composites, 3D woven CFRPs are more resistant to delamination, but the in plane mechanical properties are lower as there are less fibers placed in the planes, as shown in Figure 1.2.

Due to a constant improvement of weave architectures, 3D composites are increasingly used. A wide range of 3D architectures have been created, including braided tubes and nozzles, multilayer woven sheets and beams and flanges with complex cross sections. 3D composites have additionally been found to show novel mechanical properties, including enhanced damage tolerance, resistance to compressive micro-buckling failure, and the capacity for large ductility and energy absorption.

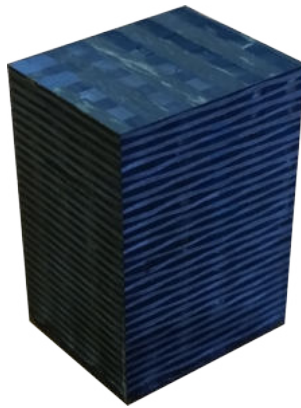


Figure 1.2: Example of a thick 3D texture: a 3D Non-interlacing Orthogonally Orienting & Binding (3DNOOBED) composite.

1.1 Design strategies

Designing efficient structural components made of CFRP is a difficult task as the design limits are often not exactly known. In order to arrive at a lightweight, but strong and stiff structure, the failure behavior must be known exactly. As a result, a large experimental program, in combination with a numerical study is needed. Such a program is often denoted as the Design Pyramid [1], as illustrated in Figure 1.3.

The design pyramid consists of several levels of testing. At the bottom, material sam-

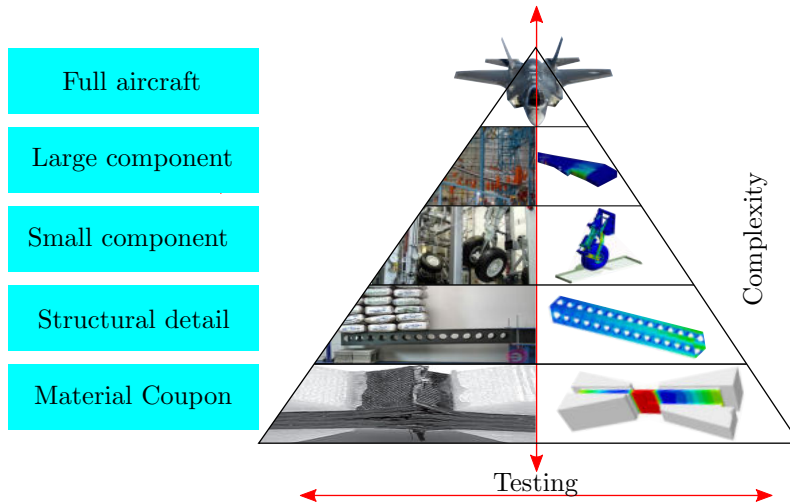


Figure 1.3: A representation of the pyramid shaped design approach used in aerospace engineering [1].

ples (coupons) are tested to obtain a material chart containing the elastic mechanical properties as well as the failure behavior. One level higher, small geometric features such as cut-outs and notches are introduced. The geometric features are more present on higher levels and at the top of the pyramid, a complete airplane is tested.

Due to large number of combinations in layups, i.e. the number and order of the stacked plies in a laminate, the number of experiments can become extremely large. In order to prevent a costly and time consuming testing programs, a number of experiments can be replaced by numerical tests. Obviously, this demands numerical models with excellent predictive capabilities.

1.2 Goal of this research

The goal of this research is to develop numerical techniques that are able to accurately predict the failure behavior of CFRP materials under complex stress states. In particular, the emphasis is on the understanding and the prediction of the failure mechanisms under a compressive load, as this is a mechanism that is less understood. The numerical framework that will be developed is not restricted to the case of compressive load or thick textile composites. It will be tailored to be used for shear failure in 3D composites as well.

1.3 Approach and structure of the Thesis

To be able to accurately predict macroscopic failure of CFRPs, an understanding of the mechanisms on the micro-scale is required. The dominant failure mechanism in composites under compressive loading has been identified to be fiber kinking [2].

In the Chapter 2, a micro-scale model for woven composites is presented in which individual fibers are modeled. In this way, the exact fiber kinking mechanism is captured accurately. A downside of this approach is that the model is restricted to two dimensions. The model is used to perform parameter studies that help to understand the formation of kink bands and parameters that affect the formation of kink bands.

In order to be able to analyze large structural components, a meso-scale model is presented in Chapter 3, in which the fibers in the tows, are homogenized using a volume averaging criterion [3]. The model, which now allows for large three dimensional analyses, is used to study the effects of notches in the compressive strength of woven layered composite materials. In Chapter 4 the models are used to study the failure mechanisms under different loading conditions, which give rise to an alternative homogenization strategy, based on a crystal plasticity model.

In Chapters 5 and 6 the models are used to study shear and compressive failure in a 3DNOBED material [4, 5]. The performance of both the Hill and the crystal plasticity model is compared with experiments. The Thesis is concluded in Chapter 7 with a summary of the conclusions. A list of recommendations for further research is presented to finalize the thesis.

Chapter 2

A micro-scale model to study the compressive strength of woven carbon-fiber reinforced plastics

The following chapter is based on the paper: "A micro-scale model to study the compressive strength of woven carbon-fiber reinforced plastics". A micro-scale plane strain model is presented that is used to simulate the formation of kink-bands in a plain weave CFRP. The emphasis is put on establishing relations between constitutive and geometric properties and the compressive strength of a laminate.

2.1 Introduction

Composite materials are increasingly being used in applications requiring thick components, such as drag braces for landing gears. As opposed to thin-walled structures, where structural buckling is the major failure mechanism under compressive and shear loadings, thick composite structures suffer from *material* failure under these loading conditions. The optimization of thick structural parts made out of woven carbon-fiber-reinforced laminates therefore relies on the in depth knowledge of the failure mechanisms of the material, for various loading states and combinations thereof: the complex loading states.

Traditionally, much research has been focused on the prediction of failure of composites loaded in tension [6, 7, 8]. The strength of the material under compression, however, is investigated to a lesser extent. Here, three main failure mechanisms have been identified: (i) kink-band formation, (ii) intra-ply cracking and (iii) inter-ply cracking [9]. Generally, kink-band formation is considered the most dominant failure mechanisms of thick walled carbon-fiber-reinforced structures under compression [2]. On the micro-scale, the formation of kink bands in unidirectional laminates has been studied extensively [10, 11, 12, 13].

In an analytical study, Rosen [14] studied the compressive failure stress of a unidirectional composite under the assumption that the material fails due to elastic buck-

ling. In contrast to this, Argon [15] proposed that failure is a result of plastic microbuckling. Budiansky and Fleck [16, 17] extended the plastic microbuckling analysis for UD composites with the assumption of an elasto-perfectly plastic matrix and derived the kinking stress:

$$\sigma_{\text{kink}} = \frac{\tau_y}{\frac{\tau_y}{G} + \bar{\phi}}, \quad (2.1)$$

where τ_y is the composite shear strength, G is the effective laminate shear modulus and $\bar{\phi}$ is the misalignment of the fiber with the loading direction.

In addition to the analytical modeling of kink bands, several numerical analyses using finite element models have been performed on unidirectional composites. Kyriakides et al. [18] showed that the shear deformation of the matrix in between the fibers allows the bending of the fibers and therefore the formation of a kink band. Pimenta et al. [19] explored several constitutive laws for the matrix and stated that a elastic-perfectly-plastic constitutive law proved to be sufficient for an accurate modeling of kink bands. Vogler and Kyriakides [20] conducted an experimental study on unidirectional plates of AS4/PEEK using a custom testing device. These experiments were later analyzed using two- and three-dimensional micromechanical models by Vogler et al. [21], who concluded that the predicted characteristics of the resulting kink bands are similar. Recently, Altman et al. [22] used a continuum damage model to predict the influence of ply waviness on stiffness and strength in ultra-thick uni-directional composites.

Although the evolution of kink bands in *unidirectional* composites has been studied widely, research on the compressive failure due to the evolution of kink bands in composites where the fiber bundles are *undulated*, such as in woven or textile composites, is less abundant. Experiments visualizing kink-band formation in textile composites have been performed by e.g. Reifsnider et al. [23] and Karayaka et al. [24]. As textile composites have a more complex structure than unidirectional composites, the effect of the tow-scale structure on the mechanical properties is an ongoing topic of research. An example of a mechanism introduced by the tow-scale structure of textiles is layer nesting, which has been studied by Breiling and Adams [25] and Hale and Villa [26]. Furthermore, De Carvalho et al. [27] conducted an experimental investigation into the compressive failure of orthogonal two-dimensional woven composites and showed that the phase differences between layers in the laminate can have a significant effect on the damage mechanisms.

Within the literature, several analytical models can be found which take into account the meso-scale structure of textile composites. Ishihikawa and Chou [28] used models based on classical laminate theory to study different types of weaves. Tan et al. [29] modeled plain weave composites using a sinusoidal beam model and more recently, De Carvalho et al. [30] used a model based on a beam supported by an elastic foundation to study the tensile and compressive response of woven composites up to failure.

When modeling textile composites using finite elements, meso-scale unit cells are often used to describe the composite on a tow-scale. A road map to create such unit cells was presented by Lomov et al. [31]. Whitcomb and Tang [32, 33] used a unit cell finite element model to study different variation of weaves to identify dominant characteristics of the weaves. Kollegal and Sridharan [34] used a finite element analysis in conjunction with a micro-mechanical model to study dominant modes of failure under in-plane tension, compression and shear and Zako et al. [35] used unit-cell

model in cooperation with an anisotropic damage model based on damage mechanics to study tensile failure in plain weaves. The effect of phase shifts between layers in a laminate was also studied numerically using unit cells by Huang [36].

A downside of modeling on the meso-scale with homogenized tow models is that the geometry of the individual fibers is lost and therefore the formation of kink bands is difficult to study. The goal of this Chapter is to determine which weave properties, and under what circumstances, influence the development of kink bands and therefore have the most significant effect on the compressive strength and stiffness of a laminate. To do so, we present a micro-mechanical finite element model of a woven carbon-fiber laminate that can be used to simulate kink-band formation in woven composites. The model is used to investigate the effect of phase differences between layers as well as several laminate properties such as the fiber-volume fraction of the laminate.

The Chapter starts with a presentation of the micro-scale model in Section 2. The compressive failure mechanism is shown in Section 2.3.1 . The model is used to investigate the effect of phase shifts in Section 2.3.2 and several laminate properties in Section 2.3.3. The results of these simulations are discussed in Section 2.4.

2.2 Method

In the spirit of the simulations performed by Kyriakides et al. [18], a micro-scale model has been created where every fiber is modeled individually. In order to keep the computational costs at an acceptable level, a two-dimensional model of the warp direction is developed. For a unidirectional compression test, plane strain conditions are assumed in the weft direction. The main features of the model are explained in the next Section. First, the geometry of the model is presented along with its modifiable parameters after which the constitutive modeling of the fibers and the matrix is addressed.

2.2.1 Geometry and boundary conditions

Consider the two-dimensional representation of a woven composite as shown in Figure 2.1. The undulating warp tows are in-plane and are depicted with the dark gray color. The weft tows undulate in the out-of-plane direction and are colored white. The space in between the warp and weft tows is filled with matrix which is colored light grey in Figure 2.1. The warp fiber bundles are assumed to undulate periodically. As a result, the model can be divided into a number of similar unit cells. Such a unit cell is indicated with the red square in Figure 2.1. The parameters that define the

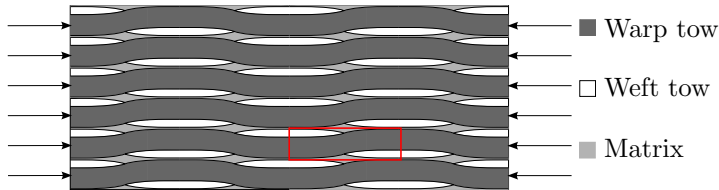


Figure 2.1: Two dimensional representation of a woven composite under a compressive loading indicated by the arrows. The red rectangle marks the unit cell chosen for this laminate. A detailed geometry is shown in Figure. 2.2

geometry of the unit cell are indicated in Figure 2.2. The unit cell consists of half a wavelength λ in the warp direction. Each fiber in the tow, with a thickness t_f , is modeled separately. The tow consists of n uniformly spaced fibers. The fiber spacing t_m is filled with the pure matrix material. The thickness of the matrix layer t_m is related to the fiber thickness t_f through the volume fraction V_{ft} in the tow:

$$t_m = \frac{t_f}{V_{ft}} - t_f. \quad (2.2)$$

The area of the warp tow A_{warp} is determined by taking the area of n fibers and matrix layers. The warp tow undulates over weft tows with an angle θ . The fibers in the weft tows do not play a role in the kinking behavior. Therefore, in order to reduce the complexity of the model, the fibers in the weft tows (hashed) of thickness t_w and surface area A_{weft} are modeled as an isotropic elasto-plastic continuum with homogenized properties. The pocket of matrix between the tows of different layers

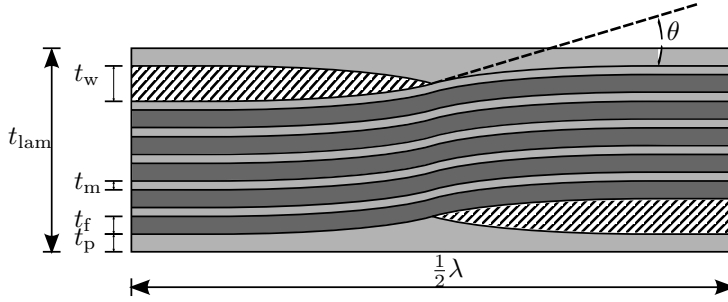


Figure 2.2: Overview of key parameters in the woven unit cell consisting of weft tows (hashed), $n = 5$ fibers (dark grey) and matrix (grey). For illustration purposes, the fibers and the matrix layers in between the fibers have not been drawn to scale with respect to the rest of the model.

has thickness t_p and surface area A_{pocket} . The total height t_{lam} of the model unit cell is then equal to:

$$t_{lam} = t_w + 2t_p + n(t_f + t_m). \quad (2.3)$$

With the areas of the warp tow, weft tow and matrix pockets determined, the laminate fiber volume fraction V_{fl} can be related to the tow volume fraction V_f :

$$V_{fl} = \frac{V_f(A_{warp} + A_{weft})}{A_{warp} + A_{weft} + A_{pocket}}. \quad (2.4)$$

The entire model is meshed with 8-node quadratic hexagonal generalized plane strain elements in the commercial software package ABAQUS[®]. In order to accurately capture the bending of the fibers, each fiber is modeled with three elements in the fiber thickness direction.

Cross-sections of multi-layer composites can be modeled by stacking and mirroring this unit cell. Additionally, the phase between the stacked layers can be varied proportionally to the wavelength λ . Let k be the number of unit cells in the warp direction and l the number of stacked layers. The model in Figure 2.3 can then be identified as a $k \times l$ model where $k = 2$ and $l = 3$.

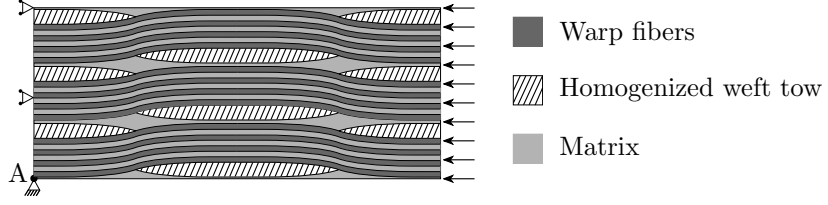


Figure 2.3: Overview of a $k \times l$ model with $k = 2$ and $l = 3$ along with the applied boundary conditions. Note that only a few warp fibers have been drawn for illustrative purposes.

In all simulations presented in this work the left edge of the model is constrained in the warp direction and the displacement of the right edge is prescribed. The bottom left node of the model located at point A in Figure 2.3 is constrained in the stacking direction to prevent rigid body motion. The top and the bottom edges of the laminate are not constrained.

2.2.2 Constitutive modeling

The mechanical properties of the carbon fibers and the matrix are similar to those used by Kyriakides et al. [18]. The carbon fibers are isotropic-elastic with a Young's modulus $E_f = 214 \cdot 10^3$ MPa and a Poisson's ratio of $\nu_f = 0.263$. The matrix is considered to be an isotropic elasto-plastic medium having an Young's modulus of $E_m = 6140$ MPa, a Poisson's ratio of $\nu_m = 0.356$. A perfect plastic material behavior with a yield stress of $\sigma_m^{y0} = 82.1$ MPa is assumed. In order to increase the stability of the simulations, a small isotropic hardening is added, according to the following strain hardening relation:

$$\sigma_m^y = \sigma_m^{y0} + H\epsilon_p, \quad (2.5)$$

where σ^y is the current yield stress, ϵ_p is the accumulated plastic strain. The hardening modulus H has been set to 10 MPa in order to avoid numerical instabilities.

The homogenized elastic properties of the weft tow are calculated using the Reuss bound:

$$\frac{1}{E_w} = \frac{V_f}{E_f} + \frac{1 - V_f}{E_m}, \quad (2.6)$$

where V_f is the fiber volume fraction in the weft tow, which is taken to be 67%. The Poisson ratio and the elasto-plastic properties of the weft tow are assumed to be equal to the matrix properties:

$$\nu_{we} = \nu_m, \quad (2.7)$$

$$\sigma_{we}^y = \sigma_{we}^{y0} + H\epsilon_p, \quad (2.8)$$

respectively. The yield stress of the weft tow σ_{we}^{y0} is updated in the same way as the yield stress of the matrix. The initial yield stress of the weft tow σ_{we}^{y0} is equal to the initial yield stress of the matrix σ_m^{y0} .

The models are created using ABAQUS[®] Standard. Large strain kinematics are assumed and the model the system of equations is solved using the Riks arc length solver.

2.3 Results

The results of uni-axial compression tests are presented in this section. First, the compressive failure mechanism is identified and the dependency of the peak compressive strength and the stiffness on the size of the model is investigated. Secondly, simulations with shifted phases are presented. The section is concluded by means of a number of parameter studies.

2.3.1 Compressive failure mechanism

In order to have a baseline result, the model is used to analyze a laminate with $k = 2$, in which all the warp tows undulate in phase. In order to reduce the boundary effects to a minimum, the number of layers stacked on top of each other is set to $l = 3$ as shown in Figure 2.4a. The load displacement curve of this analysis is shown in Figure 2.4b.

The compressive stresses are calculated by dividing the reaction forces of the nodes on the right boundary by the surface of the right boundary. As the model has unit thickness in the out of plane direction, the surface of the boundary is equal to the total thickness of the laminate t_{lam} defined in (2.3). For the configuration presented, the failure load is equal to $F/A_0 = 263$ MPa, which is the peak in the load displacement curve. The compressive stiffness is evaluated in the linear regime and has a value of $E = 7872$ MPa.

When looking at the micro-scale failure mechanism in the model, it can be concluded that these mechanisms are similar to the mechanism presented by Kyriakides et al. [18] and Pimenta et al. [37]. The matrix yields and the plasticity of the matrix allows the fibers to bend. This process is illustrated in Figure 2.4. The plastic deformation originates in the matrix material between the fibers inside a tow, see Figure 2.4c. At this point, the laminate is still capable of sustaining additional load. The amount of matrix material undergoing plastic deformation increases until the maximum load is reached. The plastic deformation at the maximum load can be seen in Figure 2.4d. A further increase of the compressive strain results in a larger rotation of the fibers and an increase in plastic deformation of the matrix material, which can be seen in Figure 2.4e.

In order to investigate the effect the model size has on the resulting stiffness and strength, a number of simulations are performed with various model sizes. Figure 2.5 shows the compressive stiffness and compressive strength calculated using models with different number of cells in the warp and thickness directions. The size of the model is indicated on the horizontal axis with $k \times l$ cells. The baseline simulation shows the kinking mechanism and the evolution of a kink band. Increasing the number of cells in the warp direction, k , does not affect the peak compressive strength of the composite. Increasing the number of stacked layers, l , does influence the strength of the laminate slightly. The strength converges to a single value if the number of stacked layers is increased. As the difference in peak strength is relatively small, the remainder of the simulations in this Chapter will be simulated with a model with $k = 2$ cells in the warp direction and $l = 5$ layers stacked on top of each other in order to reduce computational costs.

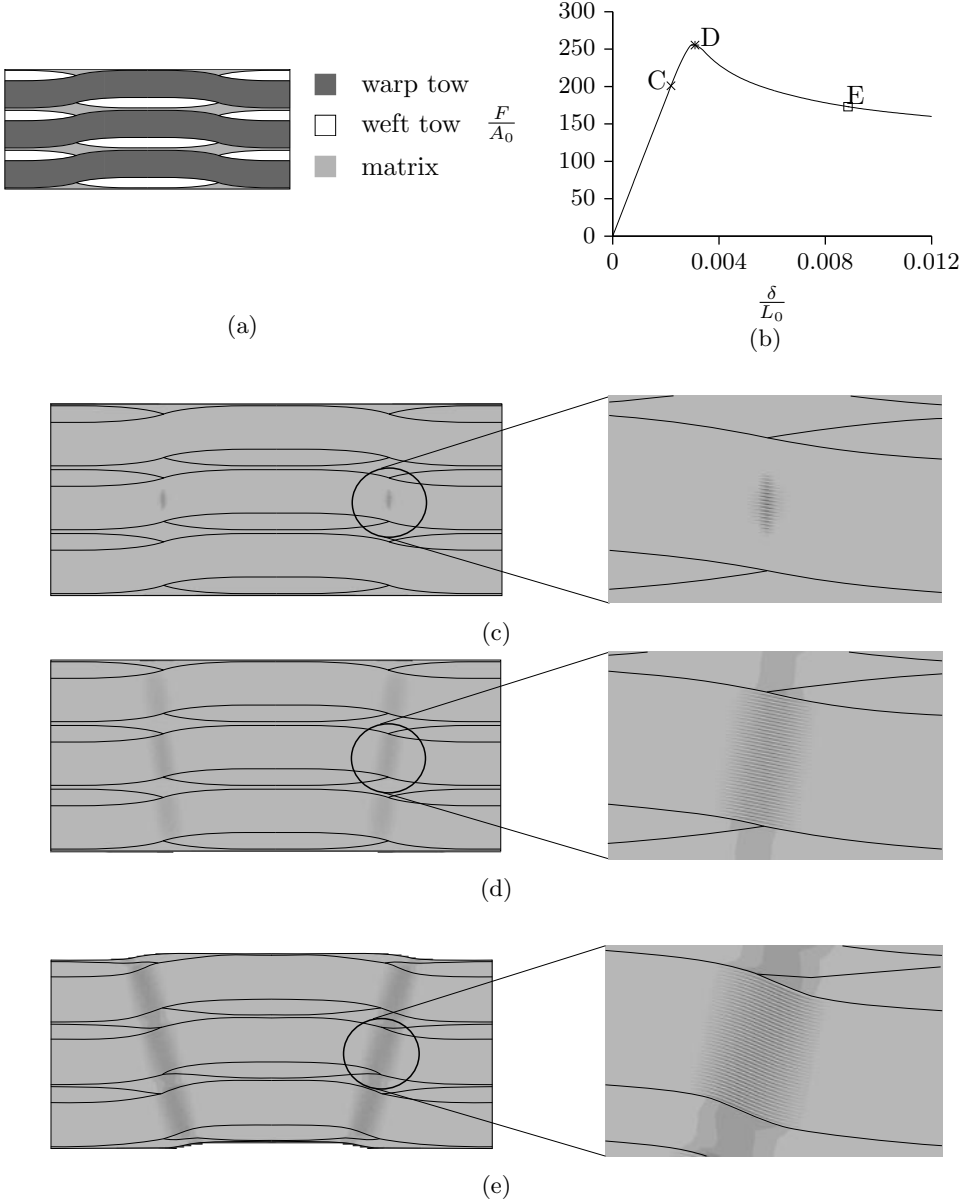


Figure 2.4: An overview of the compressive failure mechanism. 2.4a shows a legend with the positions of the warp tow, weft tow and matrix. 2.4b shows the stress-strain curve generated using a model with two cells and three layers. The points C,D and E illustrate the points in the stress-strain curve where snapshots are taken. The snapshots of the contours of plastic strain show the areas where at least 1% plastic strain has occurred in dark grey. A snapshot of the plastic strain has been made at the first occurrence of plastic strain in 2.4c, at the peak load in 2.4d and post-peak in 2.4e.

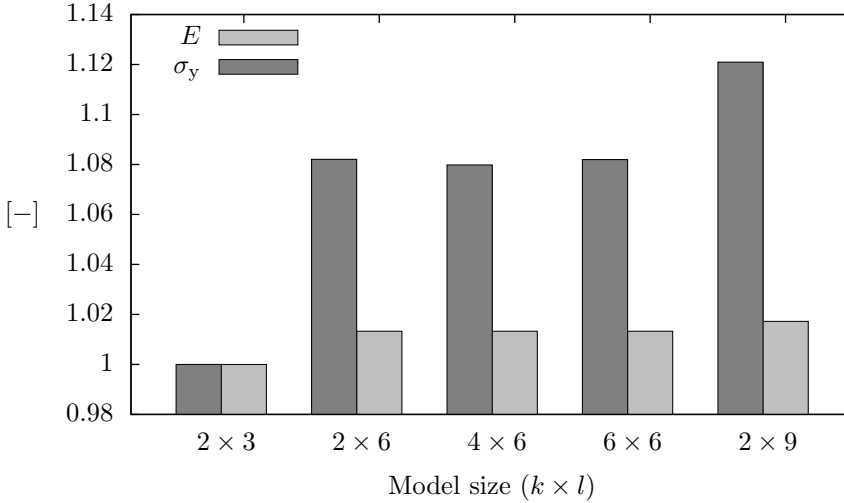


Figure 2.5: Dependency of the stress-strain response on the size of the model. A $k \times l$ model implies that a model has been simulated with k cells in the warp direction and l layers in the stacking direction. The results have been normalized with the results of a 2×3 model.

2.3.2 Influence of phase shifts

To investigate the effect of phase shifts between layers in the stacking direction, the undulations are shifted in the warp direction. All results are normalized with the results of an in-phase stacked model.

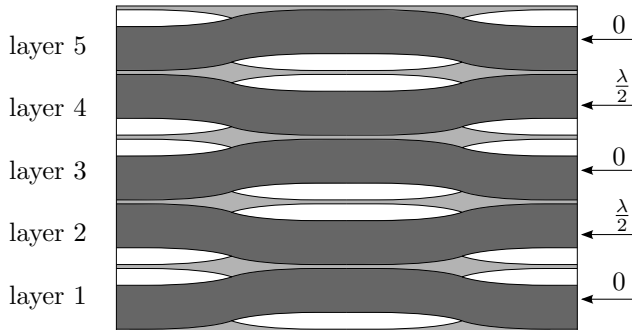


Figure 2.6: Overview of a 2x5 model where the second and the fourth layer are shifted with one wavelength λ .

Two sets of simulations are performed: a set of simulations with regular variations of the shifts of layers and a set of simulations with a random variation in the shifts of all of the layers. Within the first set of simulations, the second and the fourth layer in the model are shifted with a shift factor α of the wavelength λ . An example can be seen in Figure 2.6, where a model with shift factor $\alpha = \frac{1}{2}$ is presented. The apparent stiffness E and the compressive strength σ_c of this first set of simulations can be seen

in Figure 2.7.

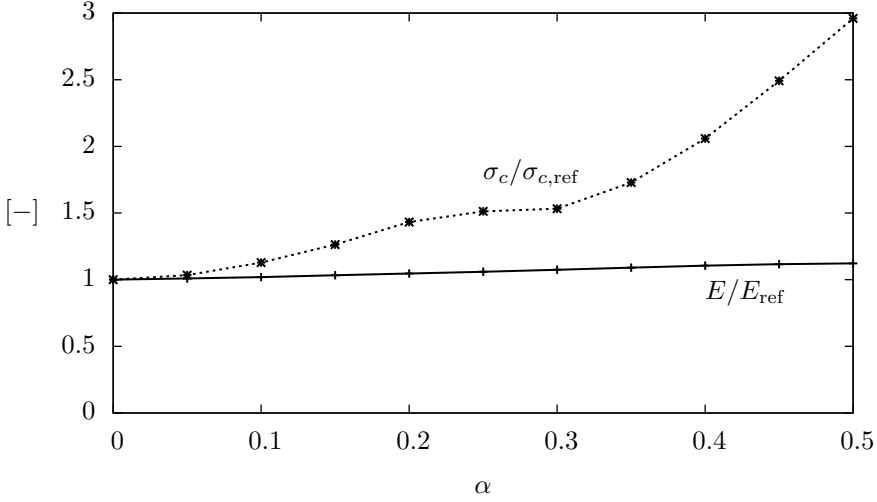


Figure 2.7: The normalised elastic modulus E/E_{ref} and the compressive strength $\sigma_c/\sigma_{c,\text{ref}}$ of the simulated laminate as a function of the shift factor α . The reference values $\sigma_{c,\text{ref}}$ and E_{ref} are taken at $\alpha = 0$.

In the second set of simulations, the layers are shifted in a random order. The stacking sequence can be identified by listing the shifts of each layer, starting from the bottom. In this way, the stacking sequence in Figure 2.6 can be identified by: $[0 \frac{\lambda}{2} 0 \frac{\lambda}{2} 0]$. Figure 2.8 shows the apparent stiffness E and the compressive strength σ_c of several randomly chosen laminates. Both sets of simulations indicate that there is a strong influence of the phase shifts on the compressive strength of the laminate. Stacking the layers of the laminate in phase provides a lower bound for the strength while stacking the layers out of phase provides an upper bound for the strength. The kink band patterns of three simulations will be discussed in more detail in Figure 2.9 to examine this spread in the strength of the laminates. The stacking sequences of these three simulations are identified in a similar way as with the random stacked simulations. The three stacking sequences are: an in-phase stacked $[0 0 0 0 0]$ laminate; an out-of-phase $[0 \frac{\lambda}{2} 0 \frac{\lambda}{2} 0]$ laminate and a random stacked laminate with stacking sequence $[0 0 \frac{\lambda}{4} \frac{\lambda}{2} \frac{\lambda}{2}]$. Figure 2.9 shows the stress strain curves and contours of the plasticity. The contour plots are taken at the peak of the stress strain curves and the dark-grey areas in the contour plots indicate the regions where there is at least 1% equivalent plastic strain.

2.3.3 Weave properties

To investigate the influence of changes in the geometry of the laminate on the compressive strength σ_c and the stiffness E of the laminate, a parameter study is performed. Four parameters are varied: the laminate fiber-volume-fraction V_{ft} ; the fiber-volume-fraction in the tow V_{ftt} ; number of fibers stacked in the tow n and the undulation angle of the weft tow θ . The variation in the laminate-volume-fraction is caused by

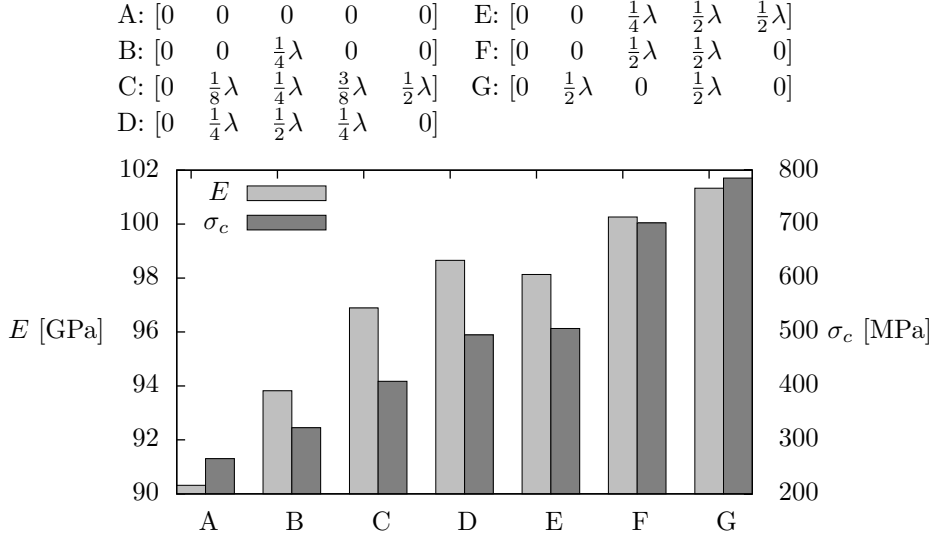


Figure 2.8: The elastic modulus E and the compressive strength σ_c of the simulated laminate using random stacking sequences.

a variation in the matrix pocket thickness t_p , all other parameters are kept constant. An indication of the knockdown factor in stiffness due to the waviness of the laminate is made by comparing the stiffness calculated using simulations E_{sim} with the Voigt and Reuss averages E_{Voigt} and E_{Reuss} :

$$E_{\text{Voigt}} = E_f V_f + E_m (1 - V_f), \quad (2.9)$$

$$\frac{1}{E_{\text{Reuss}}} = \frac{1}{E_f} V_f + \frac{1}{E_m} (1 - V_f). \quad (2.10)$$

Another comparison which can be made is the comparison between the simulated compressive strength and the kinking stress determined by (2.1). If a Reuss bound is assumed for the composite shear modulus:

$$\frac{1}{G} = \frac{2(1 + \nu_f)V_f}{E_f} + \frac{2(1 + \nu_m)(1 - V_f)}{E_m}, \quad (2.11)$$

the kinking stress σ_{kink} can be determined using (2.1). The effect of a variation in the laminate fiber-volume-fraction on the compressive strength and modulus can be seen in Figure 2.10.

To study the effect of the tow fiber-volume-fraction, the thickness of the matrix layer in between the fibers t_m is varied. With a fixed number of fibers and a fixed fiber thickness this would increase the total thickness of the model t_{lam} . The number of fibers in the tow n is therefore adjusted in such a way that the total thickness of the model t_{lam} is constant. The effect of changing the tow fiber-volume-fraction V_{ft} on the compressive stiffness and strength can be seen in Figure 2.11.

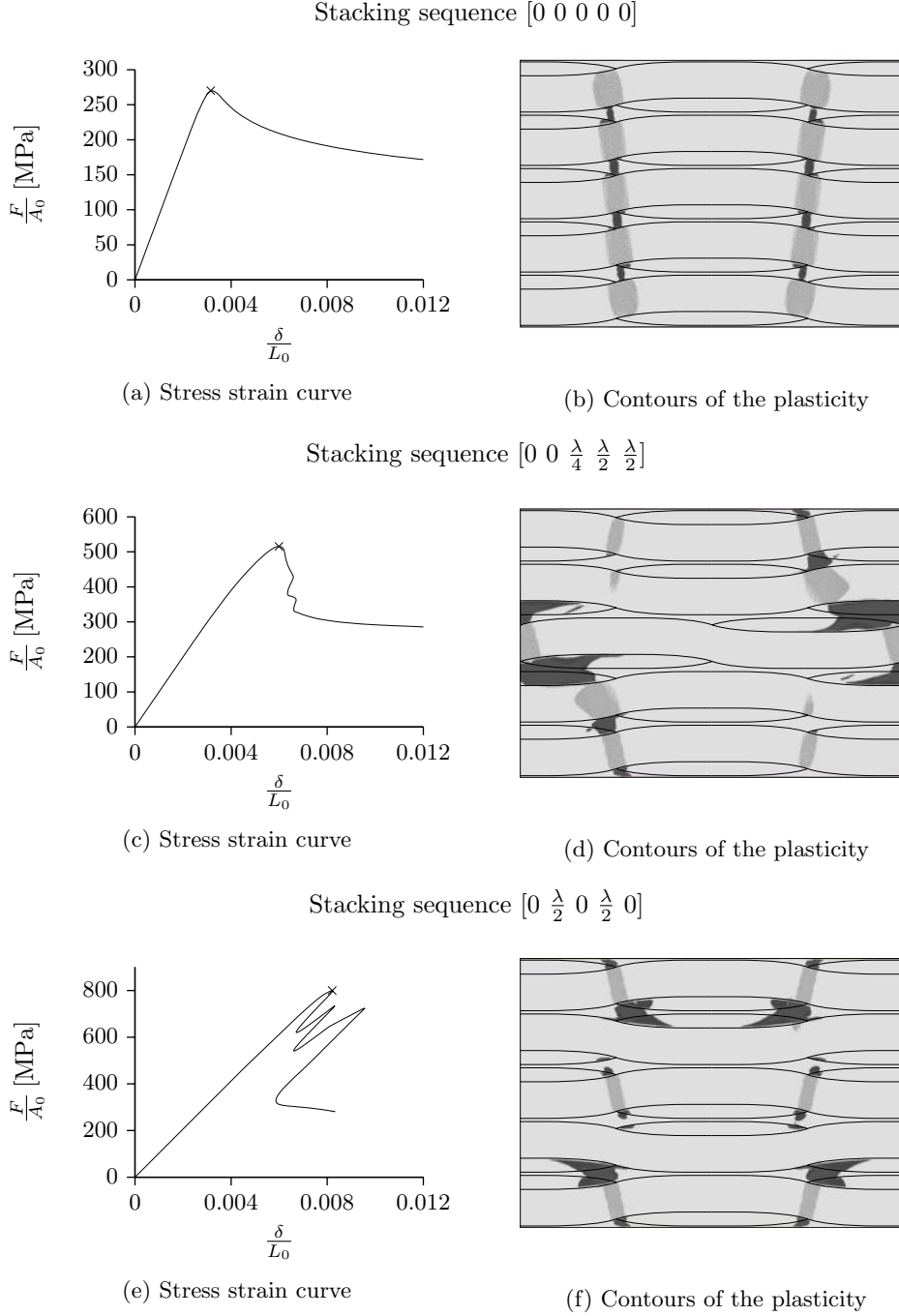


Figure 2.9: Stress strain curves and snapshots of the regions of plasticity for an in phase stacking (a and b), an out of phase stacking (c and d) and a random stacking (e and f). The snapshots of the plasticity are taken at the peak stress, indicated by the cross in the force displacement graphs. The dark-grey areas in the contour plots indicate the regions where there is at least 1% equivalent plastic strain.

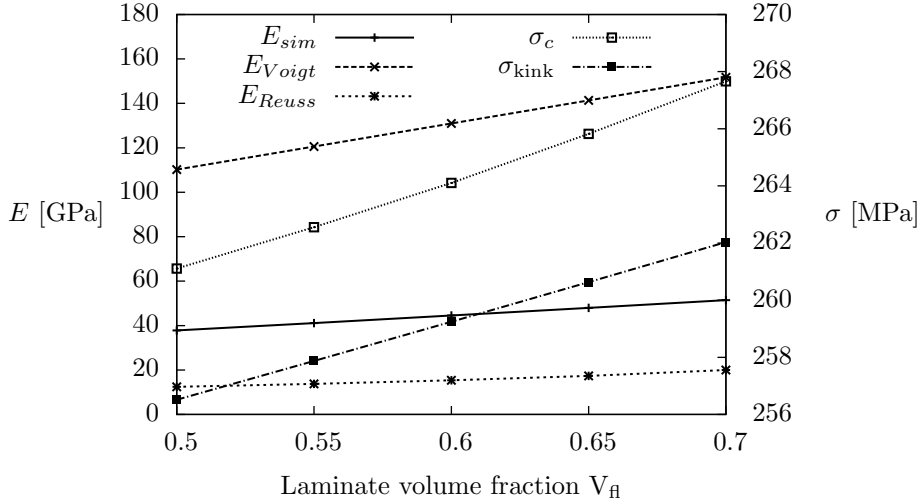


Figure 2.10: The elastic modulus E and the compressive strength σ_c of the simulated laminate as a function of the laminate fiber-volume-fraction V_f .

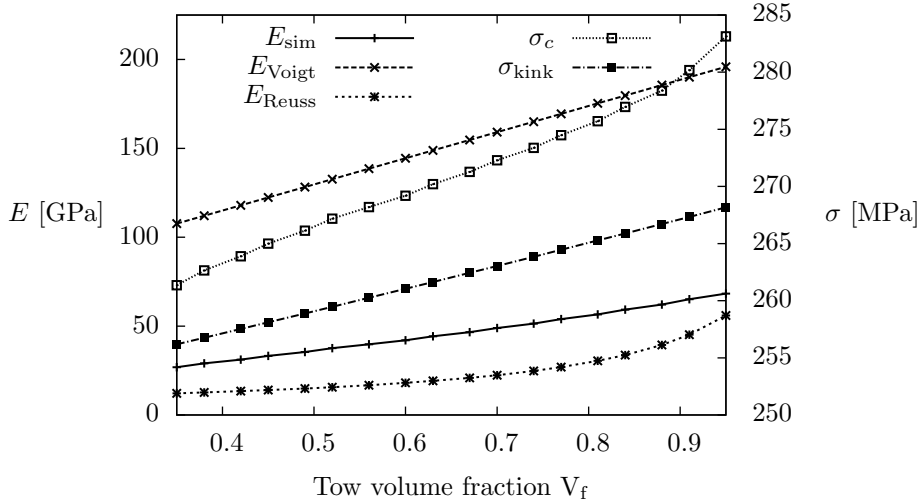


Figure 2.11: The elastic modulus E and the compressive strength σ_c of the simulated laminate as a function of tow fiber-volume-fraction V_f .

The effect of the length scale introduced by using a thicker or thinner tow in the weave can be investigated by varying the number of fibers n . A side effect of increasing the tow thickness is that the laminate fiber volume fraction increases as well. All other parameters are kept constant. The effect of the number of fibers in the tow n on the stiffness and strength of a laminate can be seen in Figure 2.12. The change in laminate volume fraction V_f has been plotted as well.

The last parameter that is investigated is the looseness of the weave. If the weave

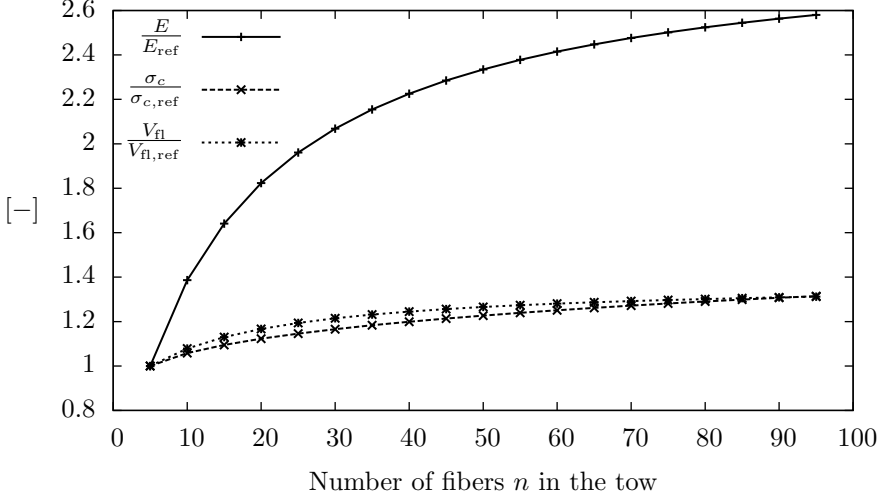


Figure 2.12: The elastic modulus E and the compressive strength σ_c of the simulated laminate as a function of the number of fibers in the tow n . The change in laminate volume fraction V_{fl} is shown as well. Note that the reference values have been taken at the lowest number of fibers in the tow.

is tightly woven and the weft tows are placed close to one another, the matrix pockets will be smaller and therefore the fiber-volume fraction of the laminate will increase while the undulation angle of the warp tow has to increase. To investigate this trade off, the unit cell is slightly modified to the unit cell depicted in Figure 2.13. Whilst in the geometry depicted in Figure 2.2 the weft tow geometry would change with the undulation angle, the weft tows in Figure 2.13 are converted to rectangles with constant area to keep the same fiber volume fraction in the weft tow. The distance between the weft tows is now d . The ratio d/λ now indicates the looseness of the weave and can be varied by changing d . Varying the ratio d/λ will show the trade of between

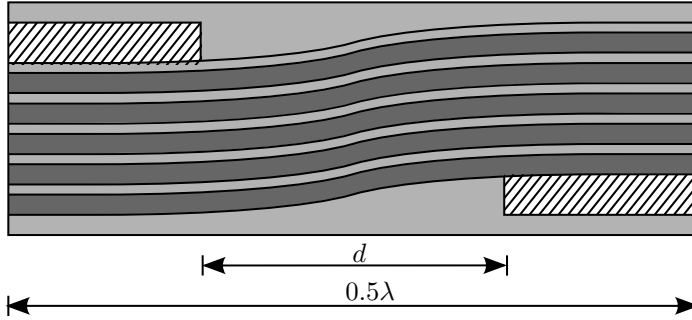


Figure 2.13: Overview of the modified unit cell. The weft tows are made rectangular and the distance between the weft cells is defined by d . Note that only 5 individual warp fibers are drawn for illustrative purpose.

a smaller undulation angle and increasing the size of matrix pockets between the tows

and thus decreasing the laminate volume fraction V_{fl} . The compressive stiffness and strength of laminates as a function of d/λ can be seen in Figure 2.14. Again, the change in laminate volume fraction V_{fl} has been plotted as well.

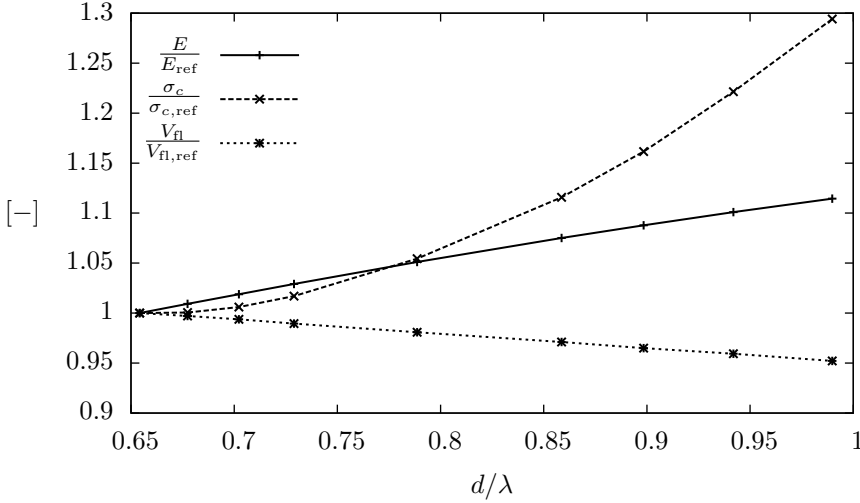


Figure 2.14: The elastic modulus E and the compressive strength σ_c of the simulated laminate as a function of the looseness of the weave d/λ . The change in laminate volume fraction V_{fl} is shown as well. The reference values are taken at the lowest value for d/λ .

2.4 Discussion

The goal of this research was to study the formation of kink-bands in woven carbon-fiber reinforced plastics. A micro-scale model was introduced which is able to characterize parameters of influence on the formation of these kink-bands. The benefit of the presented model is that there is no need for constitutive relations which describe the process of kink-band formation. Instead, the formation of the kink-bands is a direct result of the used geometry and basic constitutive properties of the matrix and the individual fibers. Although the geometry and the constitutive relations are a simplification of the reality, the model presented in this Chapter is able to describe the generation of kink bands in a plain woven composite. Figure 2.5 indicates that the number of cells used to describe the laminate does not have a significant influence on the response under compression if more than three layers are stacked on top of each other.

Due to the absence of periodic boundary conditions, kink-bands can form under an arbitrary angle and the model is not limited to an in-phase or out-of-phase stacking sequence. The presented model allows the investigation of the compressive response of a number of regular and irregular stacking sequences, as well as an investigation of the effect of several characteristic parameters of a weave.

2.4.1 Stacking sequences

De Carvalho et al. [27] suggested that the role of the support of the surrounding layers in the laminate is not negligible. The presented model is able to quantify the role of the support and the influence of the the phase difference is significant. If all cells are stacked in phase, such as displayed in Figure 2.9b, the part of the fiber-tows where the undulation angle θ is the largest are located directly above each other. If all stacked tows have the same local undulation angle, all of the tows will deform in a similar direction forming one big kink, making the stress-strain response relatively weak. If the undulation angles are opposing as displayed in Figure 2.9f, the deformation of the stacked tows is canceled out. The stress-strain response of this stacking sequence is relatively strong.

The results presented in Figures 2.7 and 2.8 are in agreement with the results of De Carvalho et al. [27] in the sense that the in-phase and out-of-phase stacking provide an upper and lower bound for the strength respectively. Although not as substantial as presented in this chapter, the physically based model of De Carvalho et al. [6] also predicts a significant difference in the compressive strength of plain weave composites.

It should be noted that the current constitutive model only includes plasticity of the matrix. Kink-bands formation is the only failure mechanism described by the model. Local concentrations of plasticity such as in Figure 2.9d indicate that other failure mechanisms such as delamination might occur. Another remark which can be made is that the strength for the out-of-phase stacking is in some cases overestimated due to the idealized geometry. In a real composite, such a perfect in-phase or out-of-phase configuration is likely to never exist, as is indicated by the small spread in experimentally determined compressive strengths presented by De Carvalho et al. [6].

2.4.2 Weave properties

Four characteristic parameters are varied: the laminate volume fraction V_{fl} , the tow volume fraction V_{ft} ; the number of fibers n which determines the thickness of the tow and the undulation angle θ through the looseness ratio d/L .

Figures 2.10 and 2.11 show that the change in the stiffness and compressive strength is approximately linear for both of the volume fractions over the ranges simulated. The comparison of the modulus with the Voigt and Reuss bound indicates that the undulation of the fibers causes a significant decrease in the stiffness of the laminate. A slight increase in compressive strength with increasing volume fractions can be seen as well in Figures 2.10 and 2.11. This increase in strength agrees well with the increase in strength predicted by the plastic-microbuckling solution proposed by Budiansky et. al. in (2.1). An increase in fiber volume fraction causes an increase in the composite shear modulus and therefore the kinking strength increases.

When investigating the effect of using a thicker tow, a similar trend can be seen. The laminate stiffness increases significantly with an increasing number of fibers n in the tow. The increasing number of fibers in the tow causes an increase in the fiber volume fraction and therefore the compressive strength increases slightly.

Another parameter which is also present in the elasto plastic-microbuckling solution is the looseness ratio d/λ . Increasing d/λ decreases the undulation angle θ which can be seen as the imperfection angle $\bar{\phi}$ in the elasto plastic-microbuckling solution 2.1. Although the laminate fiber volume fraction is decreased by increasing the size of the matrix pockets (distance d), the strength of the laminate increases as the undulation

angle decreases.

An important note that has to be made is that these four parameter studies were done using an in-phase stacked geometry. Therefore only a single kink, comparable to a kink in a unidirectional composite, is formed as can be seen in Figure 2.9b. The variation of the four weave properties only indicate the change in the lower bound for the strength. As the simulations with various stacking sequences indicated, the phase shifts have a considerable effect on the compressive strength. As the elasto plastic-microbuckling solution was intended for unidirectional composites, it does not take into account the kinematic effects of the tows and therefore cannot take into account the strengthening effect of phase shifts in textile composites.

2.5 Conclusion

This Chapter presented a micro-scale model which is able to describe the formation of kink-bands in woven composites. Several stacking sequences were simulated and a parameter study was performed to investigate the effect of several characteristics of a woven laminate.

The several stacking sequences simulated confirmed that an in-phase stacking is the weakest configuration and that an out-of-phase stacking is the strongest configuration. Moreover, the effect of differences in stacking sequences was characterized by simulating a number of regular and irregular varied stacking sequences.

The laminate stiffness is mainly determined by the fiber volume fraction and the undulation angle of the warp tow. Finally, the strength of the laminate is determined by the undulation angle of the warp tow and the phase difference between the layers rather than the fiber volume fraction.

The micro-scale model as developed in this Chapter will be used as a starting point of the derivation of a meso-scale model that can be used to study CFRP materials on a coupon level in 3 dimensions. This model and its implications will be discussed in the next Chapter.

Chapter 3

Notch sensitivity in woven carbon-fiber reinforced plastics

In this chapter, the micro-scale model of the previous chapter is used to help construct a three dimensional meso-scale model that is used to study the formation of kink-bands around holes in coupons. The model is used to study the formation of kink-bands near holes and to investigate the influence of several length scales on the notch sensitivity of plain weave composites under compressive loadings.

3.1 Introduction

When designing components and structures, the notch sensitivity of the used material is an important design parameter. For fiber reinforced plastics, the notch sensitivity is complicated by the existence of multiple length scales such as fiber diameters, ply thicknesses, and sample dimensions.

For uni-directional (UD) laminates, the mechanical response of notched samples is studied widely. A summary of the early work was presented by Awerbuch and Madhukar [38]. A large part of the literature is focused on predicting failure and its accompanying failure mechanisms under tensile loading. Analytical calculations using linear elastic fracture mechanics were performed by Sutcliffe and Fleck [39]. Differences between ply-level and sub-laminate level scaling were investigated experimentally by Wisnom et al. [40], numerically by Xu et al. [41] and Hallet et al. elegantly combined numerical and experimental techniques in [42]. Numerically, van der Meer et al. [43] used an approach based on the phantom node method and captured the influence of ply thickness on the delamination pattern of a notched cross-ply composite. Camanho et al. [44] used a continuum damage mechanics approach to characterize scaling effects under tensile loading in uni-directional composites.

Other loading types are less abundant in the literature. Chang et al. [45] studied the difference between molded in and drilled holes in woven composites using a pin-loaded experimental setup. They concluded that the failure strengths of woven composites with molded in holes are mostly higher than those of composites with drilled

holes. Within an experimental study, Tan et al. [46] used an modified Arcan rig to determine a failure envelope of a uni-directional laminate under multi-axial loading. In a following numerical study, Tan et al. [47] used a finite element model to reproduce this failure envelope. Sutcliffe and Fleck [39] did an experimental and theoretical investigation into composite panels with edge notches, center notches and centered holes under compressive loadings. They modeled the kink using cohesive zones and predicted the critical length of a kink. Soutis et al. [48] developed a cohesive zone approach where fiber-kinking, delamination and plastic deformation are bundled in a single crack and used their model to predict the effects of hole-size and lay-up on the compressive strength of a laminate. More recently, Su et al. [49] used a progressive damage model to investigate ply-level scaling and sub-laminate level scaling.

In contrast to the amount of literature reporting on uni-directional composites, studies focused on notched woven composites are limited. Reifsnider and Mirzadeh [23] performed an experimental study on notched and un-notched eight-harness satin weaves and reported that kinks not necessarily occur at the location of the maximum stress peak, but may also form at areas with the highest crimp factor. Fleck et al. [50] applied the cohesive zone model of Soutis [48] to uni-directional, two-dimensional woven and 3D woven materials to study their notch sensitivity and found that the strength of woven composites is relatively notch-insensitive when subjected to compressive loading.

In general, the compressive failure of thick composites, composites that fail due to material failure rather than structural buckling, is governed by the formation of kink bands. Kink-bands have been widely studied in the literature. Analytically, Rosen [14] proposed an elastic buckling solution to describe kinking. Argon [15] later suggested that kinking was due to plastic micro-buckling and Budiansky [17] provided an approximation of the kinking stress based on an elasto-perfectly plastic material.

Numerical study on kink-band formation was performed first by Kyriakides et al. [18] who modeled a uni-directional composite on the micro-scale under the assumption of linear elastic fibers and an elasto-perfectly-plastic matrix. On the same scale, Pimenta et al. [19] modeled the matrix using several constitutive models and claimed that an elasto-perfectly-plastic matrix was sufficient to model kink-bands. The micro-mechanical approach used by Kyriakides, where every fiber is modeled individually, was applied to woven composites in Chapter 2, where a two-dimensional plain strain model a plain weave composite laminate is constructed. Modeling on the micro-scale ensures that the kink width is correctly captured due to the presence of bending effects introduced by individual fibers.

When making finite element models of woven composites, it is a challenge to produce a representative geometry of a weave. As the weaving patterns of woven laminates are periodic, the micro structure can be represented by unit cells. An overview of modeling strategies can be found in the work of Lomov et al. [51] and an example of the construction of such unit cells was published by Verpoest and Lomov [52]. There are several papers that demonstrate the effective use of unit cells. Ivanov et al. [53], used a single unit cell in combination with novel boundary conditions to study the interaction of plies, local stresses and displacements in plain woven composites. De Carvalho et al. [6] used a reduced unit cell to study a twill woven composite under biaxial loading and Tang et al. [54] studied the progressive failure of several weave architectures.

Fleck et al. suggested that the strength of plain weave composites is relatively notch insensitive when compared to an uni-directional composite. However, as the

cohesive zone model used to make this claim does not take into account the meso-scale structure and lumped several failure mechanisms into one single crack, there was no insight given as to why the strength of plain weave composites is relatively notch insensitive. Therefore, the goal of this chapter is to investigate the interaction between several meso-scopic length scales such as the tow size, hole size and sample width in notched plain weave composites under compressive loading.

First, a 3D meso-scopic modeling strategy is presented in Section 3.2. This strategy is then applied to simulate the notch sensitivity of plain weave composites. The effect of several length scales such as the diameter of a center hole, the width of a tow and the width of a sample on the notch sensitivity is investigated in Section 3.3 along with the compressive failure mechanism.

3.2 Methods

Within the following section, a 3D finite element model of a balanced plain weave is presented. The constitutive modeling of the tows and the matrix is discussed first, followed by the geometry and boundary conditions of the model. All of the models presented within this study were made using the finite element package ABAQUS[®] [55].

3.2.1 Constitutive modelling

The constitutive properties of the fibers and the matrix in the textile composite are similar to those of the AS4 fibers and PEEK matrix used in the paper of Kyriakides et al [18]. The fibers are assumed to be isotropic elastic and have a Young's modulus of $E_f = 214$ GPa and a Poisson's ratio of $\nu_f = 0.263$. The matrix is modeled as an elasto-plastic material with Young's modulus $E_m = 6140$ MPa, Poisson's ratio of $\nu_m = 0.356$ and an initial yield stress $\sigma_m^{y_0} = 82.1$ MPa. The plastic hardening is described by:

$$\sigma_m^y = \sigma_m^{y_0} + H\epsilon_p, \quad (3.1)$$

where $H = 10$ MPa is the hardening modulus and ϵ_p is the plastic strain. In order to include the effect of potentially delaminating layers in the weave, the matrix is set to fail after 15% plastic strain. It is assumed that the point of initiation of damage is independent of the stress triaxiality, therefore the Johnson-Cook criterion implemented in ABAQUS[®] is used with only the first term. The fracture toughness of the matrix is assumed to be $G_c = 1.69$ mJ/mm², as was measured by Wang et al. [56].

To reduce the computational cost of the meso-scale model, a homogenized constitutive model is used for the tows. The elastic properties of the fibers and the matrix are used to calculate the properties of a transverse isotropic medium using Voigt and Reuss averages:

$$E_1 = E_f V_f + E_m (1 - V_f) \quad (3.2)$$

$$\frac{1}{E_2} = \frac{V_f}{E_f} + \frac{1-V_f}{E_m} \quad (3.3)$$

$$\frac{1}{G_{12}} = \frac{2(1+\nu_f)V_f}{E_f} + \frac{2(1+\nu_m)(1-V_f)}{E_m} \quad (3.4)$$

where V_f is the fiber volume fraction in the tow, E_1 is the stiffness of the tow in the fiber direction, E_2 is the transverse stiffness of the tow and G_{12}^T is the shear modulus in

Table 3.1: Tow constitutive parameters

E_1	$E_2 = E_3$	G_{12}	$\nu_{ft}^T = \nu_{ft}^T = \nu_{ft}^T$	σ_y	H
145406 MPa	17582 MPa	6508 MPa	0.356	82.1 MPa	10.0 MPa

the 12 plane. It is assumed that $E_3 = E_2$ and that the Poisson's ratios of the transverse isotropic tow are equal to the Poisson's ratio of the matrix: $\nu_{ft}^T = \nu_{tf}^T = \nu_t^T = \nu_m$. An overview of the constitutive parameters used for the tows can be seen in Table 3.1. The local element orientations are rotated to indicate the direction of the fibers as illustrated in Figure 3.1

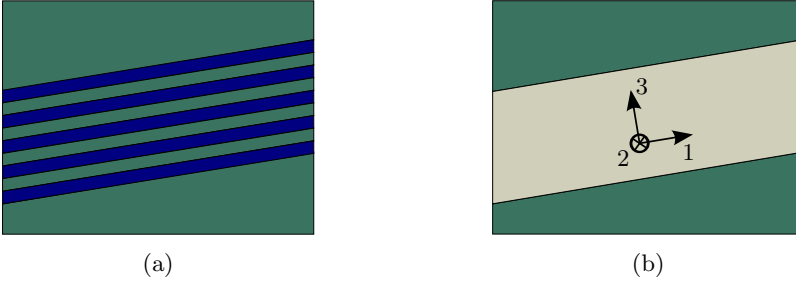


Figure 3.1: A tow where 4 individual fibers (blue) are surrounded by matrix (green) is shown in (a). A homogenized tow (brown) is shown in (b). The arrows indicate the directions of the local element coordinates for the homogenized material.

As the homogenized tows are transversely isotropic, Hill's quadratic failure criterium [57] as implemented in ABAQUS[®] is used to model the behavior of the tow in the nonlinear regime. A similar approach had been used before by Lemansky et al. [58], who modeled individual uni-directional plies as orthotropic-elastic materials in combination with Hill's quadratic failure criterium. Within Hill plasticity, an anisotropic yield potential is defined as:

$$f(\boldsymbol{\sigma}) = (F(\sigma_{22} - \sigma_{33})^2 + G(\sigma_{33} - \sigma_{11})^2 + H(\sigma_{11} - \sigma_{22})^2 + 2L\sigma_{23}^2 + 2M\sigma_{31}^2 + 2N\sigma_{12}^2)^{\frac{1}{2}}. \quad (3.5)$$

If the yield stress values $\bar{\sigma}_{ij}$ are the yield stress values of the material under a loading state where σ_{ij} is the only non-zero stress, the ratios F, G, H, L, M and N can be determined using:

$$F = \frac{\sigma^0}{2} \left(\frac{1}{\bar{\sigma}_2^2} + \frac{1}{\bar{\sigma}_2^2} - \frac{1}{\bar{\sigma}_1^2} \right) \quad (3.6)$$

$$G = \frac{\sigma^0}{2} \left(\frac{1}{\bar{\sigma}_2^2} + \frac{1}{\bar{\sigma}_1^2} - \frac{1}{\bar{\sigma}_2^2} \right) \quad (3.7)$$

$$H = \frac{\sigma^0}{2} \left(\frac{1}{\bar{\sigma}_1^2} + \frac{1}{\bar{\sigma}_2^2} - \frac{1}{\bar{\sigma}_2^2} \right) \quad (3.8)$$

$$L = \frac{3}{2} \left(\frac{\tau^0}{\bar{\sigma}_{23}} \right)^2 \quad (3.9)$$

$$M = \frac{3}{2} \left(\frac{\tau^0}{\bar{\sigma}_{13}} \right)^2 \quad (3.10)$$

$$N = \frac{3}{2} \left(\frac{\tau^0}{\bar{\sigma}_{12}} \right)^2 \quad (3.11)$$

where σ^0 is a reference yield stress and $\tau_0 = \sigma^0/\sqrt{3}$ is the corresponding reference shear yield stress. The yield stress in the fiber direction is set to a high value such that the tow will not yield in that direction. For all other directions, the yield stress ratios are set to 1 and the tow yields at the same stress as the matrix. The shear strengths were all set to be equal to the shear strength of the matrix τ_y .

$$\bar{\sigma}_1 = \sigma_f V_f + \sigma_m (1 - V_f), \quad (3.12)$$

$$\bar{\sigma}_2 = \left(\frac{V_f}{\sigma_f} + \frac{1 - V_f}{\sigma_m} \right)^{-1}, \quad (3.13)$$

$$\bar{\sigma}_{12} = \bar{\sigma}_{13} = \bar{\sigma}_{23} = \sqrt{3} \tau_y. \quad (3.14)$$

The plastic strain evolves according to the flow rule:

$$d\epsilon^{pl} = d\lambda \frac{\partial f}{\partial \sigma} \quad (3.15)$$

2D plain weave models

A downside of homogenizing the tows, is that the individual fibers and therefore the bending stiffness of the fibers is lost. The loss of this bending stiffness results in mesh sensitivity of the homogenized tows. To account for this mesh sensitivity, two-dimensional plane strain models are made which are compared to micro-models, based on the models presented in Chapter 2. The mesh size of the homogenized models is then chosen such that the peak strength of the laminate and the kink width are similar to those of the micro model.

A cross-section along the middle of the unit cell parallel to the warp fibers has been chosen as the geometry of the 2D plane strain models. A total of 5 layers have been stacked on top of each other to prevent global buckling. The model with homogenized tows can be seen in Figure 3.2a, along with the boundary conditions of the model. A comparison between the stress strain curves of a plane-strain model with homogenized tows and plane-strain model where all of the fibers in the warp tow are modeled individually can be seen in Figure 3.2b. The resulting kink widths for a homogenized model and a micro model are compared in Figures 3.2c and 3.2d respectively.

3.2.2 3D plain weave model

The geometries of the three-dimensional simulations presented in this study are all built up out of the same unit cell, which can be seen in Figure 3.3. The plain weave unit cell is constructed using tows that are $t = 2.5$ mm wide and have a wavelength of 5 mm. At the thickest point, the tow is 0.2 mm thick. A minimum resin pocket thickness of 0.05 mm has been chosen such that the total height of the unit cell is

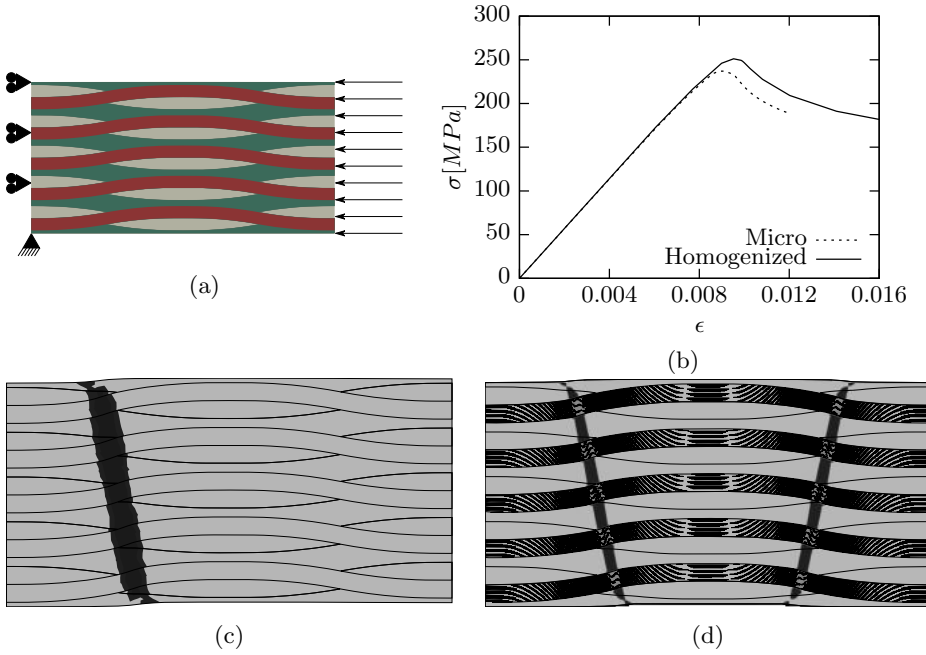


Figure 3.2: An overview of the plane strain homogenized model an the boundary conditions of the model can be seen in Figure (a). Figure (b) shows a comparison of the stress strain curves of a model with homogenized warp tows and a model where all of the fibers in the warp tows are modeled individually. Figure (c) and (d) show contour plots of the plastic strain for the homogenized model and the micro model respectively. The dark grey areas are the areas where there is a plastic strain of at least 10%.

0.5 mm. As the unit cell is modeled as one solid with different regions, no contact algorithms or cohesive zones are used to connect the constituents. The unit cells can

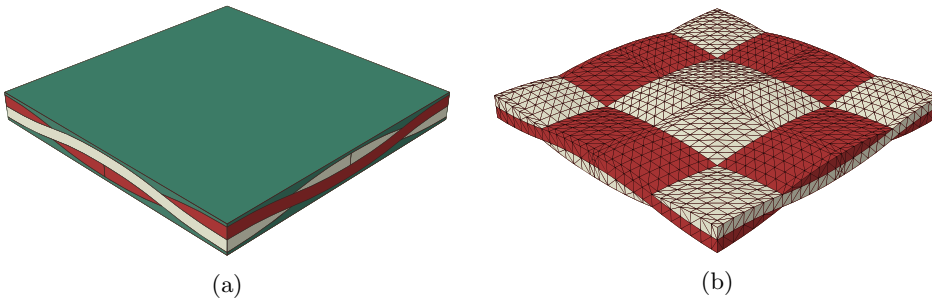


Figure 3.3: An overview of the used unit cell. The complete unit cell is shown in Figure (a) and the weaving pattern is shown in Figure (b). The matrix material is colored green, the warp tows are colored red and the weft tows are brown.

be stacked in phase to form plates. Holes are constructed by cutting a cylinder from the geometry. An example of such a plate with dimension $w \times L$ and hole diameter d can

be seen in Figure 3.4. The plates are loaded parallel to L by applying a displacement

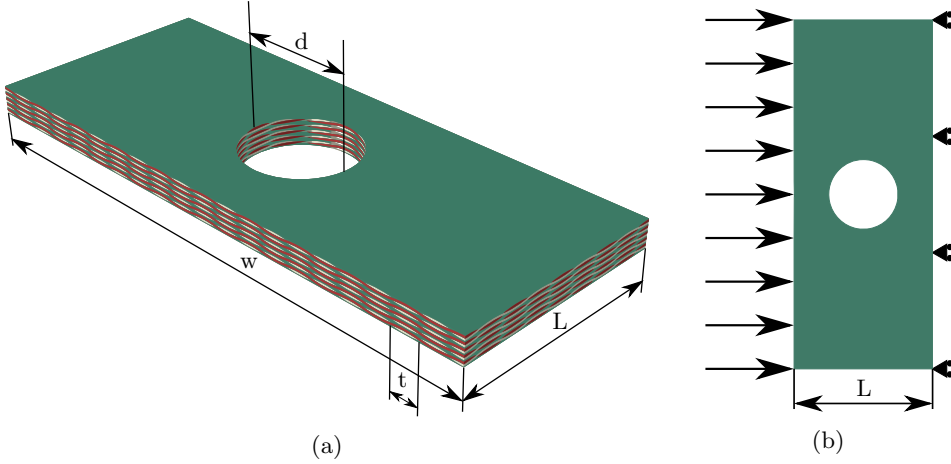


Figure 3.4: An overview of a plate with a hole. The dimensions of the plate are introduced in Figure (a) and the loading conditions can be seen in Figure (b).

on the left edge and fixing the displacements in the loading direction on the right edge as can be seen in 3.4b. The models are made using ABAQUS[®] explicit. The load is applied in 1 s. To reduce computational time, mass scaling is applied by specifying a stable time increment of $1 \cdot 10^{-5}$ s, keeping the kinetic energy below 5% of the internal energy. Large strain kinematics are assumed and a unit cell is meshed using an element size of 0.2 mm, resulting approximately 22.000 10-node modified quadratic tetrahedral C3D10M elements being placed in a unit cell.

3.3 Results

Within this section the 3D meso scale model is used to study the interaction of several length scales on the meso scale. Due to the detailed weave architecture, comparing plates of different sizes is not trivial. The fiber-volume fraction is e.g. different for a plate with a full tow at the edges and plate with a quarter of a tow at the edges. To make an equal comparison between different plate sizes and to cancel out edge effects, two simulations are used for each data point. The peak far field applied stress of a plate with a hole is compared to the peak far field applied stress of a similar sized plate without a hole σ_{un} . Two layups are investigated: a $[0\ 0\ 0\ 0\ 0]$ layup and a $[0\ 45\ 0\ 45\ 0]$ layup, where the angle is the angle between the warp tow and the loading direction. Note that as the weave is balanced, the warp and weft tow are similar.

3.3.1 Tow width

The interaction between the tow width t and the hole size d is investigated first. In this case, the net peak stress σ_{net} is analysed. The net peak stress is determined by summing the reaction forces on the loaded side and dividing them by the minimum cross-section of the plate, perpendicular to the loading direction near the hole. The tow size t is constant at 2.5 mm and the ratio d/t is varied such that the hole diameter

is in the range of $2.5 \text{ mm} \leq d \leq 15 \text{ mm}$. This process was repeated for several plate sizes w in the range of $12.5 \text{ mm} \leq w \leq 62.5 \text{ mm}$ by varying d/t at constant values of d/w . The results can be seen in Figure 3.5.

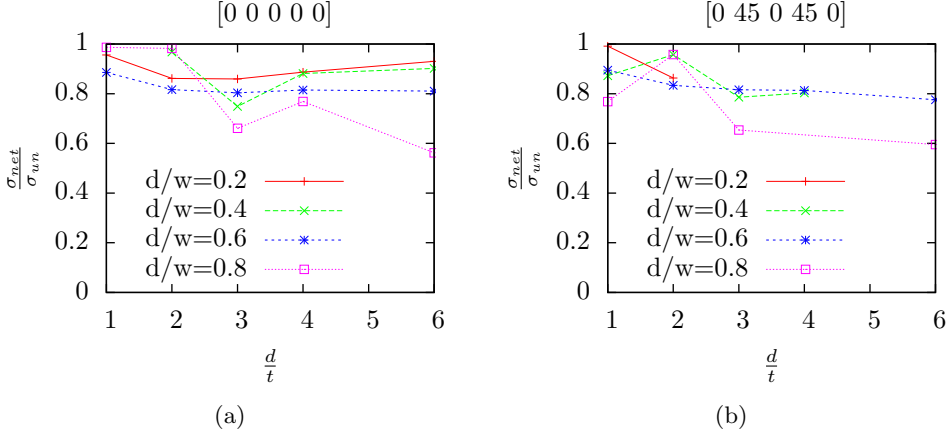


Figure 3.5: The ratios of net peak stresses σ_{net} and σ_{un} as a function of d/t for different values of d/w . Results for a $[0\ 0\ 0\ 0\ 0]$ layup are shown in Figure (a) and a $[0\ 45\ 0\ 45\ 0]$ layup is shown in Figure (b).

As can be seen in Figure 3.5, changing the ratio d/t does not affect the notch sensitivity.

3.3.2 Hole size

The effect of the hole size is examined by taking the notched peak stress σ_{no} , which is the remote stress of a plate with a hole, and again dividing it by the unnotched stress σ_{un} . Two separate situations are discussed. In the first situation, the edge of the hole is placed at the least undulating part of the tows. In the second situation, the edge of the hole is shifted a quarter wavelength such that the edge of the hole is placed at the part of the tow with the largest undulation. A graphical overview of these situations can be seen in Figure 3.6. The results of the simulations where the edge of the hole is located at the least undulating part of the tow can be seen in Figure 3.7, along with the predictions of the cohesive zone model of Soutis et al. [59], the experiments reported by Fleck et al. [50] and experiments performed at Wichita State University [60]. As can be seen from Figure 3.7 the simulations are in good agreement with the cohesive zone model of Soutis et al and shows slightly more notch-sensitive behavior than indicated by the experiments from Wichita State University [60].

Figure 3.8 shows the results of the simulations where the edge of the hole is located at the region where the tow undulates the most. With the edge of the hole located at the most undulating part of the tow, the simulations show a slightly more notch sensitive behavior than the cohesive zone model predictions of Soutis. The predictions are however more in line with the Wichita experiment.

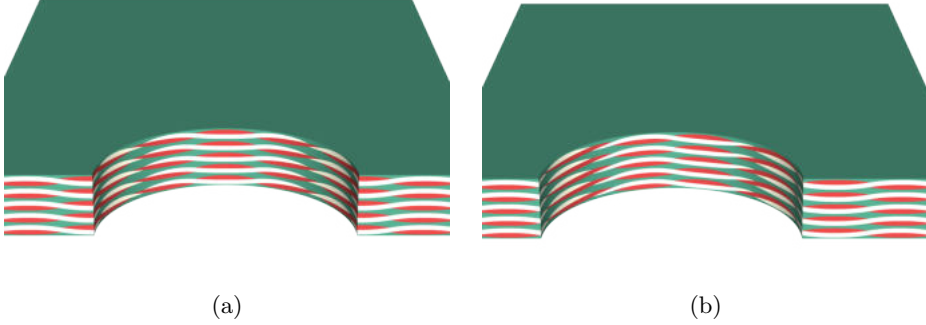


Figure 3.6: An overview of the two situations modeled. In Figure (a), the edge of the hole is placed at the least undulating part of the tow. Figure (b) shows the case where the edge of the hole is situated at the most undulating part of the tow.

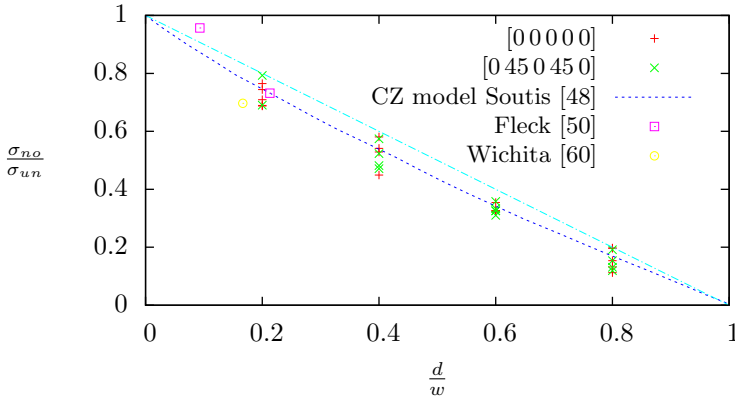


Figure 3.7: The ratios of notched remote peak stresses σ_{no} and un-notched remote peak stresses σ_{un} as a function of d/w .

3.3.3 Failure mechanism

To better understand why plain weave composites act relatively notch insensitive under compression, the failure mechanism is investigated. The $[0\ 0\ 0\ 0\ 0]$ plate with dimensions $d/w = 0.2$ and $d/t = 4$ is closer examined in Figure 3.9.

As can be seen in Figure 3.9b, areas undergoing plastic deformation are initiated near the hole. Instead of growing perpendicular to the loading direction, these areas grow parallel to the loading direction and therefore act as a splitting mechanism. Once the split has grown far enough and reaches a point where the undulation of the neighbouring tow is high, the neighbouring tow starts to kink and the plasticity grows perpendicular to the loading direction causing the plate to fail. To see whether this failure mechanism is affected by the layup, a $[0\ 45\ 0\ 45\ 0]$ plate is studied in Figure 3.10.

The $[0\ 45\ 0\ 45\ 0]$ plate shows the same failure mechanism as the $[0\ 0\ 0\ 0\ 0]$ plate. The plasticity starts at the hole and first grows parallel to the loading direction, acting as a splitting mechanism.

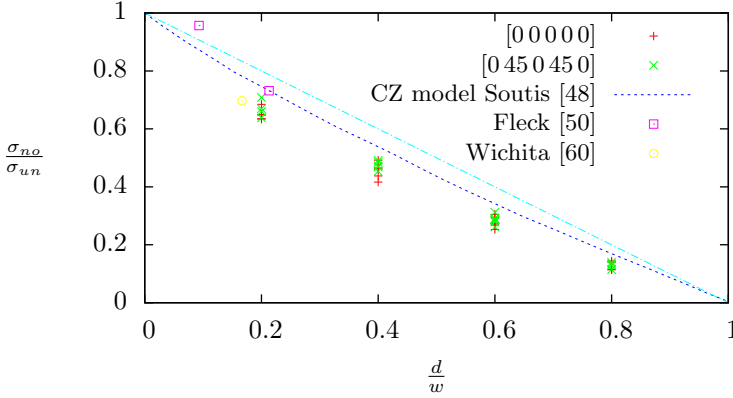


Figure 3.8: The ratios of notched remote peak stresses σ_{no} and un-notched remote peak stresses σ_{un} as a function of d/w .

3.4 Discussion

The goal of this research is to study the notch sensitivity of plain weave carbon fiber reinforced plastic plates under compressive loadings and the interaction of several length scales on the meso-scale. To do so, an idealized representation of a plain woven composite was made used to construct finite element models.

A comparison between the homogenized 2D plane-strain model and the 2D plane strain micro model showed that a kink-band can be simulated using an transversely isotropic tow in combination with Hill's quadratic failure criterion. Although this approach is mesh-sensitive, calibrating the mesh size using an equivalent micro-model yields a model that can simulate an equivalent kink-band with a similar stress-strain response. The reduction in the amount of degrees of freedom allows to produce 3D models of woven composites.

As can be seen from Figure 3.5, the strength of a woven composite is relatively insensitive to the size of the tows. There seems to be little difference between the [0 0 0 0 0] layup and the [0 45 0 45 0] layup. This would suggest that the length scale introduced by the width of the tow does not have to be included in a macroscopic constitutive model for woven plies. Figure 3.7 shows that the relation between the hole size and the width of the plate corresponds well to the cohesive zone model predictions of Fleck et al. [50] which are based on model of Soutis et al. [48].

The presentation of the failure mechanisms in the [0 0 0 0 0] and [0 45 0 45 0] layups in Figures 3.9 and 3.10 demonstrate that plastic zones start at the edge of the hole, and grows parallel to the loading direction. This plasticity acts as a splitting mechanism which reduces the stress concentration at the hole, similar to the mechanism commonly observed in uni-directional composites. In the paper of Fleck et al. [50], no such splits were observed. This lacking observation can be explained by the findings of Chan et al. [61]. In their paper they examined ceramic layered composites and assumed the interface between layers to be elastic-perfectly plastic with shear flow stress τ or slipping with constant friction stress τ . They determined that the length of a split increases as a function of the ratio σ/τ , where σ is the applied remote stress. Uni-directional composites usually have a higher compressive failure stress than 2D woven composites due to the lack of undulating tows. Assuming a similar matrix and

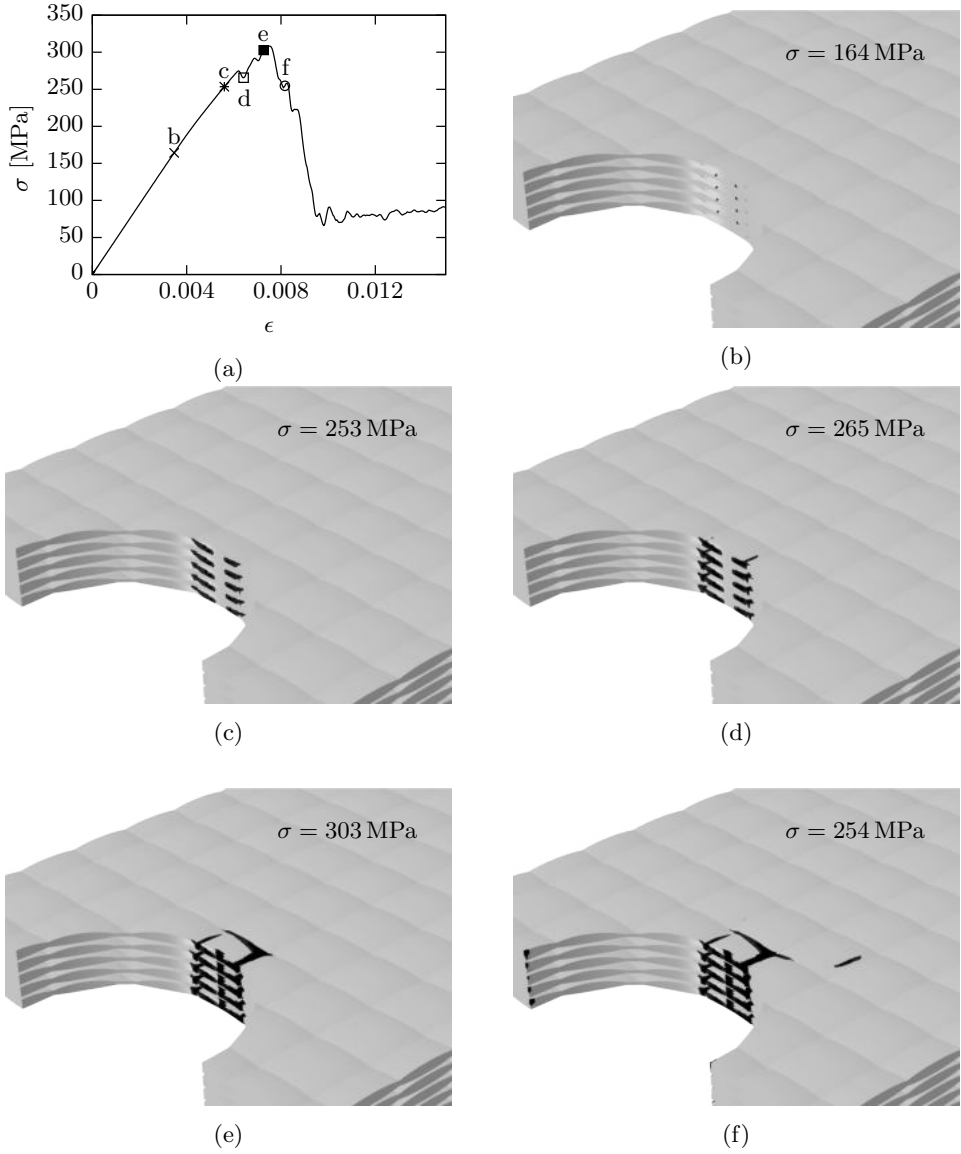


Figure 3.9: An overview of the failure mechanism of a $[0 \ 0 \ 0 \ 0 \ 0]$ plate. Figure (a) shows the compressive stress-strain curve as well as loads at which the snapshots were taken. The dark grey areas in the snapshots shown in Figures b till f indicate the areas where there is at least 5% plastic strain.

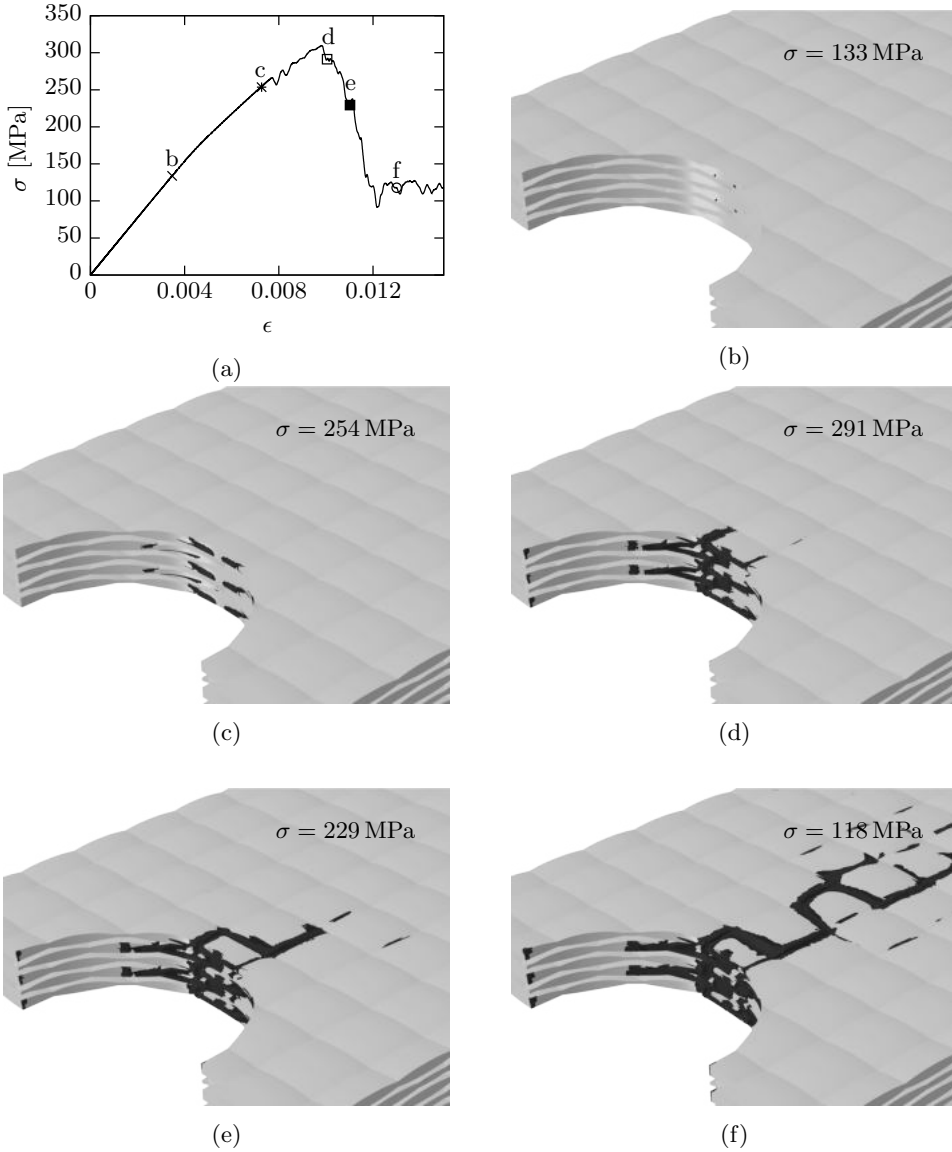


Figure 3.10: An overview of the failure mechanism of a [0 45 0 45 0] plate. Figure (a) shows the compressive stress-strain curve as well as loads at which the snapshots were taken. The dark grey areas in the snapshots shown in Figures b till f indicate the areas where there is at least 5% plastic strain.

therefore τ , more remote stress can be applied and therefore the splits are longer and easier to observe.

In the woven composite, the split needs to grow until the highest undulating section of the warp tow is reached as can be seen in Figure 3.9c. From this point onwards, a kink forms in the warp tow (Figure 3.9d). This mechanism is in accordance with the observation of Reifsnider et al. [23], who reported that kinks do not necessarily occur at the location of the maximum stress peak, but may also form at areas with the largest undulation angle.

The simulations predict slightly increased notch sensitive behavior if the edge of the hole is placed at a point where the undulation is the highest, which is shown in Figure 3.8. This configuration can be considered an upper-bound of the notch-sensitivity as the initiation of plasticity in this case coincides with the formation of a kink band. In a similar way the situation where the edge of the hole is placed where the undulation is the lowest, can be seen as an lower-bound for the notch-sensitivity as this case requires the longest split to form.

3.5 Conclusion

This chapter presented a meso-scale model of plain weave composites. The model was used to investigate the interaction between several meso-scopic length scales in notched plain weave composites under compressive loading.

It is found that notch-sensitivity of the strength corresponds well with the notch-sensitivity of the strength reported in the literature. A closer inspection of the failure mechanism shows that the notch sensitivity arises from the fact that the weakest section of the composite, the section with the highest undulation, is not always located at the edge of the hole where the stress concentration is the highest. When the section of the composite with the highest undulation does not coincide with the edge of the hole, a region of plasticity forms, causing a splitting mechanism.

In the next chapter, the performance of the Hill plasticity based homogenization for tows is evaluated under tensile loading.

Chapter 4

Application of the meso-scale model to tensile failure

It was shown in the previous chapter, that a transverse isotropic constitutive model for a tow in combination with Hill plasticity is a suitable way to model a thick plain woven composite under compressive loading on a meso-scopic scale. In this chapter, the performance of the model under a tensile loading state is examined. To do so, a two layered plain weave composite sample is modeled using the homogenized Hill plasticity approach presented in Chapter 3 and the micro modeling approach presented in Chapter 2.

4.1 Plain weave model

The geometry of the balanced plain weave textile modeled in this chapter is similar to the plain weave case that is modeled in the previous chapter. The model is reduced to two layers in the thickness direction as global buckling is not an issue under tensile loading. To be able to evaluate the homogenization strategy, the micro scale modeling approach, where individual fibers in the warp tows are modeled from Chapter 2 is used as a benchmark. The plain strain models are based on the balanced plain weave model presented in the previous chapter. The modeled plane is a cross section through the thickest point of the warp tows. The geometry and boundary conditions of these models can be seen in Figure 4.1.

The models are 5 mm long and the tows are 0.2 mm thick at the thickest point of the cross section. The maximum undulation angle is 10 degrees and the resin pockets in between the tows have a minimal thickness of 0.05 mm. The fiber volume fraction of the tows has been set to $V_f = 0.67$. The micro consists of 20 fibers across the thickness of the warp tow.

4.2 Tensile loading with Hill plasticity

In the first analysis, the micro model is loaded in tension and compared to a tensile simulation using the Hill plasticity constitutive model as used in Chapter 3. The resulting stress strain curves of these two simulations are compared in Figure 4.2. The

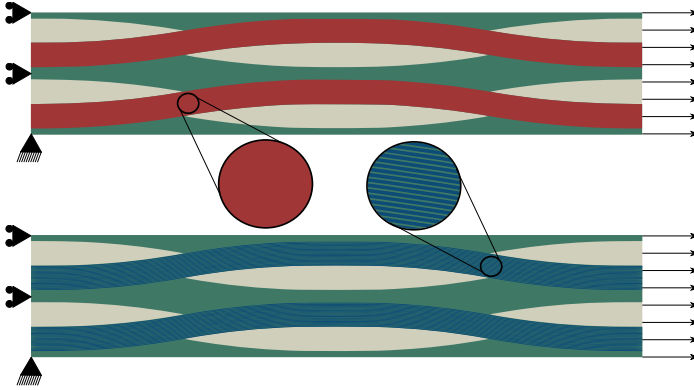


Figure 4.1: An overview of the boundary conditions of the homogenized (top) and micro model (bottom) of a 2 layered models of a plain weave composite under tensile loading.

engineering stress is calculated by dividing the reaction forces on the right hand boundary by the height of the model. The engineering strain is equal to the displacement of the right edge divided by the length of the model.

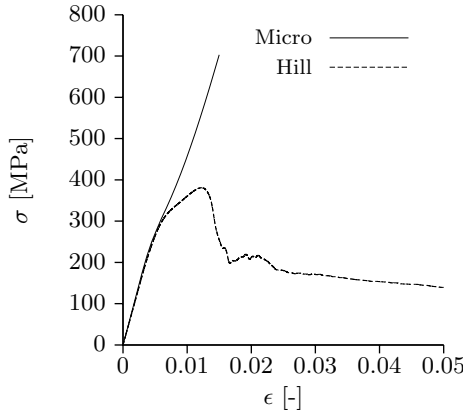


Figure 4.2: A comparison between the engineering stress-strain plots of simulations of plain weave composites under tensile loading modeled with Hill plasticity and a micro approach where individual fibers are modeled.

As can be seen from Figure 4.2, simulating the tensile response of a plain weave composite with homogenization based on Hill plasticity yields similar results to the micro model for small strains. For larger strains, i.e. for strains larger than 0.008 [-], the Hill plasticity model is incorrect as the Hill plasticity approach results in a highly non-linear stress-strain response opposed to the nearly linear stress-strain response predicted by the micro-model. This strong non-linear response originates from the large displacements that occur when the warp tows align with the tensile loading direction. The alignment of the tows causes a large local shear deformation in the

undulated areas.

In the micro scale model, the geometry of the fibers is modeled in detail and the fiber orientation is preserved during shear deformation of the tows, which is illustrated in Figure 4.3a. As the homogenized model based on Hill plasticity lacks a description of the micro structure and under shear loading, the local element orientation of the homogenized model rotates, as demonstrated in Figure 4.3b. The rotation of the local element orientation can be interpreted as a rotation of the local fiber direction in the tows, which in turn causes a reduction of stiffness as the homogenized properties are highly orthotropic. At approximately 0.05% strain, the matrix in between the fibers in the micro model and the warp tow in the homogenized model start to yield. From this point onwards, the local element orientations in the warp tow start to rotate and the stress-strain curves of the micro model and the homogenized model start to diverge. Figure 4.3c shows the deformed tows at approximately 1.5% strain along with the local element orientation indicated in blue. As can be seen in Figure 4.3c, the tow is stretched but the local element orientations rotate away from the loading direction, causing a reduction in stiffness.

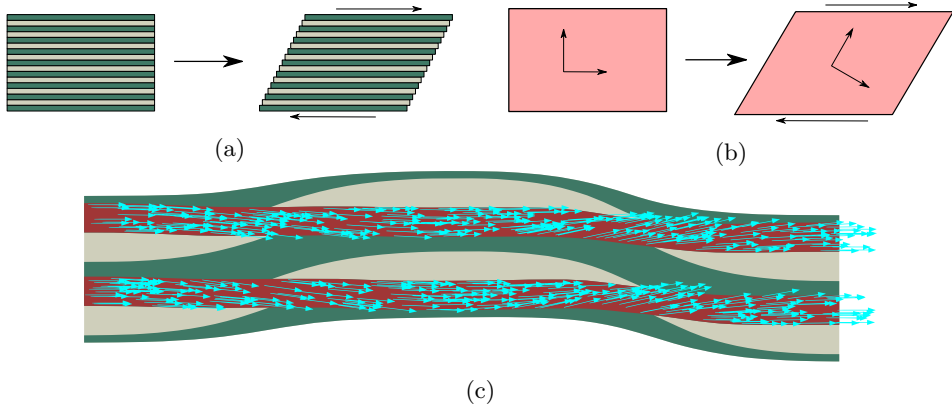


Figure 4.3: The difference in shear response between the micro model in Figure 4.3a and the homogenization based on Hill plasticity in Figure 4.3b. The local element orientations in the warp tows at 1.5% strain are shown in Figure 4.3c.

The stress-strain response of the micro model and the homogenized model start to deviate after approximately 0.05% strain. At this point, the matrix material between the fibers in the warp tow starts to yield in the micro model. In the homogenized model, the warp tow starts to plastically deform and the deformation eventually starts to localize at 1.5% strain. In tension, this localization does not occur in reality as the tow is uniformly stretched without rotating the fibers. However, the approach does work for the compressive loading scenarios as discussed in Chapter 3, as in this case, the deformation is meant to localize into a kink-band, where the fibers have a local rotation.

4.3 Crystal plasticity

A different approach that does have a description of the micro-structure and its orientation is Crystal Plasticity [62]. Originally intended for crystallographic materials, Crystal Plasticity uses slip planes and slip directions to describe the internal micro-structure of materials. In the context of fiber reinforced materials, the Crystal Plasticity framework can be used to describe UD materials or tows as they can be considered to be 2D cylindrical close packings.

In Crystal Plasticity, the deformation gradient F_{ij} is considered to be a multiplicative decomposition of the elastic deformation gradient F_{ij}^e and the plastic deformation gradient F_{ij}^p [62]:

$$F_{ij} = F_{ik}^e F_{kj}^p \quad (4.1)$$

The slip systems β are specified by two vectors: the slip direction $s_i^{(\beta)}$ and the slip plane in the undeformed configuration $m_i^{(\beta)}$. Multiple slip systems are needed to describe the deformation of a UD ply or a tow in 3D analysis. It is assumed that the fibers are arranged in a close packing and the slip systems are constructed accordingly. A schematic of the slip systems in a tow can be seen in Figure 4.4 and their respective slip directions and slip plane normals are listed in Table 4.1.

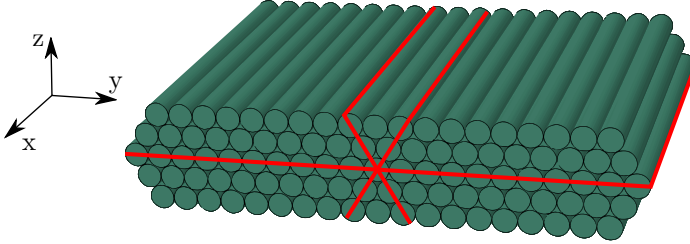


Figure 4.4: A close packing of fibers and the used slip systems indicated in red.

Table 4.1: Slip directions and slip plane normals for a UD ply or tow.

slip direction		slip plane normal	
$s^{(1)}$	$(1,0,0)$	$m^{(1)}$	$(0,0,1)$
$s^{(2)}$	$(1,0,0)$	$m^{(2)}$	$(0, \frac{\sqrt{3}}{2}, \frac{1}{2})$
$s^{(3)}$	$(1,0,0)$	$m^{(3)}$	$(0, \frac{\sqrt{3}}{2}, -\frac{1}{2})$
$s^{(4)}$	$(0,1,0)$	$m^{(4)}$	$(0,0,1)$
$s^{(5)}$	$(0, \frac{1}{2}, \frac{\sqrt{3}}{2})$	$m^{(5)}$	$(0, \frac{\sqrt{3}}{2}, \frac{1}{2})$
$s^{(6)}$	$(0, -\frac{1}{2}, \frac{\sqrt{3}}{2})$	$m^{(6)}$	$(0, \frac{\sqrt{3}}{2}, -\frac{1}{2})$

For the 2D case presented in this chapter, only one slip system is active in the warp tow. This slip system ensures that the homogenized fiber direction does not rotate with shear deformation. During deformation, the rotation of the slip direction and the

slip plane normal is dictated by the elastic deformation gradient:

$$s_i^{*(\beta)} = F_{ij}^e s_j^{(\beta)}, \quad m_i^{*(\beta)} = m_j^{(\beta)} (F_{ji}^e)^{-1}. \quad (4.2)$$

The plastic component of the deformation can be calculated using:

$$\dot{F}_{ik}^p (F_{kj}^p)^{-1} = \sum_{\beta=1}^N \dot{\gamma}^{(\beta)} s_i^{(\beta)} m_j^{(\beta)}, \quad (4.3)$$

where $\dot{\gamma}^{(\beta)}$ is the shear rate on slip system β . The plastic deformation, per slip system is determined by the resolved shear stress $\tau^{(\beta)}$:

$$\tau^{(\beta)} = s_i^{*(\beta)} \sigma_{ij} m_j^{*(\beta)}. \quad (4.4)$$

Most polymers have a yield stress that is dependent on the amount of hydrostatic pressure present. This pressure dependence is incorporated in the material model by taking the shear strength $g^{(\beta)}$ of slip system β a linear function of the pressure:

$$g^{(\beta)} = \begin{cases} \tau_y + \mu p & p \geq 0 \\ \tau_y & p < 0 \end{cases}. \quad (4.5)$$

In this equation, μ is the pressure sensitivity coefficient and p is a measure of the pressure transverse to the fiber direction. The pressure is calculated using terms of the 2nd Piola-Kirchhoff stress. For a tow with fibers placed in the local 11 direction, this pressure would be:

$$p = -\frac{1}{2}(S_{22} + S_{33}). \quad (4.6)$$

The S_{11} component is in this case not taken into account, as it is assumed that the stresses in this direction are dominated by the elastic fibers instead of the matrix. As a shear formulation, a rate dependent model similar to the one proposed by Asaro [62] is used:

$$\dot{\gamma}^{(\beta)} = \dot{\gamma}_0 \text{sign}(\tau^{(\beta)}) \left(\frac{\tau^{(\beta)}}{g^{(\beta)}} \right)^n \quad (4.7)$$

As within this Thesis, the rate dependent response of the fibrous composite materials is considered outside the scope of the research, the reference strain rate $\dot{\gamma}_0$ was set to be equal to the loading rate. Furthermore, the rate sensitivity exponent was set to $n = 5$ to approach the rate insensitive limit as much as possible without introducing numerical instabilities. The Crystal Plasticity model is implemented as a VUMAT subroutine in ABAQUS[®] explicit [55].

4.4 Tensile loading with Crystal Plasticity

The Crystal Plasticity based tow homogenization strategy is applied to the homogenized tows in the 2-layered homogenized plain weave specimen discussed at the beginning of this chapter. The elastic properties of the tows are taken the same as in the Hill plasticity simulations. The shear strength of the slip systems is set to be $\tau_y = \sigma_m^{y0}/\sqrt{3}$, where σ_m^{y0} is the initial yield stress of the matrix. As the yield stress of the matrix is insensitive to the hydrostatic pressure in the micro model and the

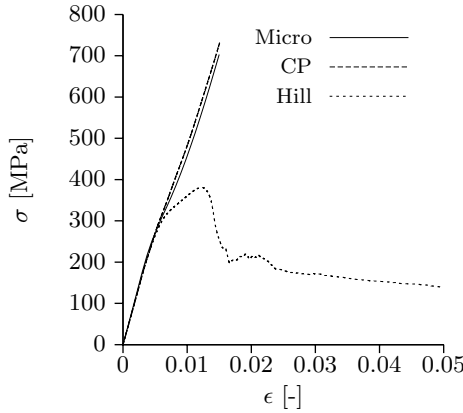


Figure 4.5: A comparison between simulations of a plain weave composites under tensile loading modeled with Hill plasticity and Crystal Plasticity. Both results are compared with the result obtained from a micro model where individual fibers were modeled.

Hill plasticity based model, the pressure sensitivity coefficient is set to $\mu = 0$ for the Crystal Plasticity simulation. The resulting stress strain curves are compared to those of the micro-model and the Hill plasticity based homogenization scheme in Figure 4.5.

Figure 4.5 shows that the stress-strain response of the Crystal Plasticity approach is similar to that of the micro model and the Hill plasticity approach. As the strains increase, the Crystal Plasticity model can be seen to display a similar nearly linear response as the micro model in stead of the highly non-linear response predicted when using the Hill plasticity approach. The local element orientations in the deformed warp tows of the plain weave simulation can be seen in Figure 4.6c. As the local element orientations do not change with plastic shear deformation, which is illustrated in Figure 4.6b, the stiff local element orientation remains aligned with the tow enabling a comparable stress strain response with respect to the micro model.

4.5 Conclusion

Within this chapter, two models with different homogenization strategies were compared to a micro model where individual fibers were modeled.

The accuracy of homogenization using Hill plasticity depends on the type of loading and the extent of the loading. The comparison between the stress-strain response showed that the Hill plasticity approach is accurate in the elastic regime. If the model undergoes plastic deformation in tension, the tows are stretched such that they align with the loading axis. The large deformations, and especially the rotations needed to stretch the tows, cause the Hill plasticity based model to be inaccurate.

If the model is loaded in compression, plastic deformation triggers the formation of kink-bands. The deformation localizes in the kink-bands and the regions outside of the kink-band do not undergo large deformations and rotations.

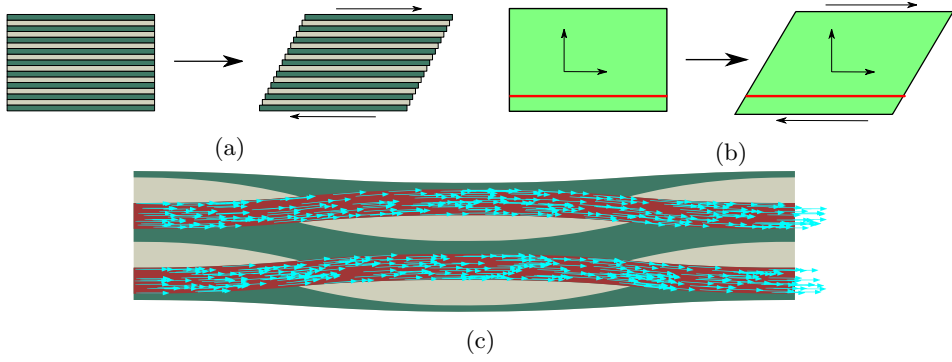


Figure 4.6: The difference in shear response between the micro model in Figure 4.6a and the Crystal Plasticity based homogenization with the slip plane indicated with the red line in Figure 4.6b. The local element orientations in the deformed warp tows are indicated with the blue arrows in Figure 4.3c.

Using a Crystal Plasticity model solves the inaccuracy when undergoing large deformations by making the rotation of the local element orientations independent of the plastic deformation and keeping the virtual fiber directions aligned with the tows. Once the model undergoes plastic deformation, the tows shear along the close packing planes and the orientation of these planes is not affected by the plastic deformation.

In the next chapter, the Crystal Plasticity based homogenization scheme is used to model 3DNOOBED composites under shear loading. This time, the performance of the Crystal Plasticity based and the Hill plasticity based tow-level homogenization will be evaluated by comparing the simulations with experiments.

Chapter 5

Shear failure in 3D non-woven carbon fibre composites

In this chapter, meso-scale models as derived in Chapter 3 are made using the Crystal Plasticity based tow-level homogenization method introduced in the previous chapter. The models are used to analyze the failure behavior of 3DNOOBED composites under shear loading. The accuracy of models using homogenization based on Hill plasticity and models using homogenization based on Crystal Plasticity is evaluated by comparing the simulations with experiments.

5.1 Introduction

The remarkable strength-to-weight performance of fiber composites, in particular carbon fiber reinforced polymer composites (CFRPs), has led to their extensive application in the fields of aerospace, automotive, and maritime engineering [63, 64, 65]. A vast majority of these fiber composites have a 2D architecture, and are fabricated as unidirectional, woven, or random sheets that are laminated with other sheets in a given preform. 2D laminated composites have many mechanical drawbacks, including poor interlaminar strength, buckling sensitivity, and a tendency for catastrophic failure [66, 67, 68, 69, 70].

Fiber composites can be designed with a 3D architecture in an attempt to overcome some of these limitations [71, 72, 73]. A wide range of 3D architectures have been created, including braided tubes and nozzles, multilayer woven sheets and beams and flanges with complex cross sections [74, 75, 76, 77]. These developments have successfully enabled 3D composites to overcome many of the vulnerabilities of laminated composites. Additionally, 3D composites have been found to exhibit many novel mechanical properties, including enhanced damage tolerance, resistance to compressive micro-buckling failure, and the capacity for large ductility and energy absorption [78, 79, 80, 81, 82]. These properties make 3D composites attractive for mechanical design purposes, but understanding the micro-mechanical origins of these attributes and reproducing them numerically has proven difficult.

Numerical models for the failure behavior of 3D composites generally incorporate either a maximum stress or a J2 plasticity criterion to determine the *onset* of failure [83]. These are often used in conjunction with continuum damage models that capture

the degradation of the mechanical properties. In the paper of Tan et al. [84], a maximum stress criterion was used to determine the failure limit of a micro-scale 3D unit cell. There, the micro-scale results were incorporated into a macro-scale model, resulting in good agreement with the longitudinal failure strengths of the large scale composite but only weak agreement with the transverse strength. Work by McGlokon et al. [85] used a reduced order binary model of tows and binder with a maximum stress criterion to model the accumulation of damage in a 3D composite. By incorporating friction into the damaged composite, this model captured the importance of interlock between the fibers in increasing 3D composite toughness. Song et al. [86] and Huang and Waas [87] used a transversely isotropic J2 plasticity model to capture the buckling response of a braided and z-pinned composite respectively. Both groups explicitly modeled tows in order to capture the compressive kink band failure behavior, but Huang and Waas [87] showed that explicitly modeling multiple unit cells led to a drop in the peak stress, better capturing the experimental response. In Das et al. [81], progressive micro-buckling in a 3D composite was modeled using a transversely isotropic Hill plasticity criterion. Correctly capturing the confined micro-buckling response required explicitly modeling the compression direction tows while modeling the transverse tows and matrix as a homogenized medium.

More detailed failure criteria have been developed for unidirectional (UD) and laminated composite materials. Work by Puck and Schrmann [88] describes the failure of a UD fiber composites using a physically based model that decouples axial fiber failure from transverse inter-fiber failure. In doing so, they define a failure envelope transverse to the fiber axis that accurately captures the tension-compression asymmetry and shear dominated failure of fiber composites. The accuracy and applicability of this method was later validated through a detailed series of micro-mechanical fiber-level simulations by Naya et al. [89]. Vogler et al. [90] developed an invariant based plasticity model that captures tension-compression asymmetry and shear dominated failure, additionally accounting for pressure dependent changes in the strength, and incorporating a non-associative flow rule for different loading directions to accurately predict the plastic Poisson's ratio.

Two often-neglected factors in the modeling of fiber composites are pressure dependent strengthening and large strain rotations of the fibers. It has long been known that pressure and large shear strains can have a pronounced effect on the properties of a composite [91, 92]. Models have been developed to capture the pressure dependent increase in strength of fiber composites, and these generally find that a linear increase in shear strength with increasing hydrostatic pressure is sufficient to capture the behavior [93, 94]. Models have also been created that capture the effect of fiber rotations in large shear strain environments. In work by Mandel et al. [95] and by Cui et al. [96], the material orientation of the fibers is explicitly rotated in a laminate as shear is being applied. In most models for UD and laminated fiber composites, pressure dependent strengthening and fiber rotation are ignored either because strains to failure are too low for their effects to contribute to the strength or because poor confinement does not allow for the build-up of any significant hydrostatic pressure.

In this work a special class of non-woven, orthogonally oriented (noobed) carbon fiber reinforced polymer (CFRP) composites [97, 98] is investigated. 3DNOOBED composites have a 3D architecture with tows aligned uniaxially in the x, y, and z directions and pockets of pure matrix filling the overlapping regions 5.1. Their architecture is unique from other 3D composites because there are no layers and it is

comprised of crimpless tows. It is also known as orthogonal nonwoven fabric, polar fabric, and xyz fabric [97]. The simplicity of 3DNOOBED composites makes them excellent model systems for studying fundamental mechanical phenomena that arise in 3D composite architectures.

5.2 Experiments

5.2.1 Materials and manufacturing

3DNOOBED composites were fabricated by weaving T700S carbon fiber tows (Toray composite Materials America Inc., USA) into a 3D fabric block that was then infused with NM FW 3070 epoxy [99] as the binder. The weaving method produced a non-crimp fabric that had tows oriented orthogonally in the x-, y-, and z-direction. After the woven pre-form was filled, solid matrix pockets formed in the overlapping regions between the tows. A unit cell of the 3NOOBED material can be seen on the right in Figure 5.1. The tows in a given direction were initially connected by loops on the outer edges of the block, but these were cut off in the sample preparation process. For samples tested in this work, the x- and y-direction tows were $\approx 12k$ fiber bundles with an average fiber volume fraction of 62.2%. The z-direction tows were $\approx 24k$ fiber-bundles with an average fiber volume fraction of 40.1%. Samples were provided in the form of large blocks ($\approx 200 \times 125 \times 50$ mm) by Biteam (Biteam AB). More details on the fabrication process can be found in [100].

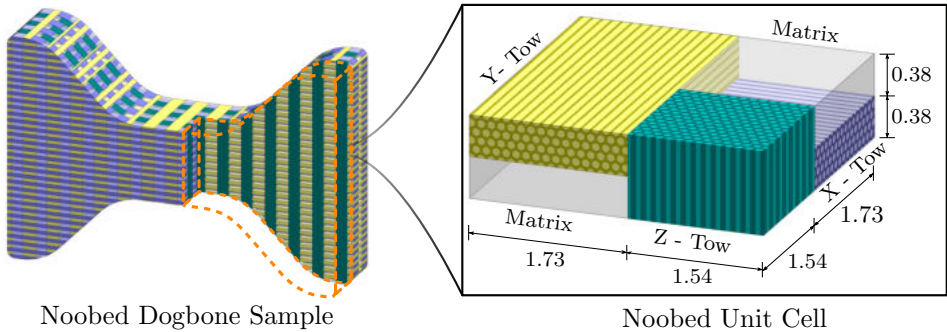


Figure 5.1: 3DNOOBED composite microstructure. A full scale CAD model of a 3DNOOBED dogbone specimen with a cut-out illustrating the internal structure on the left and on the right a 3DNOOBED unit cell showing the architecture and dimensions of the constituent tows. All dimensions are in mm.

Dogbone samples were prepared from the bulk 3DNOOBED block in two steps: first, a diamond cutting disk was used to cut ≈ 10 mm slices from the larger block, and second, a waterjet was used to cut dogbone samples from the slice. Some minor post-cut sanding was done with 120-grit SiC sandpaper to ensure the sample was the proper thickness and that there were good quality edge finishes. The total length and width of the dogbone samples was 45 mm and 30 mm respectively, and the gauge section was set to be roughly $10 \times 10 \times 10$ mm. Two orientations of composite were used. In orientation the z-tows were oriented perpendicular to the shearing axis. This orientation is referred to as the xz orientation. In the other orientation the z-

tows were parallel to the shearing axis. The latter orientation is referred to as the zx orientation. Both orientations are shown in Figure 5.2. The dogbone geometry does not impose an ideal state of shear, but it was chosen so that shear could be applied to a representative number of unit cells in the sample.

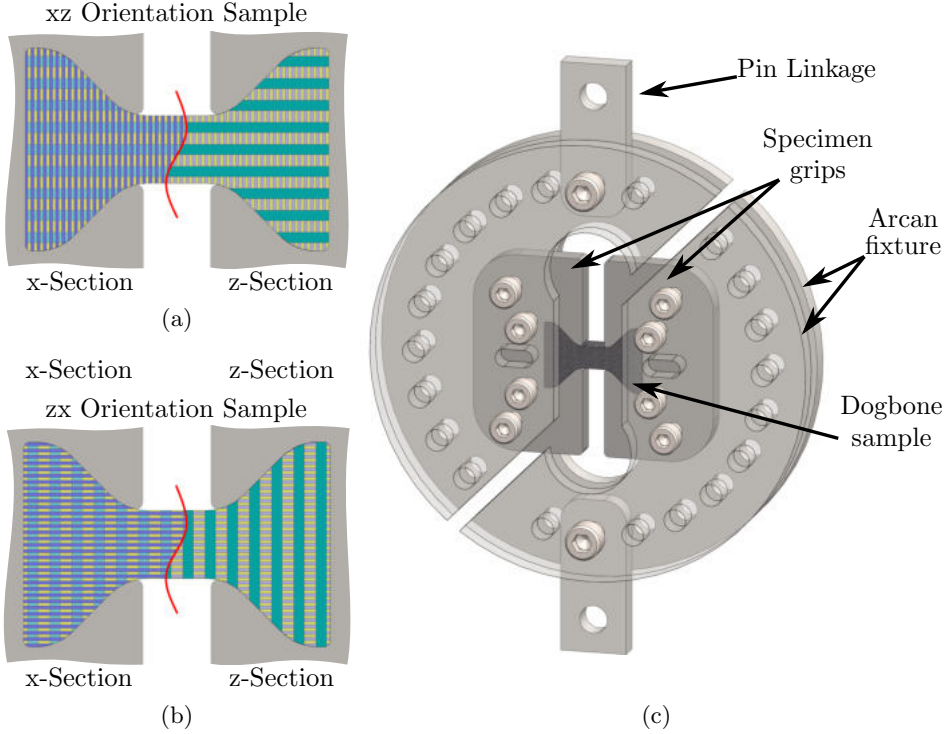


Figure 5.2: Mechanical testing setup. (a) xz and (b) zx orientation 3DNOOBED dogbone samples showing two different sections of the microstructure. (c) Arcan fixture used in the testing of the composites. The front plates of the fixture are transparent to better illustrate the setup.

5.2.2 3DNOOBED microstructure

Figure 5.1 shows the micro-structure of two representative 3DNOOBED composite samples with xz and zx orientations. Images were obtained using X-Ray computed tomography (CT) scanning performed in an X-Tek XTH 225ST system (Nikon Metrology UK Ltd.). It can be seen that the x- and y-direction tows were nearly identical and had high aspect ratio rectangular cross sections with dimensions of 0.38×1.73 mm. The z-direction tows had a rounded square cross section with overall dimensions of 1.54×1.54 mm. The profile of the z-tows can be approximated as a superellipse with exponent $n = 4$.

There was some global waviness along the length of the x- and y-tows. This waviness had an amplitude of 0.06 mm along the z-axis and 0.11 mm along the x- and y-axis respectively. Due to this waviness, the fiber volume fraction varied along the length of the x- and y-tows between 58.6% and 67.6%. Although the tows in the

z-direction did not have any significant global waviness, they had an internal waviness that was greater than that of the x- and y-tows. Quantifications of the waviness of the tows can be found in Appendix B.

Large locally cracked regions existed in the samples prior to mechanical testing (5.1). They appear to have initiated as debonded areas between the tows, after which they either spread into matrix pockets or connected with other locally cracked areas to form larger planes. Cracks that propagated into matrix pockets deviated away from the tow and toward the center of the pocket, sometimes leading to wavy debonded planes when multiple cracks interacted. The xy-plane had larger debonded areas that formed when cracks between the x- and y-direction tows connected; tows in the z-direction intersected these, creating a perforated crack plane. Larger debonded areas also formed along the length of the z-direction tows. These often formed on two or three different sides of the z-tows, resulting in a near complete debonding between them and the rest of the composite. Detailed microscope images of the tows can be found in Appendix B.

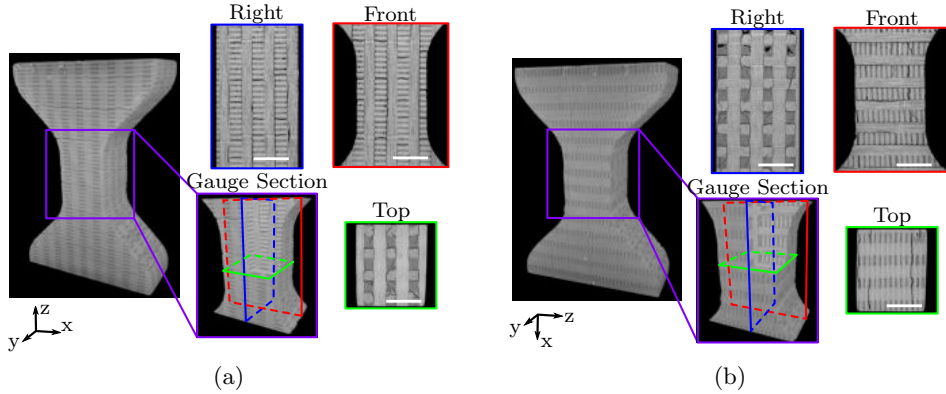


Figure 5.3: X-Ray CT scans. Representative images of the untested 3DNOOBED specimens with A) xz and B) zx orientations. Cut sections show different projections of the microstructure and illustrate the pre-existing damage in the composite. The white scale bars are all 5 μm .

5.2.3 Experimental setup

Mechanical testing was performed in an Instron 5985 testing device (Instron Corp., USA) and a 250kN load cell was used to measure the force. An Arcan fixture was used to apply a state of shear, and samples were coupled to the fixture through mild steel grips that had been machined to fit the dogbone profile. An overview of the setup can be seen in Figure 5.2c. This type of setup is commonly used to measure the shear response of different composites [101, 102]. The fixture was connected to the load cell via a pin linkage, which allows samples to translate in the direction perpendicular to the loading axis during testing. This loading setup results in a state of mixed pure and simple shear in the samples, but it prevents any premature axial stretching that will take place in a rail shear testing setup.

An ARAMIS 12M 3D-DIC setup (GOM GmbH) was used to study the surface-level stress concentrations that arose in the sample during testing. DIC images of the

xz- and zx-orientation samples taken at 35% strain and at final failure can be seen in Figures 5.4b, 5.4c, 5.4e, and 5.4f. The DIC images were also used to track the displacement of the sample in the gauge section, thereby eliminating the effect of any compliance in the Arcan fixture. A random speckle pattern for DIC was generated and applied to the sample using photo transfer paper (Photo Paper Direct Ltd.). This was done to ensure consistency in the quality of the speckle pattern between samples.

Uniaxial loading experiments were performed in one of two ways: 1) samples were taken to moderate (30–45%) shear strains and then fully unloaded, and 2) samples were loaded in shear until the onset of ultimate failure. Loading and unloading were performed at rates of 0.3 mm/min, corresponding to strain rates in the gauge section of $5 \times 10^{-4} \text{ s}^{-1}$. The shear strain is calculated by normalizing the vertical displacement by the 10 mm gauge length, and shear stress is calculated by normalizing the applied load by the cross sectional area of the specimen in the gauge section ($\approx 100 \text{ mm}^2$). The shear stiffness is calculated using the slope of the initial loading curve, and the shear strength is determined using a 0.2% strain offset. Representative stress-strain curves are shown in Figure 5.4a and 5.4d for the xz- and zx-experiments respectively.

Cyclic loading experiments were performed by gradually taking samples up in increments of strain and unloading to a fixed stress of 1 MPa before finally fully unloading after reaching 30–40% strain. Samples were loaded to 1%, 2.5%, and 4.5% strain before being loaded in continuous increments of 3.5% strain. Loading and unloading were performed at rates of $5 \times 10^{-4} \text{ s}^{-1}$. The unloading stiffness was calculated by fitting a fifth order polynomial to the unloading data - or an $(n - 1)^{\text{th}}$ order polynomial if there were $n \leq 5$ data points to fit - and finding its slope at the point of unloading. A polynomial fit of this type provides the most consistent results across all the samples.

5.2.4 Experimental results

The uniaxial and cyclic loading of two different orientations of 3DNOOBED composite samples are examined in the next section along with the damage and failure landscapes before and after testing. The stress-strain response of all samples was initially linear, and after the onset of plasticity, there was a large hardening response, as can be seen in Figures 5.4a and 5.4d). Some of the intrinsic (material) and extrinsic (structural) factors in the 3DNOOBED composites are discussed that likely contribute to the hardening behavior observed in the experiments. DIC maps illustrate the anisotropic development of strain on the surface of the samples and indicate regions of failure. X-Ray CT images of the samples before and after testing demonstrate the minimal degree of damage propagation, even for samples taken to ultimate failure. Cyclic testing shows a stiffening behavior at large strains, further demonstrating both the integrity of the 3DNOOBED composites and their resistance to damage accumulation.

xz Orientation uniaxial shear

3DNOOBED specimens loaded in the xz orientation have initial shear moduli of $G = 265 \pm 22 \text{ MPa}$, and began to yield at shear stresses of $\tau_y = 7.8 \pm 0.4 \text{ MPa}$. After yielding, the samples have a small plateau in their stress-strain response before they begin to harden considerably. This hardening continues across the entire strain range with a nearly constant slope until the onset of failure. The hardening slope is $G_h = 130 \pm 3 \text{ MPa}$, which is roughly half the initial loading slope. Samples that were unloaded prior to failure were taken to peak strains of $\epsilon_{\text{max}} = 30 - 33\%$. These samples recover

to strains of $\epsilon_{\text{final}} = 13 - 17\%$ after unloading, constituting a recovery of 48 – 60%. In samples that were taken to ultimate failure, the failure occurs at strains of $\epsilon_{\text{ult}} \cong 42\%$ and stresses of $\sigma_{\text{ult}} \cong 55$ MPa. The catastrophic failure occurs via tensile rupture of the z-direction tows. The peak strengths of the samples is ≈ 7 times higher than the initial yield strength. A small number of audible failure events were detected prior to ultimate failure, but they occurred near the ultimate failure strain.

Figure 5.4b and 5.4c show the equivalent strains of the z- and x-sections respectively of two different samples analyzed using DIC. The equivalent strain ϵ_{eq} is defined as:

$$\epsilon_{\text{eq}} = \sqrt{\frac{2}{3} e_{ij} e_{ij}} \quad (5.1)$$

where e_{ij} is the deviatoric component of the strain. In both Figures, regions of high strain directly coincide with cracked areas of the sample, and the large relative motion of the cracked interface leads to an exaggerated strain response. In Figure 5.4b, the large horizontal strains correspond with cracks along the z-tows, which tend

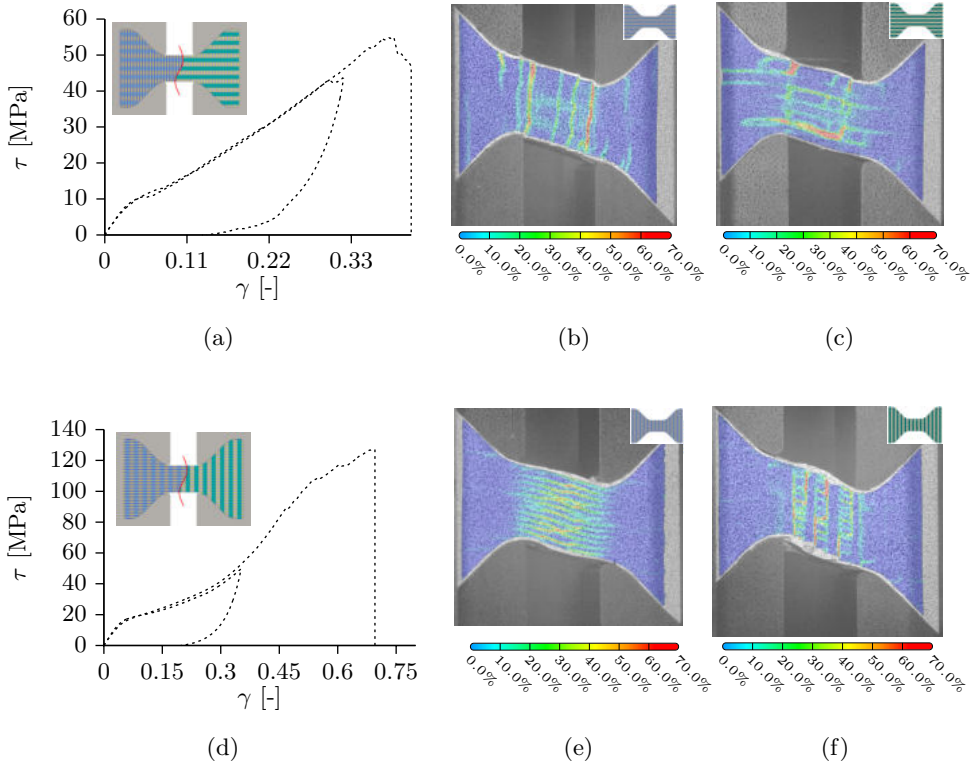


Figure 5.4: Representative stress-strain curves of the (a) xz and (d) zx oriented samples tested to $\approx 35\%$ strain and tested to failure. DIC plots show the equivalent Mises strain field in x- and z-sections respectively of the (b)/(c) xz and (e)/(f) zx oriented samples at $\epsilon = 32\%$ applied strain. Insets in the DIC figures are intended to help illustrate the section of the sample being shown.

to slip under the applied shear, and the large vertical strains correspond with cracks between the y-tows and the matrix pockets, which tend to close under the applied shear (Figure 5.5a and Figure 5.6b). The only cracks that open are those in tension near the corners of the gauge section. Smaller strain concentrations appear away from the cracked areas in the regions between the x- and y-direction tows, indicating that there are large stress concentrations between the tows even in regions where there is no cracking. In Figure 5.4c, the large strains in the vertical direction correspond to cracks between the x- and y-tows, which tend to close under the applied shear (Figure 5.5b and Figure 5.6b). There are moderate strain concentrations that arise away from the cracked areas in regions between the x-tows and the matrix pockets, but there is no visible damage in post-test CT scans of these areas, suggesting that any permanent deformation that occurred there was plastic and did not involve cracking.

zx Orientation uniaxial shear

The specimens loaded in the zx orientation had initial shear moduli of $G = 365 \pm 29$ MPa and yielded at shear stresses of $\tau_y = 11.5 \pm 1.2$ MPa. After yielding, there was a large drop in the loading stiffness that resulted in a plateau in the stress of some of the samples. As greater strains were applied, there was a substantial and continuous increase in the hardening response. Samples that were unloaded prior to failure were taken to peak strains of $\epsilon_{\max} = 35 - 43\%$, and these samples recovered to strains of $\epsilon_{\text{final}} = 17 - 20\%$ after unloading, constituting a recovery of between 50 – 52%. The observed hardening continued to increase until $\approx 45\%$ strain, at which point some audible failure events began to occur and the sample continued to harden but at a less drastic rate, eventually experiencing ultimate failure at $\epsilon_{\text{ult}} \cong 70\%$. This failure occurred catastrophically via rupture of the x-direction tows at a peak strength of $\sigma_{\text{ult}} \cong 125$ MPa, which is over an order of magnitude stronger than the initial yield strength. Within the last 15% strain prior to ultimate failure, some of the outermost x- and y-direction tows delaminated and slid off the z-direction tows holding them together (Figure 5.8b).

Figure 5.4e and 5.4f show the Mises strains of the z- and x-sections respectively of two different samples analyzed using DIC. The observed strain concentrations do not overlap solely with cracked regions of the samples, and instead arise more broadly in areas of local anisotropy. In Figure 5.4e, the vertical strain concentrations correspond to the cracked profile of the z-tows, which are observed to have slipped under the applied shear (Figure 5.7b and Figure 5.8b), but the horizontal strain concentrations arise between the y-tows and the matrix pockets due to the local anisotropy in the stiffness. In Figure 5.4f, the horizontal strain concentrations strongly align with the x-tows. These large strains eventually lead to some longitudinal cracking in the x-tows and debonding between the x- and y-tows (Figure 5.7a and Figure 5.8a). The absence of cracking in many of the observed regions of large strain suggest that the composite is either experiencing large plastic straining or sustaining large local stresses without failure.

xz Orientation X-ray CT imaging

Figure 5.5 shows two different X-Ray CT sections of an xz orientation sample before and after being sheared to 32% strain. A number of defects were present in the sample prior to testing; these existed as large xy-plane cracks and long debonded areas around

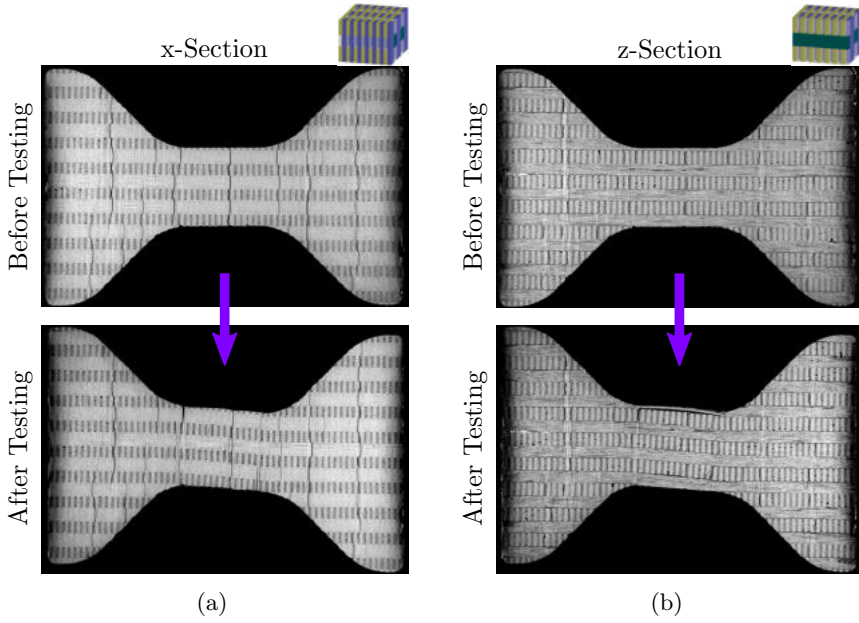


Figure 5.5: Damage in xz orientation 3DNOOBED composite. Before and after X-Ray CT images of the (a) x- and (b) z-sections of an xz orientation 3DNOOBED composite tested to 32% strain.

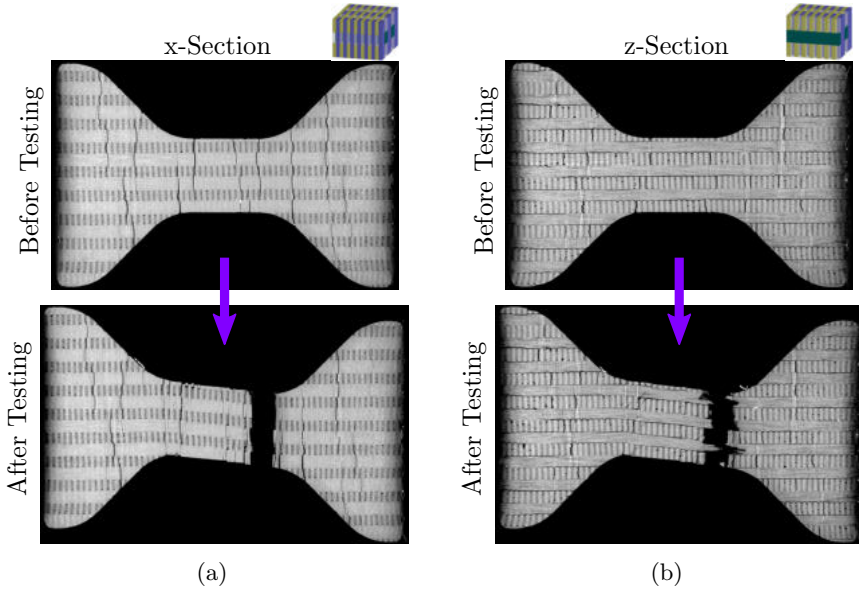


Figure 5.6: Failure of xz orientation 3DNOOBED composite. Before and after X-Ray CT images of the (a) x- and (b) z-sections of an xz orientation 3DNOOBED composite tested to failure.

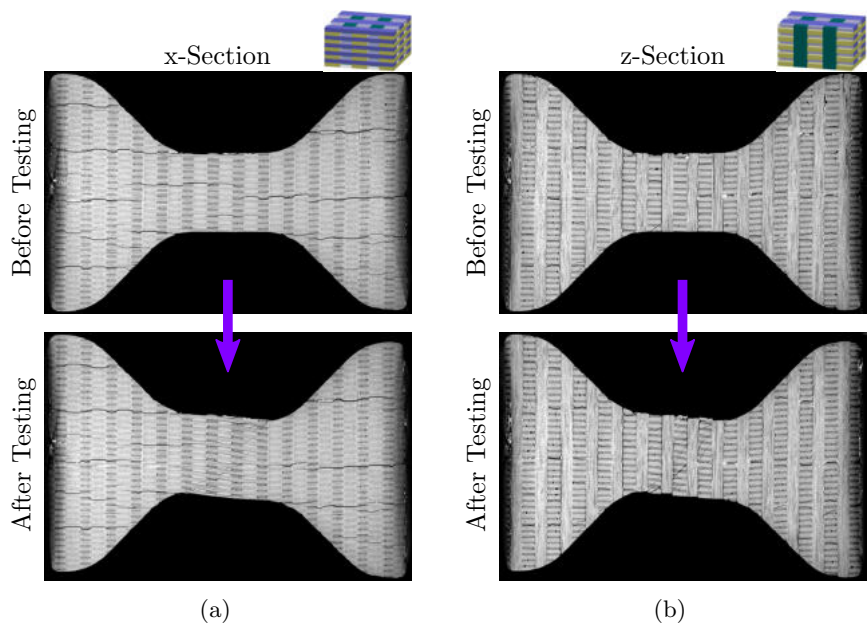


Figure 5.7: Damage in xz orientation 3DNOOBED composite. Before and after X-Ray CT images of the (a) x- and (b) z-sections of an xz orientation 3DNOOBED composite tested to 32% strain.

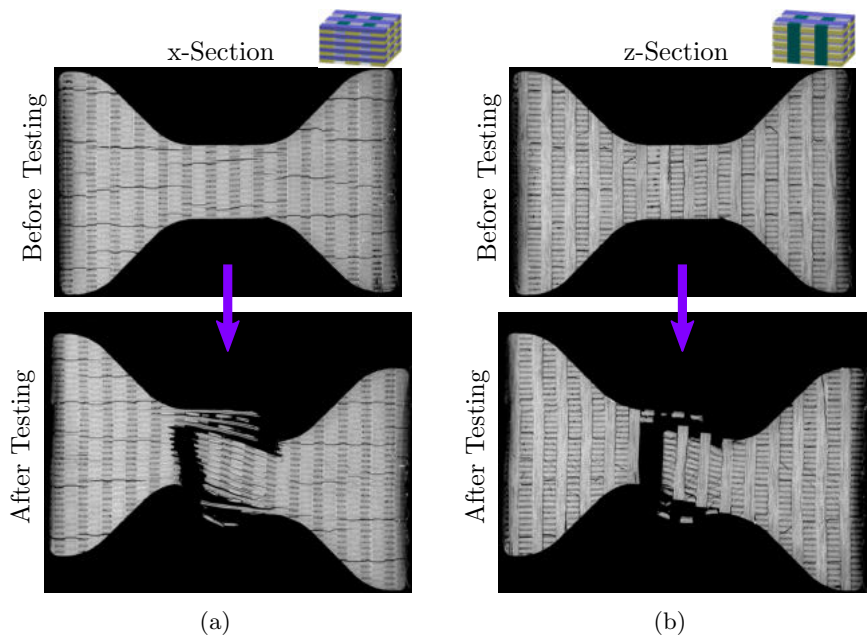


Figure 5.8: Failure of xz orientation 3DNOOBED composite. Before and after X-Ray CT images of the (a) x- and (b) z-sections of an xz orientation 3DNOOBED composite tested to failure.

the z-tows. After testing, the xy-plane cracks in the gauge section tended to slip and close (Figure 5.5a). There was both minor propagation of the existing cracks and new cracks that formed near the tensile area of the gauge section, but the majority remained stationary. Cracks along the z-tows tended to coalesce and propagate, causing larger debonded areas to form (Figure 5.7b). There was some delamination of the z-tows along the edges of the gauge section due to the cracking.

In areas of the sample that were not cracked, there was very little visible accumulated damage. There was some shear splitting perpendicular to the axis of the tows in the y-direction, but this type of damage was limited to z-sections of the sample (Figure 5.5b). There was also some visible kink band formation in the compressive region of the gauge section in the z-tows, but these kinks were limited to small regions and did not propagate through the tow. It is likely that most of the plasticity in the sample was limited to matrix pockets, and plasticity that did occur in the tows was below the cracking threshold.

Figure 5.6 shows two different CT sections of an xz orientation sample before and after testing to failure. The samples in Figure 5.5 and Figure 5.6 showed the same degree of damage after testing, with the exception that the intact sections of the z-tows had a more pronounced permanent bend. The failure of the sample occurred via fracture of the z-tows near the edge of the gauge section along one of the xy-plane cracks. The failed z-tows had an irregular fiber breakage and pull-out that is characteristic of carbon fiber composite fracture (Figure 5.6). In some areas of the sample, the z-tows fully delaminated and pulled out of the surrounding composite entirely. There was very little visible permanent damage in the sample other than the ruptured tows.

zx Orientation X-ray CT imaging

Figure 5.7 shows X-Ray CT sections of an zx orientation sample before and after being sheared to 35% strain. The zx and xz orientation samples had a similar initial defect structure, they were just rotated 90° relative to each other. After testing, the xy-plane cracks in the gauge section tended to close, and they underwent no visible propagation (Figure 5.7a). The only new cracks that formed in this direction were in the x-tows at the outer edges of the gauge section, where there was some minor visible delamination. Cracks along the z-tows propagated and strongly slipped. Some areas of the z-tows completely slid out of the surrounding composite, particularly near the edges of the gauge section (Figure 5.7b).

There was a moderate amount of damage accumulated locally in the tows. Some of the x-tows split in their midsection along the fiber axis, particularly in the compressive region of the gauge section (Figure 5.7a). These splitting events did not propagate through the tows or extend into the surrounding matrix. There were also local shear cracking events in the y-tows in the gauge section perpendicular to the fiber axis (Figure 5.7b). These sometimes propagated through matrix pockets and intersected multiple tows. These cracks did not propagate into the x- or z-tows, although they did often continue along the full length of the y-tows. No visible damage accumulated internally in the z-tows.

Figure 5.8 shows CT sections of a zx orientation sample before and after testing to failure. Similar types of damage existed between the samples in Figure 5.7 and Figure 5.8, but the damage in the failed sample had developed to a much greater degree. Splitting in the x-tows propagated further along their length, and there was

moderate accumulated shear damage both in the y-tows and in the matrix surrounding it. There was more severe delamination of the x-tows, so much so that some of the x-tows entirely slid off the z-tows confining them. The cracks along the z-tows did not propagate down their length and remained confined to the outer edges of the gauge section. The failure of the sample occurred via fracture of the x-tows along the two different ends of the gauge section; delaminated tows failed on one end, while tows that had not delaminated failed on the other end. The failed tows had the same irregular breakage and pull-out that is characteristic of carbon fiber composite fracture. In the z-section failed areas, there was a clean fracture between the y- and z-tows.

Cyclic loading

Figure 5.9 shows the stress-strain response of loading and unloading cycles of the 3DNOOBED composites and shows the corresponding unloading stiffnesses E_{unload} as a function of applied strain. Both sample orientations showed a gradual increase in the unloading stiffnesses that mirrored the hardening response in uniaxial loading. The unloading stiffness of the xz orientation samples monotonically increased across the entire strain range which can be seen in Figure 5.9c. There was initially a small jump in the stiffness from $G_{\text{unl}} = 0.26$ GPa at 1% strain to $G_{\text{unl}} = 0.44$ GPa at 2.5% strain, after which there was a nearly linear stiffening to $G_{\text{unl}} = 1.22$ GPa at 32% strain. The zx orientation samples had a long plateau in their unloading stiffness before stiffening considerably as indicated in Figure 5.9d. The initial unloading stiffness remained around $G_{\text{unl}} = 0.70 \pm 0.04$ GPa until 20% strain, after which there was a linear stiffening to $G_{\text{unl}} = 0.96$ GPa at 35% strain. The observed stiffening was primarily due to the reorientation of the axial tows in the sample. In a traditional laminated composite, there would also be a reorientation stiffening in shear, but damage would normally lead to a knockdown in the stiffening response.

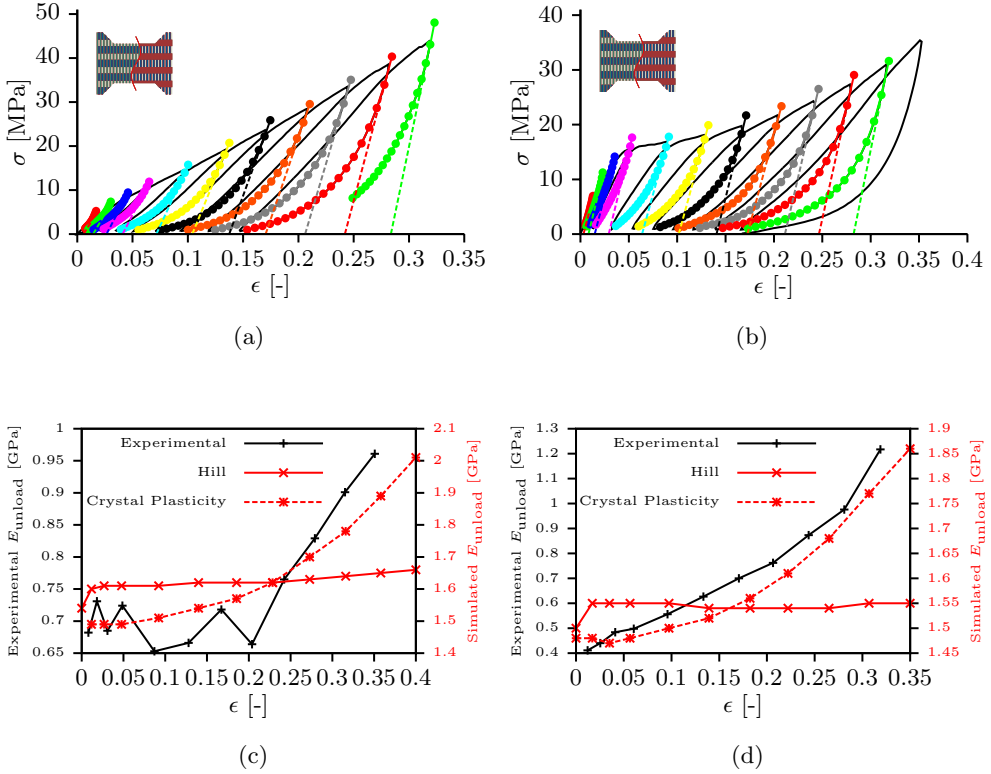


Figure 5.9: Cyclic testing. Stress-strain curves of (a) xz and (b) zx oriented 3DNOOBED composites illustrate the loading/unloading behavior. Colored sections indicate the regions of the curve used in the unloading fit, and dashed lines indicate the unloading stiffness fits. The unloading stiffness as a function of increasing strain is shown for the (c) xz and (d) zx orientations.

All of the unloading cycles for each of the samples showed a considerable hysteresis. In each of the loading cycles outside of the elastic regime (i.e. $\epsilon_{app} > 10\%$), both samples recovered between 48% - 65% strain when they were unloaded to 1 MPa. The amount of recovery gradually decreased as larger strains were applied to samples, but it remained consistently high throughout the entire strain range. This consistent and considerable recovery suggests that there is minimal damage accumulation throughout the deformation of the sample, and that much of the global stress response is accommodated through hydrostatic compression of the tows. These results suggest composite damage models that make use of unloading stiffnesses to measure property degradation are inappropriate for analyzing the 3DNOOBED composite materials.

5.3 Computational modeling

In the following sections, the geometric details and the constitutive models used to simulate the shear samples are discussed.

5.3.1 Numerical model design

The architecture of 3D fiber composites is intrinsically complex, and multiple material and defect length scales govern their global behavior. Creating homogenized models that accurately capture 3D composite behavior is correspondingly difficult, and no homogenized model exists today that can reproduce the large strain elastic-plastic behavior observed in the 3DNOOBED samples studied in this work. To work around this, a tow level numerical model, similar to those in Chapter 3 and the Crystal Plasticity model in Chapter 4, is developed of the gauge section of the sample and a small grip region above and below it. In this, all the tows and matrix pockets are explicitly modeled using dimensions obtained from samples. The constituent tows and matrix regions are constructed as rectangular prisms made of hexahedral elements (C3D8). An overview of the model can be seen in Figure 5.10a. Material properties and orientations are assigned on an element level. All coinciding nodes in the model, both between tows and between tows and matrix pockets, are merged to create a single solid body. There are no tie constraints or cohesive surfaces used.

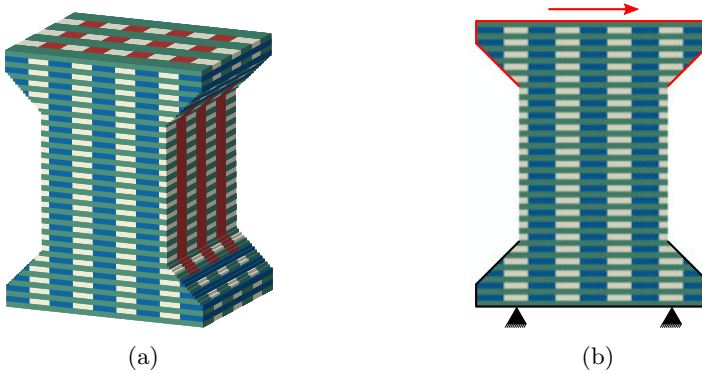


Figure 5.10: (a) Representative image of an xz orientation 3DNOOBED composite with all tows and matrix pockets explicitly modeled. (b) Front view of xz orientation model showing the boundary conditions.

The number of physical features and material properties in the model are kept to a minimum so that the salient properties affecting the experimental behavior can be determined. The ends of the dogbone sample are excluded because the low stress and minimal damage seen in them experimentally suggest that they do not have a significant impact on the global mechanical response. Attributes such as cracks and cohesive debonding zones between tows are also excluded from the model because their impact on the performance can be reasonably reproduced by modifying other material properties.

All calculations are performed using the commercial finite element software package ABAQUS[®]. The simulations are run using ABAQUS[®] explicit while assuming large deformations and mass scaling to a target time increment of 10^5 of the total time such that $E_{\text{kinetic}}/E_{\text{internal}} < 5\%$. A rigid body constraint is applied to nodes along the upper and lower edge regions of the sample to form a top and bottom 'grip' respectively. The boundary conditions can be seen in Figure 5.10b. The bottom grip is fixed and a constant rate shear velocity is applied to the top grip with an initial rate smoothing step of $\epsilon_{\text{smooth}} = 0.4\%$ to prevent any numerical instability artifacts. This smoothing

is applied to both loading and unloading. The axial displacement of the top nodes is unconstrained; this is done in to match the conditions in the experimental setup. The models consist out of approximately $2 \cdot 10^6$ elements and has approximately $8 \cdot 10^6$ degrees of freedom. Each tow has at least 4 elements across its minimum dimension. Convergence studies were performed to ensure the time step and element size were sufficiently small. Depending on the applied strain, the time step was adjusted such that a number of $1 \cdot 10^5$ steps were used to calculate the results.

5.3.2 Material models

The elastic properties of the NM FW 3070 epoxy matrix and of the T700S carbon fibers were obtained from data sheets [99, 103], and the matrix and fibers were both taken to be isotropic media. It has been shown that the T700S carbon fibers are transversely isotropic [104], but the addition of fiber anisotropy in these models had a negligible effect on the resulting mechanical properties of the composite. Table 5.1 lists the constituent material properties used in the model.

Table 5.1: Constitutive properties of the fibers and matrix

T700S Carbon fiber			NM FW 3070 Epoxy				
E_f	ν_f	σ_f	E_m	ν_m	σ_m	τ_y	μ
230 GPa	0.28	4.9 GPa	2.70 GPa	0.3	17.3 MPa	10 MPa	0.2

In shear, the plastic behavior of a unidirectional fiber composite is governed primarily by the properties of the matrix [88, 89, 105, 106]. Two properties are used to approximate the plastic response of the tows and matrix: the shear yield strength τ_y and the pressure dependent strengthening coefficient μ . These parameters are used for both the strength of a tow slip plane and the isotropic shear strength of the matrix. While the tow and matrix shear strengths likely differ from each other, and the tow strengths are dependent on fiber volume fraction and failure direction, all the strengths are set to be equal here for the sake of studying the effect of geometric anisotropies on mechanical performance. The best fit shear yield strength is determined to be $\tau_y = 10$ MPa, which is slightly lower than the shear strength of the epoxy obtained from data sheets, but it effectively represents a knockdown in the properties due to imperfections like voids and cracks. The best fit pressure strengthening coefficient is determined to be $\mu = 0.2$, which is similar to hardening coefficients for other polymers found in literature [107]. The pressure sensitivity of the tows and matrix is set to be equal because it is assumed to arise from the pressure dependence of the constituent matrix and not to be affected by the granularity of the tows. The effect of varying τ_y and μ on the results can be found in Appendix B. Quantification of the effect of different shear strengths for the slip directions and a varying fiber volume fraction along the tow requires in-depth studies that are considered beyond the scope of this work.

Matrix material model

The pure matrix material is modeled using a linear Drucker-Prager model in ABAQUS[®]. A non-dilational matrix is modeled by setting the dilation angle to $\phi = 0$, and the Von-Mises yield surface is assumed to be a circle on the deviatoric plane ($K = 1$).

The pressure dependent strengthening coefficient μ is related to the friction angle β in the Drucker-Prager model as $\beta = \arctan(\mu)$. The matrix is modeled as an elastic, perfectly plastic material in the sense that there is no strain hardening applied.

Tow elastic properties

The elastic properties of the tows are determined using the constitutive properties of the fibers and matrix. The average fiber volume fraction V_f is used to assign properties for the entire tow; there is no volume fraction variation along the length to account for waviness. The uniaxial stiffness and Poissons ratio are determined using a Voigt average, and the transverse stiffnesses and shear stiffnesses are determined using a Halpin-Tsai model [108] and stiffness equilibrium relationships. The transverse Poissons ratio is determined using a Clyne model [109]. The bulk modulus of the tow is determined using a Reuss average. Equations for the elastic properties of a tow with the fibers oriented in the axial 1-direction are shown below. The final tow properties can be found in Table 5.2.

$$E_1 = E_f V_f + E_m (1 - V_f) \quad (5.2)$$

$$E_2 = E_3 = E_m \frac{1 + \eta \xi V_f}{1 - \eta V_f}, \eta = \frac{\frac{E_f}{E_m} - 1}{\frac{E_f}{E_m} + \xi}, \xi = 2 + 40V_f^{10}, \quad (5.3)$$

$$G_{12} = G_{13} = G_m \frac{1 + \eta \xi V_f}{1 - \eta V_f}, \eta = \frac{\frac{G_f}{G_m} - 1}{\frac{G_f}{G_m} + \xi}, \xi = 1 + 40V_f^{10}. \quad (5.4)$$

$$\nu_{12} = \nu_f V_f + \nu_m (1 - V_f) \quad (5.5)$$

$$\nu_{21} = \nu_{12} \frac{E_2}{E_1} \quad (5.6)$$

$$\nu_{23} = 1 - \nu_{21} - \frac{E_2}{3K_t}, \quad (5.7)$$

$$K_f = \frac{E_f}{3(1 - 2\nu_f)}, \quad (5.8)$$

$$K_t = \left(\frac{V_f}{K_f} + \frac{1 - V_f}{K_m} \right)^{-1} \quad (5.9)$$

Table 5.2: Elastic properties of the Tows

Tow	E_1	E_2, E_3	G_{12}, G_{13}	G_{23}	ν_{12}	ν_{21}	ν_{23}
X/Y	144 GPa	16.2 GPa	4.79 GPa	3.09 GPa	0.288	0.018	0.451
Z	93.6 GPa	14.9 GPa	4.27 GPa	1.96 GPa	0.292	0.018	0.460

Tow plasticity model

The Hill plasticity approach

The Hill plasticity approach used for the tows in the 3DNOOBED composites is the same as the approach used for the tows in the 2D plain weave models presented in chapter 3. Within Hill plasticity, an anisotropic yield potential is defined as:

$$f(\boldsymbol{\sigma}) = (F(\sigma_{22} - \sigma_{33})^2 + G(\sigma_{33} - \sigma_{11})^2 + H(\sigma_{11} - \sigma_{22})^2 + 2L\sigma_{23}^2 + 2M\sigma_{31}^2 + 2N\sigma_{12}^2)^{\frac{1}{2}}. \quad (5.10)$$

If the yield stress values $\bar{\sigma}_{ij}$ are the yield stress values of the material under a loading state where σ_{ij} is the only non-zero stress, the ratios F, G, H, L, M and N can be determined using [57]:

$$F = \frac{\sigma^0}{2} \left(\frac{1}{\bar{\sigma}_2^2} + \frac{1}{\bar{\sigma}_2^2} - \frac{1}{\bar{\sigma}_1^2} \right) \quad (5.11)$$

$$G = \frac{\sigma^0}{2} \left(\frac{1}{\bar{\sigma}_2^2} + \frac{1}{\bar{\sigma}_1^2} - \frac{1}{\bar{\sigma}_2^2} \right) \quad (5.12)$$

$$H = \frac{\sigma^0}{2} \left(\frac{1}{\bar{\sigma}_1^2} + \frac{1}{\bar{\sigma}_2^2} - \frac{1}{\bar{\sigma}_2^2} \right) \quad (5.13)$$

$$L = \frac{3}{2} \left(\frac{\tau^0}{\bar{\sigma}_{23}} \right)^2 \quad (5.14)$$

$$M = \frac{3}{2} \left(\frac{\tau^0}{\bar{\sigma}_{13}} \right)^2 \quad (5.15)$$

$$N = \frac{3}{2} \left(\frac{\tau^0}{\bar{\sigma}_{12}} \right)^2 \quad (5.16)$$

where σ^0 is a reference yield stress and $\tau_0 = \sigma^0/\sqrt{3}$ is the corresponding reference shear yield stress. The axial strength σ_1 and the transverse strength σ_2 of the tows were calculated using the Voigt and Reuss rule of mixtures respectively, and the shear strengths were all set to be equal to the shear strength of the matrix τ_y .

$$\bar{\sigma}_1 = \sigma_f V_f + \sigma_m (1 - V_f), \quad (5.17)$$

$$\bar{\sigma}_2 = \left(\frac{V_f}{\sigma_f} + \frac{1 - V_f}{\sigma_m} \right)^{-1}, \quad (5.18)$$

$$\bar{\sigma}_{12} = \bar{\sigma}_{13} = \bar{\sigma}_{23} = \sqrt{3}\tau_y. \quad (5.19)$$

The plastic strain evolves according to the flow rule:

$$d\epsilon^{pl} = d\lambda \frac{\partial f}{\partial \boldsymbol{\sigma}} \quad (5.20)$$

Tow Crystal Plasticity model with pressure dependent hardening

The Crystal Plasticity approach used to model the tows is similar to the model presented in Chapter 4. The most important features of the model are discussed below.

In Crystal Plasticity, the deformation gradient F_{ij} is written as a multiplicative decomposition of the elastic deformation F_{ij}^e and plastic deformation F_{ij}^p as:

$$F_{ij} = F_{ik}^e F_{kj}^p. \quad (5.21)$$

Each slip system β is specified by two vectors, one which defines the slip direction ($s_i^{(\beta)}$), and one that defines the normal vector to the slip plane in the undeformed configuration ($m_i^{(\beta)}$). These vectors rotate with the principle fiber axis so that in the deformed configuration they become:

$$s_i^{*(\beta)} = F_{ij}^e s_j^{(\beta)}, \quad m_i^{*(\beta)} = m_j^{(\beta)} (F_{ji}^e)^{-1}. \quad (5.22)$$

$N = 6$ slip systems are defined that represent the shear failure directions of the 3DNOBED composites. The slip directions and slip plane normal vectors in the undeformed configuration for an x-direction tow are listed in Table 5.3. The slip systems $\beta = 1, 2, 3$ correspond to longitudinal shear failure, and the slip systems $\beta = 4, 5, 6$ correspond to transverse shear failure.

Table 5.3: Slip directions and slip plane normals for a UD ply or tow.

slip direction		slip plane normal	
$s^{(1)}$	(1,0,0)	$m^{(1)}$	(0,0,1)
$s^{(2)}$	(1,0,0)	$m^{(2)}$	$(0, \frac{\sqrt{3}}{2}, \frac{1}{2})$
$s^{(3)}$	(1,0,0)	$m^{(3)}$	$(0, \frac{\sqrt{3}}{2}, -\frac{1}{2})$
$s^{(4)}$	(0,1,0)	$m^{(4)}$	(0,0,1)
$s^{(5)}$	$(0, \frac{1}{2}, \frac{\sqrt{3}}{2})$	$m^{(5)}$	$(0, \frac{\sqrt{3}}{2}, \frac{1}{2})$
$s^{(6)}$	$(0, -\frac{1}{2}, \frac{\sqrt{3}}{2})$	$m^{(6)}$	$(0, \frac{\sqrt{3}}{2}, -\frac{1}{2})$

The plastic component of the deformation gradient associated with shearing on the slip systems follows as:

$$\dot{F}_{ik}^p (F_{kj}^p)^{-1} = \sum_{\beta=1}^N \dot{\gamma}^{(\beta)} s_i^{(\beta)} m_j^{(\beta)}, \quad (5.23)$$

where $\dot{\gamma}^{(\beta)}$ is the shear rate on slip system β . Plastic deformation due to shearing on each slip system is governed by the resolved shear stress $\tau^{(\beta)}$:

$$\tau^{(\beta)} = s_i^{*(\beta)} \sigma_{ij} m_j^{*(\beta)}. \quad (5.24)$$

The pressure dependence of the composite tows is incorporated into the yield strength of the model as a linear pressure dependent strengthening such that

$$g^{(\beta)} = \begin{cases} \tau_y + \mu p & p \geq 0 \\ \tau_y & p < 0 \end{cases}. \quad (5.25)$$

where p is a measure of the pressure transverse to the fiber direction and is hence defined in terms of the 2nd Piola-Kirchhoff stress as:

$$p = -\frac{1}{2}(S_{22} + S_{33}). \quad (5.26)$$

The pressure in the fiber direction S_{11} is not used because it is orthogonal to all the shear planes and is therefore not thought to contribute to any shear hardening.

An ideal shear formulation would incorporate a rate independent model for $\gamma^{(\beta)}$, but there are significant numerical difficulties associated with the rate independent limit in determining the active slip systems and the amount of slip on each of these systems. Therefore, a model similar to one proposed by Asaro [62] is followed, wherein the shear is specified by a rate dependent law as:

$$\dot{\gamma}^{(\beta)} = \dot{\gamma}_0 \text{sign}(\tau^{(\beta)}) \left(\frac{\tau^{(\beta)}}{g^{(\beta)}} \right)^n, \quad (5.27)$$

where $\dot{\gamma}_0$ is a reference strain rate, here set to be equal to the global applied strain rate, and n is a rate sensitivity exponent such that the rate independent limit is retrieved for $n \rightarrow \infty$. A rate sensitivity of $n = 5$ is used here, which approaches the rate independent limit [110]. More complexity can be added to this model by including more advanced rate dependence laws, latent hardening or cross slip hardening to particular slip systems, but these effects are ignored in the calculation presented in this chapter.

5.4 Numerical results

In the final part of the chapter, the results of the numerical models in relation to their experimental analogues are examined and discussed. It is found that the Crystal Plasticity model effectively reproduces the hardening behavior of the 3DNOOBED composite, while the Hill plasticity model significantly under predicts the response. The difference in hardening behavior predicted by the different models is discussed, along with the effect of incompatible failure modes, texture evolution and the pressure build-up in the tows that is introduced by the Crystal Plasticity model. The significance of the three-dimensionality of the 3DNOOBED composites is studied in simulations where y-direction tows were replaced by matrix pockets. The shortcomings of the numerical model are discussed and the changes that could be made to improve the predictive capabilities are examined.

5.4.1 Comparison to Hill plasticity

The Hill plasticity model over predicts the initial elastic stiffness and under predicts the large strain hardening behavior. Simulations on xz orientation samples give an initial shear modulus of $G = 1.71$ GPa and a yield limit of $\tau_y = 9.2$ MPa. This shear modulus is ≈ 6 times greater than that of the experiments, meaning it significantly overestimates the elastic response, but the yield strength of the simulation and the experiments are in reasonably good agreement as can be seen in Figure 5.11a. The simulation for the zx orientation samples gives a similar response with an initial shear modulus of $G = 1.74$ GPa and a yield limit of $\tau_y = 9.4$ MPa. The experimental modulus is overestimated by a factor of ≈ 5 but still gives a reasonably good agreement with the yield stress as can be seen in Figure 5.11d. This overestimation of the shear

modulus occurs because, unlike for the shear strength, the model does not attempt to account for any of the imperfections affecting the stiffness of the sample, such as the waviness of the tows, the large pre-existing cracks or any locally debonded areas between tows. Knockdown factors could be incorporated to reduce the tow stiffnesses and low strength cohesive interfaces could be included between the tows to reproduce the local debonding, but the large diversity and irregularity of the defects makes it difficult to capture their exact effect without modeling them explicitly.

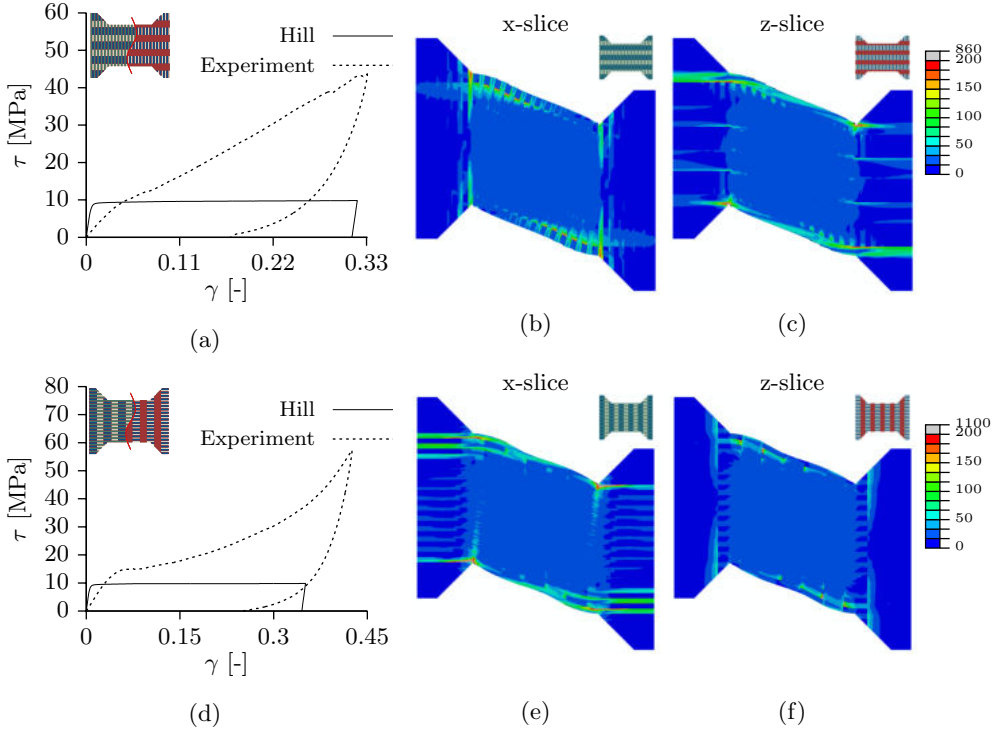


Figure 5.11: An overview of the shear experiments modeled with Hill plasticity based homogenization. Figure (a) and (d) show the stress-strain curves comparisons between the experiments and the simulations, Figures (b), (c), (e) and (f) show Von Mises stress contours. Stresses are in MPa.

Figures 5.11b, 5.11c, 5.11e and 5.11f show the Mises stress in the models with Hill plasticity at an applied strain of $\epsilon = 40\%$. Plots of the Mises stress are intended to illustrate where shear failure inhibition leads to the build-up of large stresses, not to be a direct comparison with the equivalent strain plotted in the DIC results in Figure 5.4. Despite the considerable anisotropy in the elastic properties, the post-yield state shows very little stress concentration arising anywhere in the gauge section of the samples. The only areas with considerably large stress build-up are the corners of the gauge sections, where the sample geometry naturally gives rise to a large tensile and compressive stresses and where the sharp corners further added to the stress concentrations.

Figures 5.13b and 5.13d show that there is also almost no hydrostatic stress build-up in the gauge section of the sample, even at large shears. The uniform shearing

behavior observed in these models is qualitatively different from the response observed experimentally.

The stress-strain curves in Figures 5.11a and 5.11d show that the Hill model produces effectively no strain hardening response after the onset of plasticity for either sample orientation tested. Furthermore, there is very little stiffening in the unloading response at higher applied strains as can be shown in Figures 5.9c and 5.9d. This occurs because the model fails to capture two major physical attributes of the 3DNOBED composites: the fiber rotation and the shear yield anisotropy. Although the tows physically rotate in the model according to the applied shear, the material coordinate transformation is dependent on the rotation of the deformation gradient $\mathbf{R} = \mathbf{F}u^{-1}$, which includes the elastic and plastic components of the deformation. The deformation gradient rotation does not necessarily follow the global tow rotation, particularly when large shears are applied, and the material coordinates are thereby frequently misaligned with the fiber direction. This misalignment leads to an improper prediction of the stiffness and an incorrect orientation of the yield surface. Additionally, the tows have an intrinsic anisotropy in their shear yield limits due to the orientation of the fibers, i.e. $\tau_{y12} \neq \tau_{y21}$ and $\tau_{y13} \neq \tau_{y31}$ [47]. This shear yield anisotropy occurs because the shear strength along the fiber axis (τ_{y12} and τ_{y13}) is governed by the strength of the matrix, but shear strength transverse to the fiber axis (τ_{y21} and τ_{y31}) involves a combination of shearing and bending of the fibers and a resolving of the shear into the orthogonally aligned matrix. Failing to capture this effect leads to both an overestimation of the shear strain in the tows and to an additional incorrect material coordinate rotation.

5.4.2 Comparison with Crystal Plasticity model

The Crystal Plasticity model has a similar initial stress-strain response to the Hill model, with shear stiffness and yield strengths of $G = 1.63$ GPa and $\tau_y = 9.1$ MPa for the xz orientation sample and $G = 1.61$ GPa and $\tau_y = 9.3$ MPa for the zx orientation sample. This means the Hill and Crystal Plasticity models similarly overpredict the experimental shear stiffness but give reasonable agreement with the yield strength, which is expected given that the stiffness and initial yield strengths are identical between them. The reasons for the shear stiffness discrepancy between the Crystal Plasticity model and the experiments are the same as those discussed for the Hill model.

At large strains, the Crystal Plasticity model has a pronounced hardening response, which is in stark contrast to the Hill plasticity results. This hardening occurs regardless of any pressure dependent strengthening, but some amount of pressure dependence is needed to more accurately reproduce the experimental hardening behavior. Figure 5.12a indicates that the model provides good agreement with the hardening behavior of the xz orientation sample, although it does not perfectly reproduce the rapid onset of hardening or the near constant hardening slope. This discrepancy is likely due to the complex crack and delamination behavior of the z-tows during deformation. Figure 5.12d shows that the model provides excellent agreement with the hardening behavior of the zx orientation sample, accurately reproducing the plateau in the stress-strain response and the large hardening that followed at higher strains. The slight underestimation of the magnitude of the stress likely occurs because the tow shear strengths are set to be equal regardless of fiber volume fraction or slip direction,

and correctly predicting the shear strength anisotropy will require more accurately modeling the effect of fiber content and transverse vs longitudinal slip on the tow shear strength.

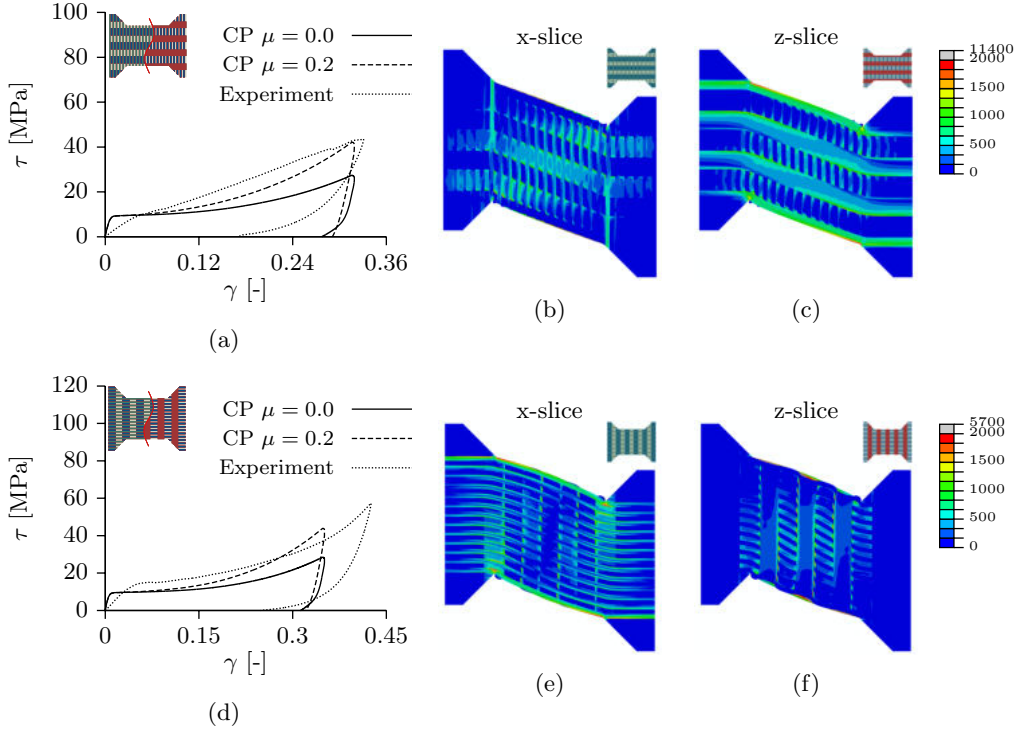


Figure 5.12: An overview of the shear experiments modeled with Crystal Plasticity based homogenization. Figure (a) and (d) show the stress-strain curves comparisons between the experiments and the simulations, Figures (b), (c), (e) and (f) show Von Mises stress contours. Stresses are in MPa.

The unloading stiffness trends of the Crystal Plasticity simulations shown in Figures 5.9c and 5.9d qualitatively match those of the experiments, predicting a plateau in the unloading stiffness at small strains and then a monotonic increase in the unloading stiffness at higher applied strains. The simulated unloading stiffnesses are consistently 0.7 – 1.0 GPa higher than the experimentally measured unloading stiffnesses. Analog to the mismatch in the initial elastic stiffness, the mismatch in unloading stiffness occurs because there is no knockdown applied to the constituent material stiffnesses. The monotonic stiffening effect is primarily due to the reorientation of the fibers, particularly of those initially aligned with the dogbone axis that rotate toward the shearing axis. The rate at which the stiffening occurs can provide insight into the failure in the composite.

Figure 5.9c indicates that the xz orientation simulation stiffens at a slower rate than the experiments, indicating that there is an additional shear hardening in these experiments compared to the simulations. This could be because the xz orientation samples are weaker due to the initial debonding in the z-tows as could be observed in Figure 5.5, and the higher hardening rate could be due to frictional lock-up along the

z-direction tows. In Figure Figure 5.9d, the zx orientation model stiffens at a faster rate than the experiments, indicating there is an additional shear softening in these experiments compared to the model. This could be due to factors like micro-structural damage, which is observed to a greater extent in the zx composite, shown in Figure 5.7. The unloading stiffness of the xz orientation model increases at a slightly slower rate than that of the zx orientation model, but this is likely due to the initial higher fiber volume fraction along the axis of the zx orientation sample.

The Mises stress plots of the Crystal Plasticity simulations shown in Figure 5.12b, 5.12c, 5.12e, and 5.12f illustrate the considerable suppression of shear strain in the tows. Many regions in the model undergo large shear strains, particularly in tows that lie parallel to the shearing axis, but the large stress concentrations that arise at tow interfaces indicate there are incompatible shearing modes between them that inhibit failure. It is this failure inhibition that brings about the hardening response in the Crystal Plasticity model. We discuss this point in more detail in Section 5.4.5. The location of many of the stress concentrations are similar to regions that experience cracking in experiments, suggesting that the implementation of a cohesive interface between tows could qualitatively reproduce the experimental cracking behavior. The inability of the model to form cracks is likely one of the most significant factors influencing the discrepancy with the experiments.

5.4.3 The role of pressure dependence

The hydrostatic pressure in the 3DNOOBED composite models has a significant impact on their mechanical behavior. Using Crystal Plasticity, the pressure in the central area of the gauge section, away from the stress concentrations near the corners, reached as high as $p = 300$ MPa in the xz orientation model and $p = 400$ MPa in the zx orientation model. The pressures in certain areas of the sample, particularly the matrix pockets and the tows perpendicular to the shearing direction, is consistently above $p = 100$ MPa as is shown in Figure 5.13c and 5.13d. With a pressure sensitivity of $\mu = 0.2$, these pressures correspond to an increases of tens of MPa in the yield strength of both the tows and the matrix, which is considerably large given that the initial yield strength is $\tau_y = 10$ MPa. Although the pressure is not uniformly distributed across the gauge section or the individual tows, its impact on the global mechanical behavior is pronounced. The stress-strain response of the xz orientation model with and without a pressure dependent shear strength is shown in Figure 5.12a. The strengthening shows an increase from 36.6 MPa to 58.5 MPa at $\epsilon = 0.36$. A similar response is observed in the zx orientation composite. The stress-strain curve shown in Figure 5.12d show an increase from 32.3 MPa to 52.1 MPa at $\epsilon = 0.36$. In contrast, the hydrostatic pressure in models with Hill plasticity rarely reached above $p = 10 - 15$ MPa. Even with a considerably large pressure dependent strengthening coefficient, this pressure would have little to no impact on the global mechanical behavior

5.4.4 Without y-direction Tows

To investigate the effect of the through direction tows on the mechanical behavior of the 3DNOOBED composites, a model is constructed with the y-tows replaced by pure matrix. Figure 5.14 shows that in both the xz and zx orientation models, there is a considerable drop in the hardening response when the y-tows are removed. For the xz orientation simulation, the resulting stress of the model with no y-tows is 19.1 MPa at

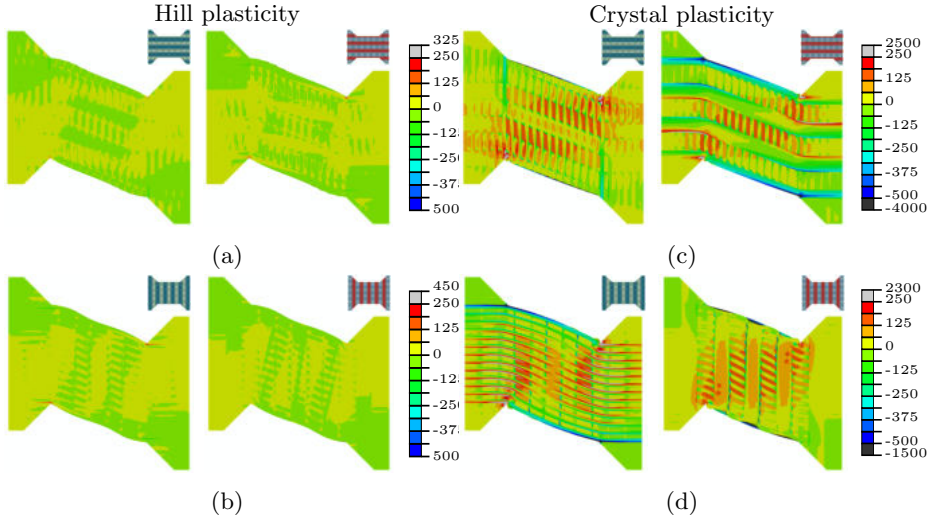


Figure 5.13: Contour plots of the hydrostatic stress in the xz samples. Figures (a) and (c) show the sample modelled with Hill plasticity and Figures (b) and (d) show the samples modelled with Crystal Plasticity. Stresses are in MPa.

$\epsilon = 0.36$, compared to 58.5 MPa at $\epsilon = 0.36$ for the full 3D model. Similarly, for the xz orientation simulation, the resulting stress of the model with no y-tows is 18.9 MPa at $\epsilon = 0.36$, compared to 52.1 MPa for the full 3D model. There is also a small drop in the initial shear stiffness of $G = 1.18$ GPa for the xz orientation and $G = 1.11$ GPa for the zx orientation, but this effect is small in comparison. Despite the large drop in the hardening response, the yield stresses in the models without y-tows are nearly identical to those of the full 3D composite.

By using the same shear strength for the tows and the matrix in the Crystal Plasticity model, it is possible to see the effect of the 3D architecture. The x- and z-tows provide some resistance to the shear, as is demonstrated by the small hardening response, but removing the through direction y-tows also removes the incompatible failure planes, allowing shear to occur more freely. The x- and z-tows still have some incompatibility in their failure mechanisms. Correspondingly, Figures 5.14c and 5.14e show that there are regions in the model with considerable stress concentrations in the tows, primarily in tows that are perpendicular to the shearing axis, but the overall stresses are lower than those in the full 3D composite. The initial yield strength of the 2D composite does not change because shear failure in the matrix and tows is activated at the same stress. These simulations are intended to mimic the in-plane shear response of a laminated composite, and the hardening behavior was found to closely resemble that of 0-90 laminated CFRP composites [47], albeit with a lower magnitude of strength.

5.4.5 Interpretation and discussion of Crystal Plasticity results

The Crystal Plasticity model qualitatively reproduces the experimental behavior of the 3DNOBED CFRP composites. This is possible because the model captures some of the key physics governing the deformation behavior, namely the fiber rotation, shear

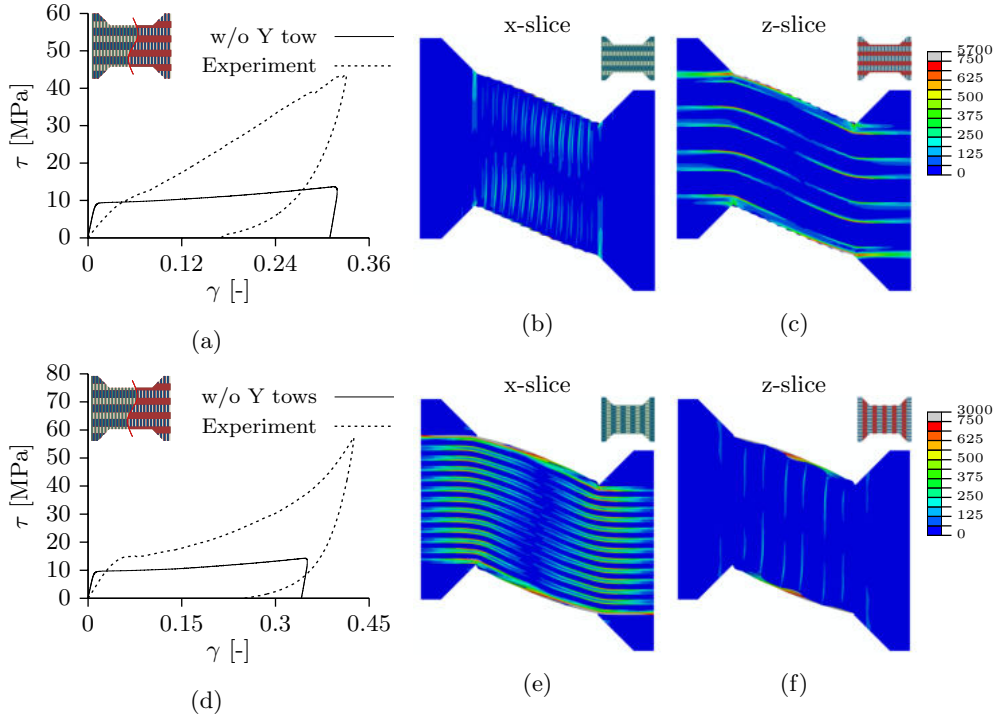


Figure 5.14: Crystal Plasticity Results without y-Tows. Stress-strain plots of the uniaxial loading results from Crystal Plasticity simulations without y-tows for (a) xz and (d) zx 3DNOOBED composites compared to representative experiments. The stress plots show Mises stress concentrations for x- and z-sections of the (b)/(c) xz and (e)/(f) zx orientation simulations at $\epsilon = 40\%$ applied strain to illustrate the location of stress concentrations in the tows. Stresses are in MPa.

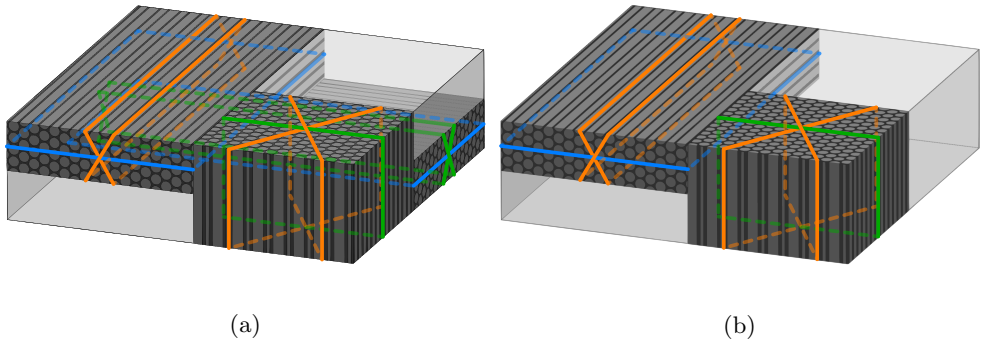


Figure 5.15: Compatible and incompatible failure mechanisms. (a) A sketch of the failure planes in a 3DNOOBED architecture shows that there are no compatible failure mechanisms between all three tows. (b) A sketch of the failure planes in a 2D composite illustrate the compatible failure mechanisms. Planes with the same colour indicate compatible failure mechanisms.

strength directionality and pressure dependence of the tows and matrix. In the process, it elucidates the role of the 3D architecture on the mechanical performance and reveals two unique effects that lead to the enhanced shear performance: incompatible shear failure and texture evolution.

One of the dominant plasticity mechanisms in a unidirectional composite is inter-fiber shear failure [88]. The confinement of this failure in laminated and 3D fiber composites can greatly improve the post-yield behavior. If a local shear event is activated and there are compatible shearing mechanisms in coinciding regions, the failure event will be able to propagate at a sufficient applied load. If there are differently oriented shear modes in coinciding regions, the propagation of a failure event would require a higher applied load because the stress must be resolved in a different direction to activate it. If there are completely orthogonal failure modes or if there are multiple intersecting failure planes with no possibility of resolving the shear along each of them, the mechanisms would be incompatible and failure would not be able to propagate. In the 3DNOBED composite architecture drawn in Figure 5.15a, the 3D assembly of the tows makes it so that there are no failure mechanisms that are compatible with every tow. Therefore, even though failure may be able to occur locally in a single tow or between two tows, it will not be able to propagate globally through the sample, effectively 'locking' the failure and giving rise to a hardening response irrespective of the shear necessary to activate individual slip planes. In contrast, for a laminated or 2D composite, similar to the one drawn in Figure 5.15b, there will always be some sets of compatible failure mechanisms normally aligned with the lamination plane. Having compatible failure mechanisms leads to a significantly less pronounced hardening behavior.

Failure in the tows with Crystal Plasticity is directional and restricted to occur via longitudinal or transverse shear. Any axial stretching or shearing that is not aligned with the slip directions will lead to a build-up of stress in the tows. The activation of shear failure modes brings about a corresponding directional shape change. Due to the 3D orientation of the composite, most of the shape changes in a tow are incompatible with shape changes in the coincident tows, meaning that failure leads to a texture evolution in the samples. The development of texture in the sample is accommodated through a build-up of hydrostatic pressures and large local stresses in the inter-penetrating tows, and these pressures have a pronounced effect on the mechanical properties due to the pressure sensitivity of the constituent materials. The texture evolution thereby has a major effect on the final mechanical properties, as is indicated by the stress-strain curves of the samples with and without pressure dependence displayed in Figures 5.12a and 5.12d. The textures observed in the Crystal Plasticity models qualitatively align with the textures observed experimentally.

5.5 Implications for Homogenized Models

It is found in this chapter that capturing the micro-structural evolution of a composite material is hugely important to predicting its resulting properties. Although continuum plasticity methods can reasonably replicate the physical rotation of a tow during deformation, they are unable to capture the micro-structural response, i.e. the material response, and therefore do not correctly predict the resulting behavior. The Crystal Plasticity method provides a convenient means of modeling the micro-structural response of the tows while simultaneously reproducing the macro-scale response. The

model presented here is able to reproduce the 3DNOOBED composite behavior because all of the tows are explicitly modeled, and therefore the tow level micro-structural response does not need to be accounted for. However, any homogenization scheme for a 3D laminated composite would need to account for the micro-structural evolution both at the tow level and at the fiber level, thereby requiring something of a multiscale Crystal Plasticity method.

5.6 Summary

The performance of 3DNOOBED CFRP composites has been examined, finding that they undergo extensive hardening in shear and have minimal damage propagation prior to failure. The composites also show a monotonic increase in their unloading stiffness prior to ultimate failure via tensile rupture. Two tow-level numerical models were used to study the 3DNOOBED composite behavior, one based on a Hill yield criterion and one using Crystal Plasticity modeling. It was found that the Hill model does not reproduce any of the hardening observed experimentally because it is unable to capture the micro-structural response of the tows, namely the fiber rotation and shear anisotropy. The Crystal Plasticity model captured the experimentally observed hardening behavior; elucidating the effect of incompatible shear modes; texture evolution and pressure sensitivity on the global mechanical response. The organization of the tows in the 3DNOOBED composite creates a truly 3D effect that enables both enhanced post-yield hardening and considerable energy absorption prior to failure.

In the next Chapter a set of 3DNOOBED compression experiments are modeled. The predictive capability with respect to the stress-strain response of the 3DNOOBED composite is investigated. Furthermore, the capability of the Crystal Plasticity based tow-level homogenization to simulate reflective kinking is investigated as well.

Chapter 6

On the enhanced ductility of 3DNOOBED composites under compressive loadings

In this chapter, the Hill plasticity based approach presented in Chapter 3 and the Crystal Plasticity based tow-level homogenization presented in Chapter 4 are used to the mechanical behavior of 3DNOOBED composites that are loaded under compression. The predictive capabilities with respect to the stress-strain response observed in the experiments is investigated as well as the the ability to model the reflective kink-bands that appear during experimental testing.

6.1 Fabrication and Microstructure

The 3D Non-interlacing Orthogonally Orienting & Binding (3DNOOBED) composites are composites that have non-woven tows placed in three orthogonal directions. A schematic of the placement of tows in the 3DNOOBED composites can be seen in Figure 6.1. The 3DNOOBED composites were fabricated using T700S carbon fiber

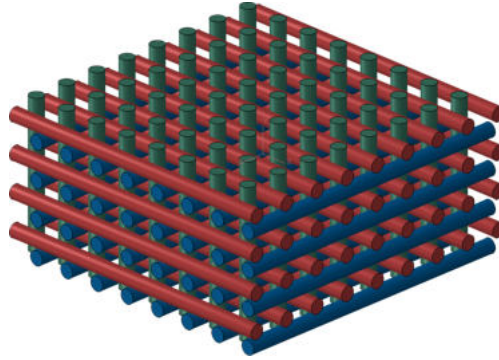


Figure 6.1: Schematic of the placement of tows in the 3DNOOBED composites studied in this chapter.

tow bundles (Toray composite Materials America Inc., USA) and NM FW 3070 epoxy (Nils Malmgren AB, Sweden) as the binder. Carbon fiber tows were woven into a 3D fabric block that was subsequently infused with the epoxy, producing a non-crimp fabric with tows oriented orthogonally in the x, y, and z direction. The tows were initially connected via loops at the edges of the woven sample [81].

Two samples with different numbers of fibers in the x-, y, and z-direction tows were used. The two different samples are referred to as sample A and sample B. In sample A, the x- and y-tows consist are 12k tows and have an average volume fraction of 62.2%. The z-tows are 24k tows with an average volume fraction of 40.1%. In sample B, the x- and y-tows were 12k tows with an average volume fraction of 67.7%. The z-tows in this sample were 48k tows with an average volume fraction of 71.1%. The x- and y- tows had rectangular cross sections while the z-tows had square cross sections.

The dimensions of the tows in each of the samples are shown in Table 6.1. The degree of internal and external waviness of the tows in each of the samples is quantified in Appendix B. The 3DNOOBED composites were provided in the form of large blocks of $\approx 200 \times 125 \times 50$ mm by Biteam (Biteam AB). The samples were cut roughly to size using a diamond cutting disk, and were finished in a milling machine using a carbide cutting tool to a final dimension of $10 \times 10 \times 43$ mm. The loops on the outer edges of the sample were cut off during this process. Two orientations of the composite were made, one with the x-tows aligned with the long axis, and one with the z-tows aligned with the long axis. The experiments on these two orientations will be referred to as x-tow compression experiments and z-tow compression experiments. The two samples with two orientations each resulted in four different types of specimens in total.

Table 6.1: Dimensions of the different tows in sample A and B in mm.

Sample A			Sample B		
x Width	x Height	z Width	x Width	x Height	z Width
1.74 ± 0.1	0.44 ± 0.06	1.54 ± 0.1	1.56 ± 0.16	0.45 ± 0.1	1.67 ± 0.05

6.2 Experimental methods

Testing was done in a screw driven Instron 5500R testing device (Instron Corp., USA). Compression was performed along the long axis of the specimen in a clamped compression setup identical to the one used by Das et.al. [81]. The samples were placed into steel slip fit end caps that were ≈ 13 mm thick and compressed between two pin-guided steel platens. The slip fit end caps were used to prevent premature global buckling of the specimen. Most of the resulting damage that occurred during testing was confined to the exposed gauge section of the sample. An overview of the experimental setup can be seen in Figure 6.2.

The compression experiments were performed at a rate of 0.2 mm/min, corresponding to a strain rate of $\approx 7.5 \cdot 10^{-5} \text{ s}^{-1}$. A laser extensometer was used to measure the displacement of the platens with laser strain gauges placed ≈ 15 mm apart. The strain of the sample was calculated by normalizing the applied displacement by the total 43 mm length of the specimen. The load on the sample was measured using a 100 kN load cell, and the stress was calculated by normalizing the load by the 100 mm^2 cross sectional area.

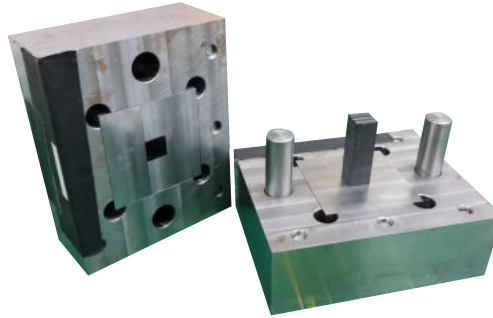


Figure 6.2: An overview of the clamped compression setup.

Two types of imaging were performed to quantify the damage that took place during testing. X-Ray computed tomography (XCT) images were taken before and after testing in an X-Tek XTH 225ST system (Nikon Metrology UK Ltd.), which revealed the full internal micro-structure of the sample. An Olympus BX51M optical microscope was used to obtain high-resolution images of different layers of the post-test samples. Before capturing the microscopy images, samples were cut in half using a diamond cutting blade, then polished using diamond grit polishing sheets and finally with an alumina particle slurry to an RMS roughness of $< 1 \mu\text{m}$. Large area images were obtained by capturing multiple images and stitching them together in post-processing.

6.2.1 Experimental results

Figure 6.3 shows the stress-strain response of the x- and z-tow compression of the sample A and B 3DNOOBED composites. A minimum of four different samples per configuration were tested to varying degrees of applied strain to observe the evolution of damage and to garner some statistical repeatability for the behavior. The different samples in each loading case showed some degree of scatter in their results, but the overall trends are similar. In the x-tow compression case for sample A, samples underwent a linear-elastic deformation with a stiffness of $E = 27.3 \pm 0.5 \text{ GPa}$ before reaching peak stresses between $\sigma_{\text{peak}} = 260$ to 300 MPa . After the initiation of failure, there was some intermittent failure before the stress dropped to a lower plateau stress around $\sigma_{\text{plateau}} = 225 \text{ MPa}$. In the z-tow compression case, samples underwent a linear-elastic loading with a stiffness of $E = 14.5 \pm 0.9 \text{ GPa}$ before reaching a peak stress between $\sigma_{\text{peak}} = 135$ and 155 MPa .

After the initiation of failure some loss in load carrying capacity was observed, after which samples experienced a moderate hardening behavior, reaching stresses of $\sigma = 270 \text{ MPa}$ at strains of $\epsilon = 0.05$. Figure 6.3 shows the stress strain response of the x- and z-tow compression experiments on the sample B. The results from each of these tests was highly repeatable, likely due to the hardening behavior in both loading directions. In the x-tow compression case, samples underwent a linear elastic loading with a stiffness of $E = 31.8 \pm 1.4 \text{ GPa}$ before reaching peak stresses between $\sigma_{\text{peak}} = 210$ and 260 MPa . The large range of peak stresses is likely due to a large variance in the initial imperfection landscape of the samples. After the initial failure event, there was a strong hardening behavior, with samples reaching stresses of $\sigma = 350 \text{ MPa}$ at

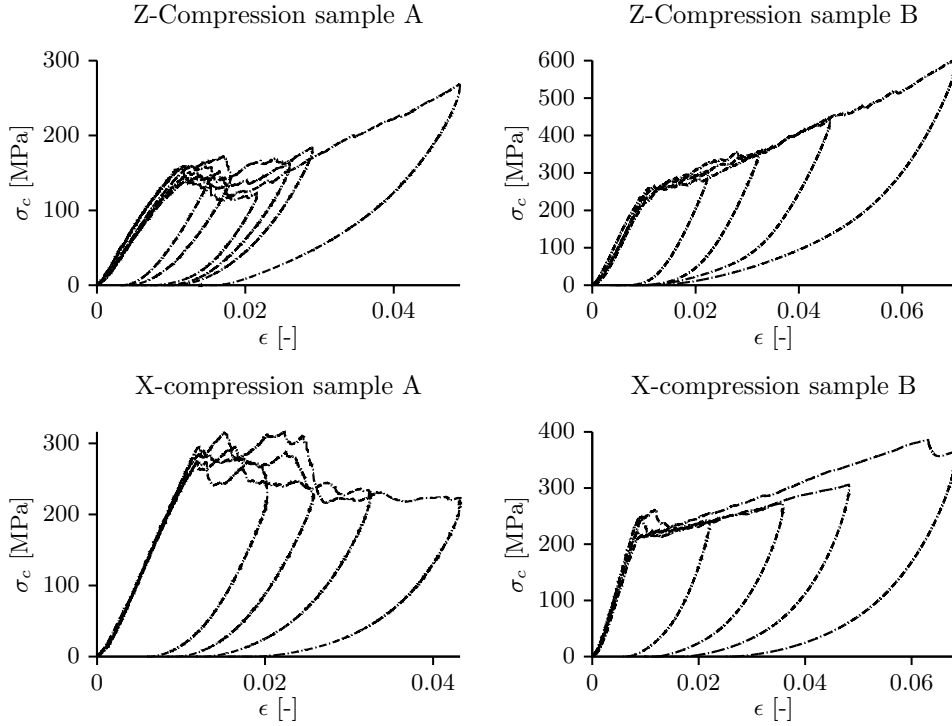


Figure 6.3: Stress-strain results from 3DNOOBED compression testing. The data shows the compression response of tests on four individual samples to varying degrees of stress.

strains of $\epsilon = 0.05$. The drop in stress at $\epsilon = 0.063$ corresponds with rupture of one of the transverse z-tows. In the z-tow compression case, samples underwent a linear elastic loading with a stiffness of $E = 28.0 \pm 0.6$ GPa until the initiation of failure at $\sigma_y = 240$ to 258 MPa. Here, samples had a very narrow band of failure strengths, indicating that the variation of imperfections was very similar. The samples showed a pronounced hardening after failure, reaching stresses of $\sigma = 475$ MPa at strains of $\epsilon = 0.05$.

Final failure for all samples in both loading cases occurred at strains of $\epsilon_y \approx 0.011$. In both loading cases, there was some hysteresis during unloading, indicating that some viscoelastic deformation contributed to the unloading from the polymer. During testing, sonic emissions could be detected corresponding to the drops in stress. The magnitude of the emission roughly correlated with the magnitude of the strength drop, although emissions could still be detected in samples that were experiencing hardening despite of not showing any considerable drop in stress.

The XCT images revealed the evolution of damage in the samples after testing to varying levels of strain as shown in Figure 6.4. Despite the differences in peak stresses between samples A and B, the failure mechanisms were relatively similar between each sample for a given compression direction. For the x-tow compression samples, damage accumulated largely in the gauge section of the sample in the form of kink

bands oriented at 15° to 30° relative to the horizontal axis, as shown in Figure 6.4a. These kink bands all formed along the xz plane, and there was little to no relative shift or rotation of the band along the y-axis. Once the first kinks formed, some were able to propagate whereas other kinks were trapped and reflected. The kink bands that interacted with matrix pockets, were largely able to transmit through the pocket, causing a kink to initiate in the adjacent tow. When kinks interacted with y-direction tows, their motion was largely impeded at small strains, leading to a reflection of the kink inside the tow. At large strains, the kink bands were able to propagate through the y-tows, although this propagation took place at a different orientation angle than the kink itself, often at 60° to 75° relative to the horizontal axis. This kink propagation through the y-tows led to internal delamination, some of which was observed to propagate through the tow into the next layer. None of the kinking damage propagated to the z-tows, and no damage was observed in the z-tows until sufficiently large compressive stresses were applied such that indirect tensile failure occurred.

For the z-tow compression samples, damage was almost entirely confined to the z-tows in the form of internal and reflected kinking as can be seen in Figure 6.4b. Most of the damage initiated at the ends of the sample, although at higher strains, damage was observed to build up in the gauge section. The kinks were independent of the direction, and while many formed in the xz or yz plane, some also showed a mixed character between the two directions, although most were oriented at an angle of 15° to 30° relative to the horizontal axis. Many kink bands initiated at cracks or voids along the outer edges of the z-tows, after which they remained confined to the z-tow. Essentially, no damage was observed in the x- or y-tows until the onset of catastrophic failure via indirect tensile rupture, at which point the majority of the gauge section of the sample was destroyed. Microscope images provide a more detailed

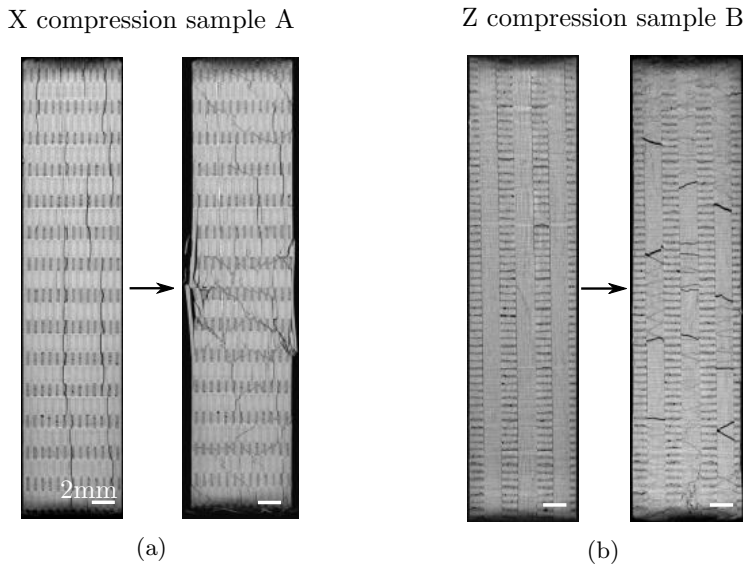


Figure 6.4: An overview an undamaged and a damaged x-direction compression sample in Figure 6.4a. Figure 6.4b shows an overview of an undamaged and a damaged z-direction compression sample.

look at the kink band propagation behavior. Figure 6.6 shows the transmission of a kink band through a matrix pocket as well as the mixed transmission and reflection of a kink interacting with the y-tows. It can be seen that a considerable amount of damage and delamination occurs where the kink passes through the transverse tow, while there is no visible damage at the location where the kink passes through the matrix pocket. It is also revealed that many of the kink bands initiate at the regions where the fibers in the the x-tows show some significant curvature. Figure 6.6 shows the complete internal reflection of kink bands that have initiated in z-tows, both at the matrix pockets and other tows. Many kinks either initiate or intersect with the interface between the matrix pockets the transverse tows, which often coincides with local cracks or delaminated areas.

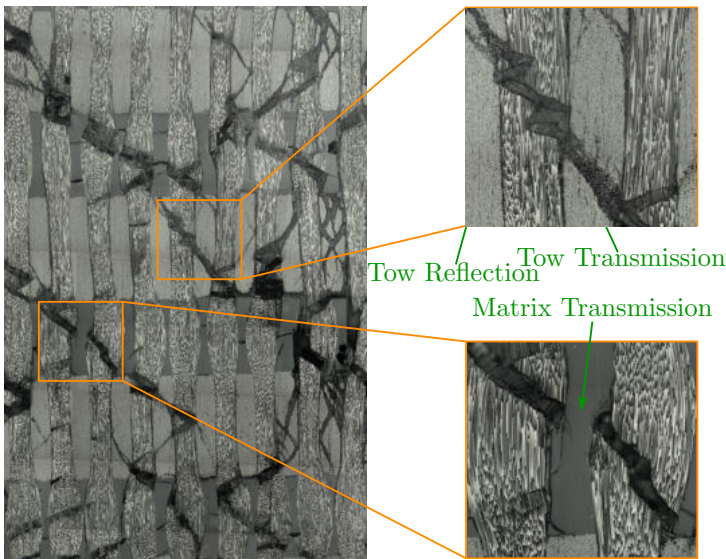


Figure 6.5: Micrographs of a x-tow compression test showing kinks that are transmitted through tows.

6.3 Computational modeling

Both the x- and z-tow compression samples are each modeled with their own model. These models are introduced first. The constitutive modeling is discussed afterwards.

6.3.1 Z-tow compression model

In the z-tow compression a total of 9 z-tows are modeled in a 3x3 square arrangement. The z-tows are indicated in green in Figure 6.7a. The x-direction tows are indicated in red and the y-direction tows are colored blue. The matrix pockets in between the tows are colored beige. Four x-direction tows are modeled in the y-direction: two full tows and two halves at either end of the model. Similar to the y-direction, three y-direction tows are modeled in the x-direction making the model for sample A 9.96 mm wide and the model for sample B 9.71 mm wide. In total 11 x- and z-direction tows are stacked

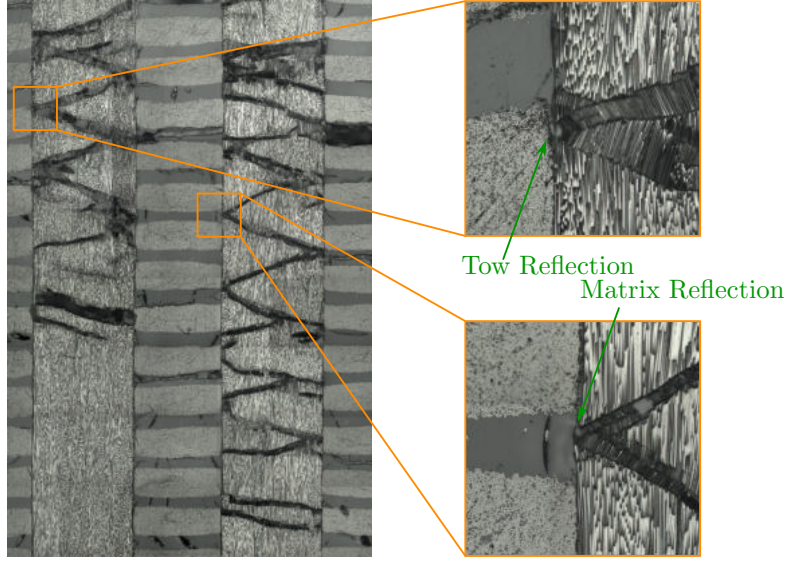


Figure 6.6: Micrographs of a z-tow compression test showing kinks that are reflected within tows.

on top of each other to exclude boundary effects. Simulations indeed indicated that the stress-strain response converges from this height on. The boundary conditions of the model can be seen in Figure 6.7b. The top surface of the model is fixed in the x- and z-direction and is subjected to a constant velocity prescribed in the y-direction. The nodes on the bottom surface are fixed in all directions. Imperfections are introduced in the z-tows to trigger buckling. Within these imperfection regions, indicated in grey in Figure 6.7b, the local orientation of the material are rotated at an angle $\phi = 2^\circ$ around the y-axis.

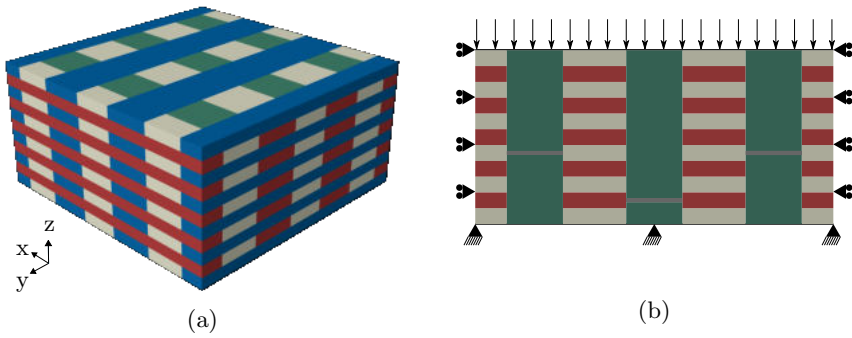


Figure 6.7: An overview of the z-tow compression model in Figure 6.7a and an overview of the boundary conditions used in the model in Figure 6.7b

6.3.2 X compression model

The x-tow compression model is constructed in a similar fashion as the z-compression model. A total of 3 x-direction tows are modeled across the z-direction and 8 tows are modeled in the compression direction. As there are no tows that are susceptible to kinking in the symmetry planes, only a quarter of the block was modeled using symmetry boundary conditions on the yellow and green planes indicated in Figure 6.8b. Other boundary conditions are indicated in Figure 6.8c. The displacements at the bottom of the model are fixed and the nodes at the top of the model are fixed in the y and z direction while being prescribed a velocity in the x direction. Imperfections are placed within the grey regions in the x-tows by rotating the material with an angle $\phi = 2^\circ$ around the z-axis.

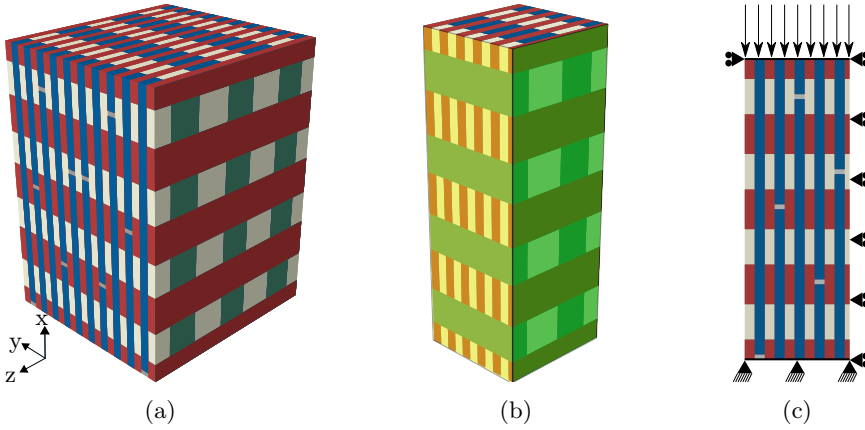


Figure 6.8: An overview of the x-compression sample in Figure 6.8a, an overview of the quarter model and the used symmetry planes in Figure 6.8b and the boundary conditions applied to the quarter model in Figure 6.8c.

The models are made using ABAQUS[®] explicit. Mass scaling is applied to reduce the computational time, while keeping the kinetic energy below 5% of the internal energy. Large strain kinematics are assumed and the models are meshed using 8 hexagonal elements with reduced integration across the thickness of the tows.

6.3.3 Constitutive modeling

Two constitutive models are considered to model the mechanical behavior of the tows: a Hill plasticity approach and a Crystal Plasticity approach. Both approaches are discussed after the elastic properties of the tows, which are the same for both approaches.

Elastic properties

The elastic properties of the tows are determined using the elastic properties of the fibers and matrix. Both the fibers and the matrix are assumed to be isotropic. The fibers are assumed to have an elastic modulus of $E_f = 231$ GPa and a Poisson's ratio of $\nu_f = 0.2$. The matrix has an elastic modulus of $E_m = 2700$ MPa and a Poisson's ratio of $\nu_m = 0.3$. The properties of the fibers and the matrix are summarized in Table 6.2

Table 6.2: Constitutive properties of the fibers and matrix

T700S Carbon fiber			NM FW 3070 Epoxy				
E_f	ν_f	σ_f	E_m	ν_m	σ_m	τ_y	μ
230 GPa	0.28	4.9 GPa	2.70 GPa	0.3	17.3 MPa	20 MPa	0.2

A constant volume fraction V_f is assumed in a tow, and the elastic stiffness in the fiber direction E_1 is calculated using the Voigt average of the fiber modulus E_f and the matrix modulus E_m :

$$E_1 = E_f V_f + E_m (1 - V_f) \quad (6.1)$$

The transverse moduli E_2 and E_3 are calculated using a Halpin-Tsai model [108]:

$$E_2 = E_3 = E_m \frac{1 + \eta \xi V_f}{1 - \eta V_f}, \quad (6.2)$$

where the parameters η and ξ are calculated using:

$$\eta = \frac{\frac{E_f}{E_m} - 1}{\frac{E_f}{E_m} + \xi} \quad (6.3)$$

and

$$\xi = 2 + 40V_f^{10}. \quad (6.4)$$

The shear moduli G_{12} and G_{13} are calculated in a similar way as the transverse elastic moduli:

$$G_{12} = G_{13} = G_m \frac{1 + \eta \xi V_f}{1 - \eta V_f}, \quad (6.5)$$

where the parameters η and ξ are now calculated using:

$$\eta = \frac{\frac{G_f}{G_m} - 1}{\frac{G_f}{G_m} + \xi} \quad (6.6)$$

and

$$\xi = 1 + 40V_f^{10}. \quad (6.7)$$

The Poisson's ratio's that involve the fiber direction are calculated using:

$$\nu_{12} = \nu_f V_f + \nu_m (1 - V_f) \quad (6.8)$$

$$\nu_{21} = \nu_{12} \frac{E_2}{E_1} \quad (6.9)$$

The transverse Poisson's ratios are determined using a Clyne model [109]:

$$\nu_{23} = 1 - \nu_{21} - \frac{E_2}{3K_t}, \quad (6.10)$$

where K_t is the bulk modulus of the tow. If K_m is the matrix bulk modulus and the fiber bulk modulus K_f is calculated using:

$$K_f = \frac{E_f}{3(1 - 2\nu_f)}, \quad (6.11)$$

the bulk modulus of the tow can be calculated using a Reuss average:

$$K_t = \left(\frac{V_f}{K_f} + \frac{1 - V_f}{K_m} \right)^{-1} \quad (6.12)$$

The Hill plasticity approach

The Hill plasticity approach used for the tows in the 3DNOOBED composites is the same as the approach used for the tows in the 2D plain weave models presented in Chapter 3 and the 3DNOOBED shear simulations presented in the previous chapter. Within Hill plasticity, an anisotropic yield potential is defined as:

$$f(\boldsymbol{\sigma}) = (F(\sigma_{22} - \sigma_{33})^2 + G(\sigma_{33} - \sigma_{11})^2 + H(\sigma_{11} - \sigma_{22})^2 + 2L\sigma_{23}^2 + 2M\sigma_{31}^2 + 2N\sigma_{12}^2)^{\frac{1}{2}}. \quad (6.13)$$

If the yield stress values $\bar{\sigma}_{ij}$ are the yield stress values of the material under a loading state where σ_{ij} is the only non-zero stress, the ratios F, G, H, L, M and N can be determined using:

$$F = \frac{\sigma^0}{2} \left(\frac{1}{\bar{\sigma}_2^2} + \frac{1}{\bar{\sigma}_2^2} - \frac{1}{\bar{\sigma}_1^2} \right) \quad (6.14)$$

$$G = \frac{\sigma^0}{2} \left(\frac{1}{\bar{\sigma}_2^2} + \frac{1}{\bar{\sigma}_1^2} - \frac{1}{\bar{\sigma}_2^2} \right) \quad (6.15)$$

$$H = \frac{\sigma^0}{2} \left(\frac{1}{\bar{\sigma}_1^2} + \frac{1}{\bar{\sigma}_2^2} - \frac{1}{\bar{\sigma}_2^2} \right) \quad (6.16)$$

$$L = \frac{3}{2} \left(\frac{\tau^0}{\bar{\sigma}_{23}} \right)^2 \quad (6.17)$$

$$M = \frac{3}{2} \left(\frac{\tau^0}{\bar{\sigma}_{13}} \right)^2 \quad (6.18)$$

$$N = \frac{3}{2} \left(\frac{\tau^0}{\bar{\sigma}_{12}} \right)^2 \quad (6.19)$$

where σ^0 is a reference yield stress and $\tau_0 = \sigma^0/\sqrt{3}$ is the corresponding reference shear yield stress. The axial strength σ_1 and the transverse strength σ_2 of the tows were calculated using the Voigt and Reuss rule of mixtures respectively, and the shear strengths were all set to be equal to the shear strength of the matrix τ_y .

$$\bar{\sigma}_1 = \sigma_f V_f + \sigma_m (1 - V_f), \quad (6.20)$$

$$\bar{\sigma}_2 = \left(\frac{V_f}{\sigma_f} + \frac{1 - V_f}{\sigma_m} \right)^{-1}, \quad (6.21)$$

$$\bar{\sigma}_{12} = \bar{\sigma}_{13} = \bar{\sigma}_{23} = \sqrt{3}\tau_y. \quad (6.22)$$

The plastic strain evolves according to the flow rule:

$$d\epsilon^{\text{pl}} = d\lambda \frac{\partial f}{\partial \boldsymbol{\sigma}} \quad (6.23)$$

Crystal plasticity

Originally intended for crystallographic materials, Crystal Plasticity uses slip planes and slip directions to describe the internal micro-structure of materials. In the context of fiber reinforced materials, the Crystal Plasticity framework can be used to describe UD materials or tows as they can be considered to be 2D cylindrical close packings. In Crystal Plasticity, the deformation gradient F_{ij} is considered to be a multiplicative decomposition of the elastic deformation gradient F_{ij}^e and the plastic deformation gradient F_{ij}^p :

$$F_{ij} = F_{ik}^e F_{kj}^p \quad (6.24)$$

The slip systems β are specified by two vectors: the slip direction $s_i^{(\beta)}$ and the slip plane in the undeformed configuration $m_i^{(\beta)}$. Multiple slip systems are needed to describe the deformation of a UD ply or a tow in 3D analysis. It is assumed that the fibers are arranged in a close packing and the slip systems are constructed accordingly. A schematic of the slip systems in a tow can be seen in Figure 6.9 and their respective slip directions and slip plane normals are listed in Table 6.3.

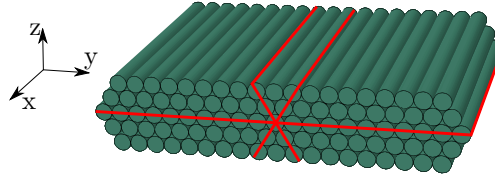


Figure 6.9: A close packing of fibers and the used slip systems indicated in red.

Table 6.3: Slip directions and slip plane normals for a UD ply or tow.

slip direction		slip plane normal	
$s^{(1)}$	$(1,0,0)$	$m^{(1)}$	$(0,0,1)$
$s^{(2)}$	$(1,0,0)$	$m^{(2)}$	$(0, \frac{\sqrt{3}}{2}, \frac{1}{2})$
$s^{(3)}$	$(1,0,0)$	$m^{(3)}$	$(0, \frac{\sqrt{3}}{2}, -\frac{1}{2})$
$s^{(4)}$	$(0,1,0)$	$m^{(4)}$	$(0,0,1)$
$s^{(5)}$	$(0, \frac{1}{2}, \frac{\sqrt{3}}{2})$	$m^{(5)}$	$(0, \frac{\sqrt{3}}{2}, \frac{1}{2})$
$s^{(6)}$	$(0, -\frac{1}{2}, \frac{\sqrt{3}}{2})$	$m^{(6)}$	$(0, \frac{\sqrt{3}}{2}, -\frac{1}{2})$

During deformation, the rotation of the slip direction and the slip plane normal is dictated by the elastic deformation gradient:

$$s_i^{*(\beta)} = F_{ij}^e s_j^{(\beta)}, \quad m_i^{*(\beta)} = m_j^{(\beta)} (F_{ji}^e)^{-1}. \quad (6.25)$$

The plastic component of the deformation can be calculated using:

$$\dot{F}_{ik}^p (F_{kj}^p)^{-1} = \sum_{\beta=1}^N \dot{\gamma}^{(\beta)} s_i^{(\beta)} m_j^{(\beta)}, \quad (6.26)$$

where $\dot{\gamma}^{(\beta)}$ is the shear rate on slip system β . Per slip system, the plastic deformation is determined by the resolved shear stress

$$\tau^{(\beta)} = s_i^{*(\beta)} \sigma_{ij} m_j^{*(\beta)}. \quad (6.27)$$

Most polymers have a yield stress that is dependent on the amount of hydrostatic pressure present. An increase in yield stress with increasing hydrostatic pressure has been linked to a reduction in free volume [111, 112]. This pressure dependence is incorporated in the material model by making the shear strength $g^{(\beta)}$ of slip system β a linear function of the pressure:

$$g^{(\beta)} = \begin{cases} \tau_y + \mu p & p \geq 0 \\ \tau_y & p < 0 \end{cases}, \quad (6.28)$$

where μ is the pressure sensitivity coefficient and p is a measure of the pressure transverse to the fiber direction. The pressure is calculated using terms of the 2nd Piola-Kirchhoff stress and for a tow with fibers placed in the 11 direction, this pressure would be:

$$p = -\frac{1}{2}(S_{22} + S_{33}). \quad (6.29)$$

The S_{11} component is in this case not taken into account, as it is assumed that the stresses in this direction are dominated by the fibers instead of the matrix. As a shear formulation, a rate dependent model similar to the one proposed by Asaro [62] is used:

$$\dot{\gamma}^{(\beta)} = \dot{\gamma}_0 \text{sign}(\tau^{(\beta)}) \left(\frac{\tau^{(\beta)}}{g^{(\beta)}} \right)^n \quad (6.30)$$

As within this thesis, the rate dependent response of the fibrous composite materials is considered outside of the scope, the reference strain rate $\dot{\gamma}_0$ was set to be equal to the loading rate. Furthermore, the rate sensitivity exponent was set to $n = 5$ to approach the rate insensitive limit as much as possible without introducing numerical instabilities.

The matrix

The pure matrix material was modeled as a linear Drucker-Prager model in ABAQUS[®]. The matrix was taken to be nondilational by setting the dilation angle to $\phi = 0$, and the yield surface was assumed to be a Von-Mises circle in the deviatoric plane ($K = 1$). The friction angle β in the Drucker-Prager model is related to μ as $\beta = \text{atan}(\mu)$. The matrix is modeled as an elastic, perfectly plastic material in the sense that there is no strain hardening applied.

6.4 Simulation results

In the following section, the simulated mechanical response of the two samples are compared with experimentally obtained behavior. Both x and z-tow compression experiments are evaluated for samples A and B. Both the Hill plasticity approach and the Crystal Plasticity approach are discussed. The compressive stress-strain curves obtained using the Hill plasticity approach are shown in Figure 6.10.

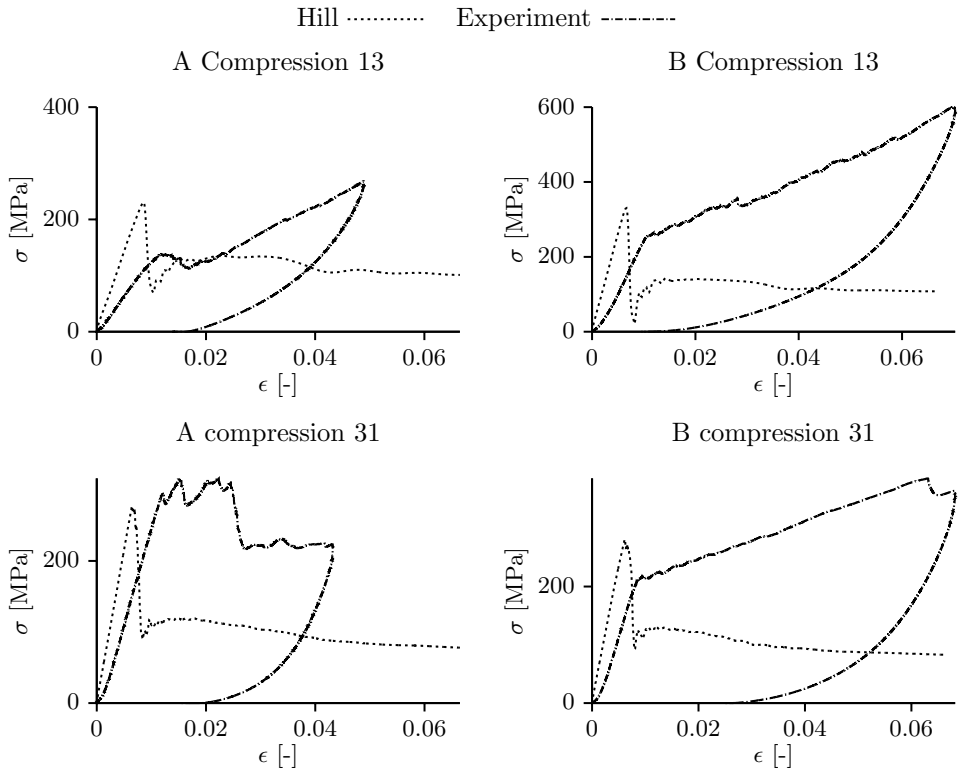


Figure 6.10: An overview of the y and x-direction compression simulations for sample A and B. The Hill plasticity approach is compared to experimentally obtained curves.

As can be seen in Figure 6.10, there is a significant mismatch between the simulated and experimentally obtained compressive stress-strain curves. Initially, the simulations over predict the stiffness of the sample. After the peak is reached, a sharp drop in the compressive stress shows the lack of the ability of the Hill homogenization model to capture the hardening.

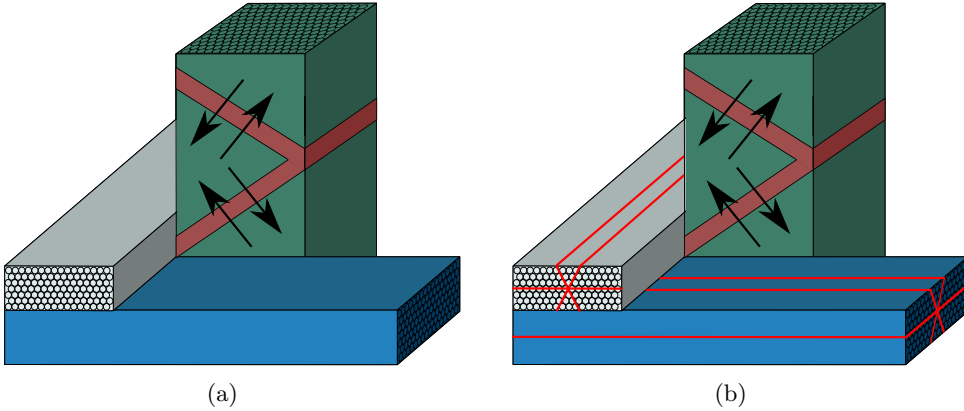


Figure 6.11: An overview of the shear deformation invoked by the kinking in the vertical z-tow during compression in the z-direction. Figure (a) shows the tows modeled with the Hill plasticity approach where the shear deformation that forms the kinks is unconstrained. Figure (b) shows the location and orientation of the slip planes in the situation where the tows are modeled with Crystal Plasticity. The presence of the slip planes in the tows constrains the shear deformation needed to form kinks.

In contrast to the plain weave compression simulation presented in the first two chapters, where the shear deformation invoking the kinking is in the laminated plane, there is a shear deformation introduced transverse to the fibers in the horizontally placed x- and y-tows of the 3DNOOBED composites. In reality, this shearing mode will be blocked by the elastic fibers in the tow. For the z-tow compression, this mechanism is illustrated in Figure 6.11a. The black arrows in Figure 6.11a indicate the direction of shearing that triggers the kink-bands in the z-direction tow. As the Hill plasticity approach does not account for the micro-structure of the fibers, the shear deformation is transmitted through the horizontally placed blue tows in Figure 6.11a. As has been discussed in Chapter 5, a Crystal Plasticity model can be used to take into account the micro structural geometry of the tows. The compressive stress-strain curves of the simulations with the tows modeled using a Crystal Plasticity approach can be seen in Figure 6.12. The figure shows that the predicted initial stiffness and peak stress of the simulations with Crystal Plasticity is similar to the the predicted initial stiffness of the simulations based on the Hill plasticity approach. In the post-peak regime, Figure 6.12 shows that the simulations based on Crystal Plasticity show a slightly increased hardening that is still lower than the hardening observed in the experiments.

Figure 6.11b illustrates a z-tow compression model where the Crystal Plasticity model has been used in the tows. The horizontally placed blue tow is enhanced with the red slip systems. These slip planes block the shear deformation indicated by the black lines and fortify the stress-strain responses shown in Figure 6.12.

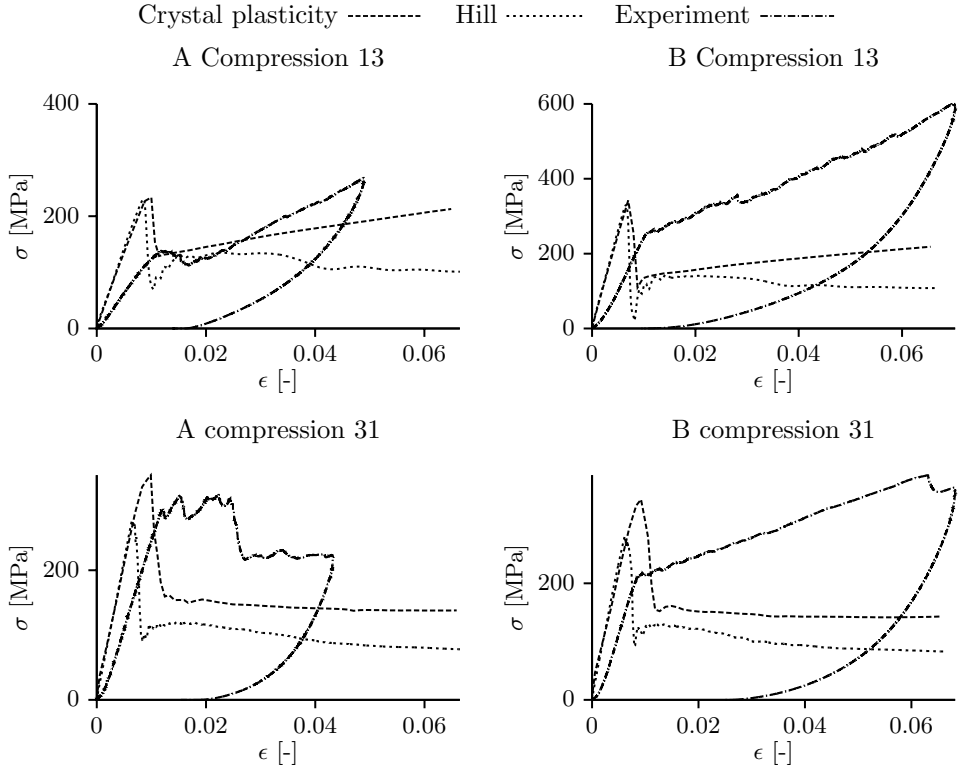


Figure 6.12: An overview of the y and x-direction compression simulations for sample A and B. The Crystal Plasticity approach is compared to experimentally obtained curves and the Hill plasticity results.

6.4.1 Pressure sensitivity

In order to investigate the effect of a pressure sensitive matrix, a value of $\mu = 0.2$ is chosen to be used with the crystal plasticity model, which is similar to coefficients found in the literature [107]. The resulting stress-strain curves can be seen in Figure 6.13. Adding the pressure sensitive shear yield stress to the Crystal Plasticity approach significantly increases the slope of the hardening and the material can sustain a larger load after the initial peak load.

6.4.2 Imperfection angle

It is well known that the formation of kink-bands is sensitive to the misalignment of the fibers with respect to the applied compressive load [15, 17]. To investigate the role of the misalignment that triggers fiber kinking, the imperfection angle ϕ has been varied. The results in Figure 6.14, show that the peaks in the graphs are reduced when the imperfection angle increases. For the z-tow compression simulations, the peaks nearly vanish, while for the x-direction compression simulations, a small peak remains present for larger imperfection angles. It can be concluded that imperfections introduced by the waviness in the tows cause a significant reduction of the strength of

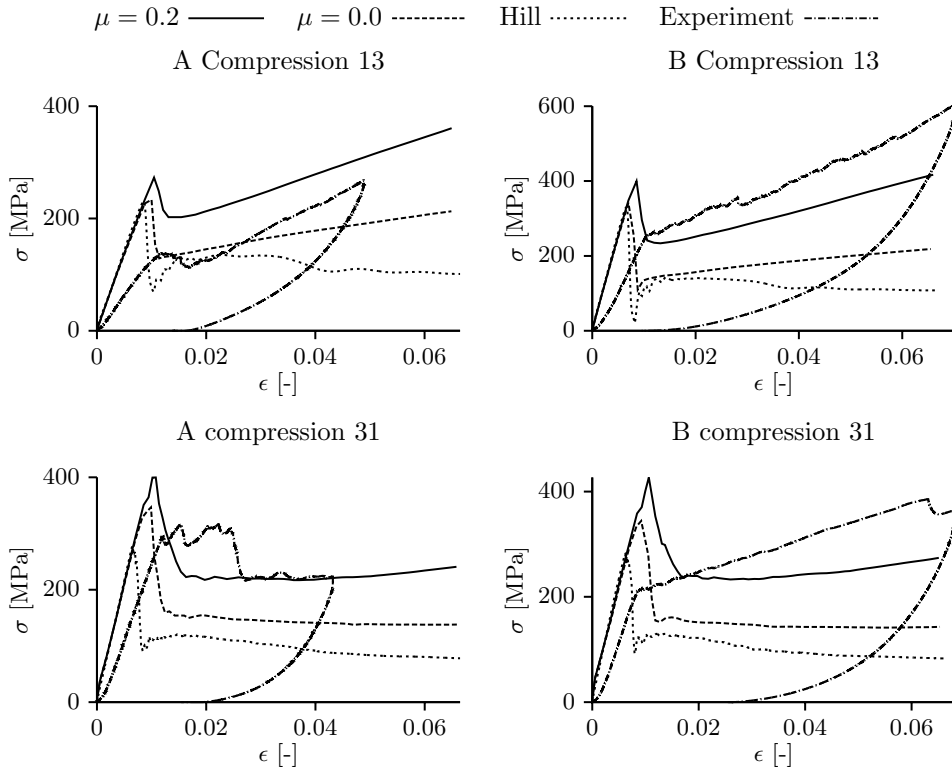


Figure 6.13: A comparison between a simulations of plain weave composites under tensile loading modeled with Hill plasticity and a micro approach where individual fibers are modeled.

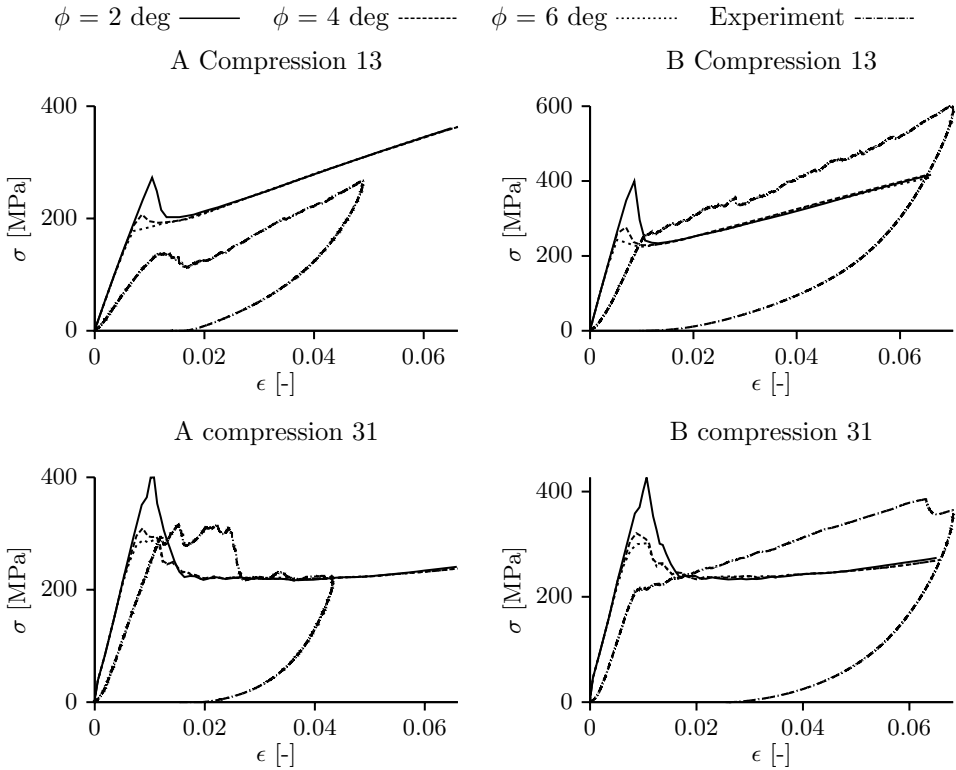


Figure 6.14: A comparison between a simulations of plain weave composites under tensile loading modeled with Hill plasticity and a micro approach where individual fibers are modeled.

the composite.

6.4.3 Axial stiffness of the tow

In addition to reducing the compressive strength of composites, it has been reported in the literature that the waviness of fibers in a tow can significantly reduce the stiffness of a tow [113]. As in the current modeling approach the tows are homogenized using Voigt averages that assume perfectly straight fibers, the initial modulus is over predicted. An analyses of the waviness in the tows has been made in Appendix B. To correct for this phenomenon, a knockdown factor ck has been applied to the axial stiffness of the tows such that effective axial stiffness is $E_{\text{axial}} = E_1/ck$. Due to the complex nature of the micro structure and variation of fiber angles, rather than identifying a specific value to be applied, a range of knockdown factors is presented in Figure 6.15. As can

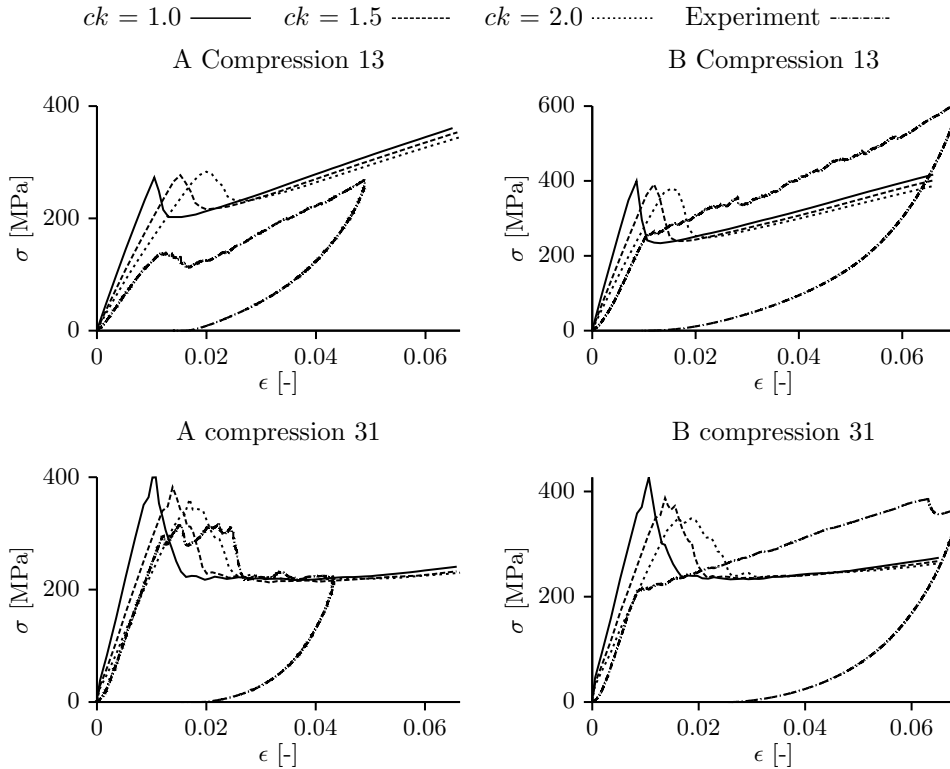


Figure 6.15: A comparison between a simulations of plain weave composites under tensile loading modeled with Hill plasticity and a micro approach where individual fibers are modeled.

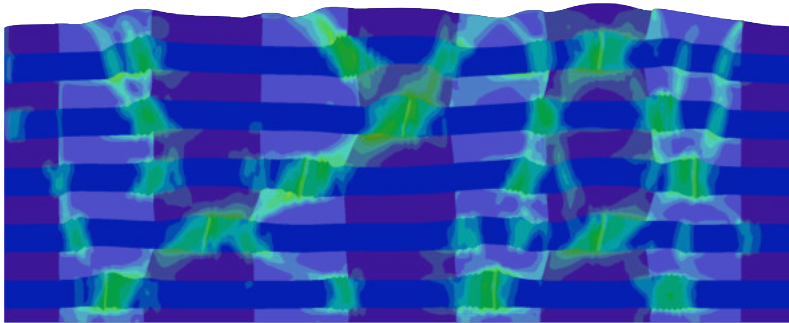
be seen in Figure 6.15, the initial stiffness of the simulations is reduced and there is a minor reduction in the hardening response. The simulations indicate that, depending on the experiment, the measured stiffness can be approached if a knockdown factor of 1.5-2.0 is used.

6.5 Kink-bands

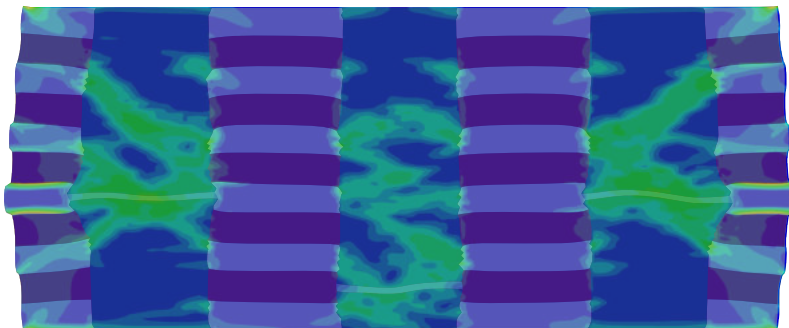
The results in Chapter 3 showed that kink bands can be modeled with a homogenized tow model. A common feature of the Hill plasticity model and the Crystal Plasticity model is that the width of the kinks predicted by both models is dependent on the mesh size used in the simulation. Based on the experiments, the mesh size in the simulations has been chosen such that the simulated kinks are ≈ 0.5 mm wide.

Figure 6.16b shows contours of the maximum principle strain. As can be seen in Figure 6.16a, kink bands form in the x-direction tows and are transmitted through matrix pockets and y-direction tows in a similar way as could be seen in the micrographs shown in Figure 6.5.

The contours of the maximum principle strain in the z-tow compression simulations can be seen in Figure 6.16b. Similar to the kinks observed in Figure 6.16a, the simulated kinks in the z-direction simulations are trapped in the z-direction tows. No transmission through matrix pockets and x- or y-direction tows is observed.



(a)



(b)

Figure 6.16: Contours of the maximum principle strain. The x-direction compression simulation is shown in Figure (a) and the z-tow compression simulation is shown in (b).

6.6 Conclusion

The simulations in this chapter have shown that although the Hill plasticity approach works for 2D textile composites under compression, the approach is inaccurate in predicting the stress-strain response of 3DNOOBED composites in general and the reflecting kink-bands in particular. In 3DNOOBED composites there are fiber bundles placed perpendicular to the plane in which the shear deformation occurs that forms the kinks. The propagation of kinks across tows loaded under compressive loading is blocked by some of these tows, increasing the hardening of the stress-strain response. In addition, in order to get a representative hardening response, it is necessary to include pressure sensitivity to the constitutive modeling of both tows and matrix. Contour plots of the strains in the simulations showed kinking. The transmission of the kinks in the x-direction compression experiments through the surrounding matrix pockets and y-direction tow is reproduced by the model. In the z-tow compression simulations, a trapping of the kinks in the compressed tows can be observed that is similar to the trapping observed in the compressive experiments.

Chapter 7

Conclusions and recommendations

The main conclusions of the research presented in this Thesis are summarized in the first part of this chapter. The second part of this chapter will list a set of recommendations for further research.

7.1 Conclusion

A plane strain model of a plain weave composite is presented in Chapter 2 where individual fibers are modeled. The modeling of individual fibers allows for an accurate representation of kink-bands as the relevant length scale, the diameter of a fiber, is included in the model. When examining the effect of the phase shifts between different layers in the laminate, the simulations indicate that an in-phase stacking provides a lower-bound for the compressive strength and the out-of-phase stacking provides an upper bound of the strength of the laminate under compressive loading. Furthermore, the model presented in Chapter 2 can be used as a tool to gain insight in the relevant geometric and constitutive parameters of the weave that contribute to failure. As an example, the parameter studies reveal that although the decrease of the undulation angle of the weave is likely to reduce the volume fraction of the fibers present, the compressive strength of the weave increases.

Based on the micro-model presented in Chapter 2, a tow level homogenization scheme using Hill plasticity relation has been formulated. A meso-scale model of a plain weave composite has been made where the tows are the smallest details modeled. Due to the absence of the kinematics of individual fibers, the size of the resulting kink-band depends on the size of the mesh. To be able to perform accurate predictions, the micro-model presented in Chapter 2 is used to calibrate the mesh size.

The model was used to simulate the formation of kink-bands in compressive open hole coupon test of different sizes. Using the simulations, a detailed overview of the series of events leading to catastrophic failure was made. It appears that during compressive loading, a region of plastic deformation originates near the hole. This plastic zone grows parallel to the loading direction, acting as a splitting mechanism causing relatively notch insensitive behavior with respect to the size of the sample and the size of the tows.

In chapter 4 the performance of the Hill plasticity based homogenization is evaluated for tows under tensile loading. Under compressive loading, the failure of a textile composite under compression is triggered by the plasticity of the matrix in the tow. When loaded in tension, plasticity in a tow allows the stretching of a tow, but final failure of the tow is related to the strength of the fibers. The stretching of a tow under tensile loading requires large local deformations and rotations of the tow. As Hill plasticity model lacks a description of the texture of the tow, the material can rotate freely, irrespective of the fiber orientations. As a result, a reduction of stiffness in the fiber direction is observed. Without including fiber bending effects and therefore retaining the mesh-sensitivity of kink-bands, a Crystal Plasticity model uses slip systems to represent the texture of fibers in a tow. The orientation of these slip systems is independent of the plastic deformation and therefore the description of the texture remains accurate in the case of large rotations.

In Chapter 5 a 3DNOOBED composite under shear loading is studied both experimentally and numerically. Experiments show that these 3DNOOBED composites have minimal damage prior to failure and show a significant amount of hardening when loaded in shear. The Hill plasticity based homogenization for tows is unable to capture the hardening response of the 3DNOOBED composites as the homogenized tows does not include a description of the texture of the fibers. The organization of the tows in the sample causes a buildup of hydrostatic pressure due to incompatible failure modes. The slip planes in the Crystal Plasticity model do provide a description of the fibers in the tows. The incompatible failure modes caused by the Crystal Plasticity mode already allow hardening of the global stress strain response. If a pressure sensitive yield stress is taken into account, the hardening in the 3DNOOBED simulations matches the experimentally observed hardening.

In the final study in this thesis, the 3DNOOBED samples presented in Chapter 5 were studied under compressive loading. Again, the homogenization strategies used in Chapter 3 and 4 were compared with experiments. Similar trends as in Chapter 5, could be observed. The Crystal Plasticity model outperformed the Hill plasticity approach. Taking a pressure sensitive yield stress into account proved to be a vital part in capturing the hardening seen in experiments. In contrast to the shear experiments in Chapter 5, the compressive response of the 3DNOOBED samples is harder to capture accurately. Although qualitatively the simulations capture the experimental observations well, a correct quantitative prediction remains difficult. In general, the compression experiments are much more sensitive with respect to imperfections present in the material. When looking at contour plots of the strains, kink bands can be observed under compression. However, it is hard to accurately capture the reflective kink-bands as observed in experiments. As the kink-bands merely act as a mechanism to allow the deformation in the compression direction, this does not have a significant effect on the compressive stress-strain response.

7.2 Recommendations

The following lists a set of recommendations that can be made based on the research presented in this thesis:

- The models presented in Chapter 2 allow for an accurate study of the formation of kink-bands in the warp tow. However, the constitutive relations used for the

matrix and the fibers are oversimplified in order to capture the essence of kinking. For a more accurate model, the carbon fibers could be modeled as anisotropic entities and a more realistic model for the matrix can be used, such as the rate dependent Eindhoven Glassy Polymer model [114]. The current numerical framework allows for a straightforward extension.

- During the production of composites there are often significant temperature differences. Currently the influence of the residual stresses is neglected in this study. The micro model presented in Chapter 2 together with temperature dependent constitutive models for the fibers and matrix would be a good place to start to investigate the effect of thermal stresses.
- A downside of homogenizing the tows, either with Hill plasticity or Crystal Plasticity, is that the geometry of the fibers is not explicitly modeled. The absence of bending effects of the fibers causes the width of the resulting kink-bands to be mesh dependent. A technique to solve this mesh dependency, such as non-local models [115], should be investigated keeping in mind the relatively large size of the models.
- The compressive response of 3DNOOBED composites is sensitive to imperfections in the material. In order to get a good match between the simulations and experiments, a measure of these imperfections has to be taken into account in the model. One option would be to vary the local element orientations to represent the waviness, but this can only be done after a model has been implemented for the tows that is able to represent the bending effects introduced by the fibers in the tows.

Appendix A

3DNOOBED shear sensitivities

In Chapter 5 two parameters needed to be determined to match the experimental results: the shear yield strength τ_y and the pressure strengthening coefficient μ . To illustrate the effect they have on the results, a range of τ_y and μ is presented in Figure A.1. It can be seen in Figure A.1a and A.1c that the shear strength τ_y linearly increases the yield strength of the composite and has little to no effect on the hardening. The pressure coefficient μ does not affect the yield strength or the initial stress-strain behavior, it approximately linearly affects the hardening response at higher strains. These two parameters therefore provide an excellent means to tune the mechanical response of the model to better match the experiments.

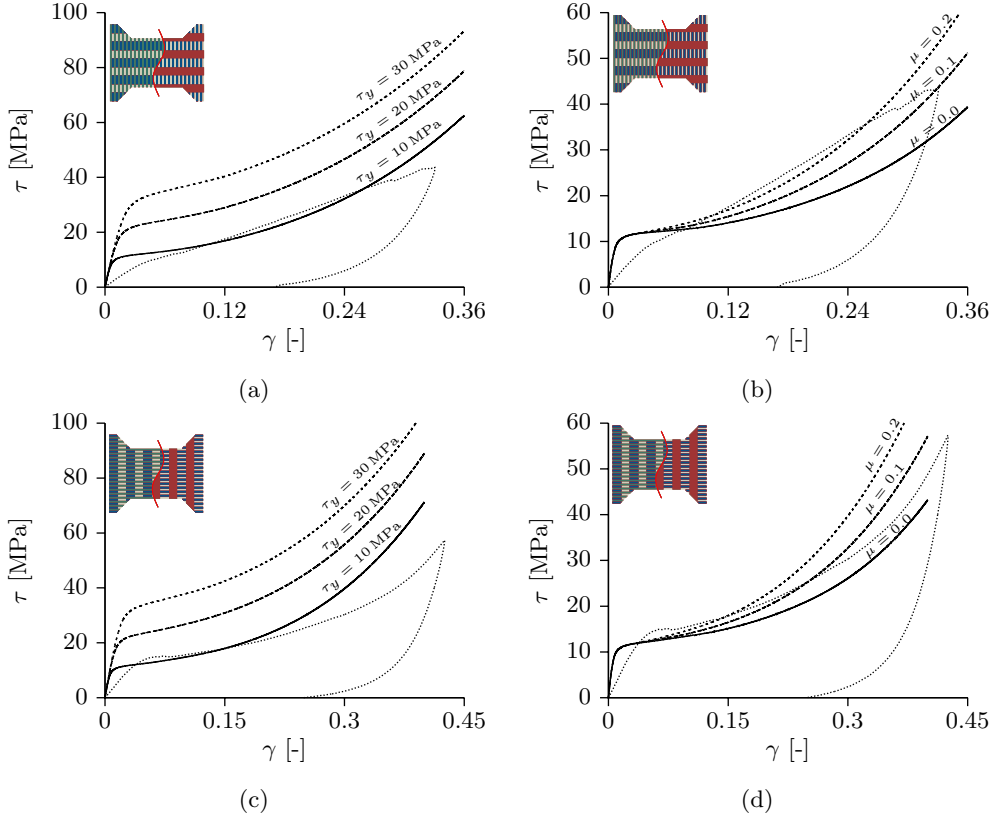


Figure A.1: The effect of τ_y and μ . The simulation results for different values of τ_y are shown in Figures A.1a and A.1c for the xz and zx orientation respectively. Figures A.1b and A.1d show the simulation results using different values of μ for respectively the xz and zx orientation.

Appendix B

Quantifying waviness

The waviness of the fibers in sample A and sample B is characterized in this appendix. Note that all shear experiments presented in Chapter 5 were performed on sample A. The samples used to make the images in Figures B.1 and B.2 were sectioned with a diamond cutting saw and polished to an RMS roughness of < 50 nm to see both the fiber and crack distribution in the tows. The global waviness of the x- and y-direction tows (as seen in the XCT scans) was reconfirmed in the microscope images, but the polishing revealed the internal waviness of the z-direction tows. Directionality analysis was performed with the image processing software ImageJ.

The average histograms of ten of the sample A x-tows and five of the sample A z-tows are shown in Figures B.1c and B.1d respectively. Although the x-tows have a more visible distortion along their length, they only have a variance in their direction of $\sigma^2 = 2.95^\circ$, whereas the low volume fraction of the z-tows leads to a greater degree of internal waviness during processing and a variance of $\sigma^2 = 7.84^\circ$. This suggests that the z-tows will have a greater knockdown in stiffness and strength than the x-tows.

For sample B, the average histogram of ten x-tows is shown in Figure B.2c and the average histogram of 5 z-tows is shown in Figure B.2d. The histograms indicate that with respect to sample A, there is more waviness in sample B.

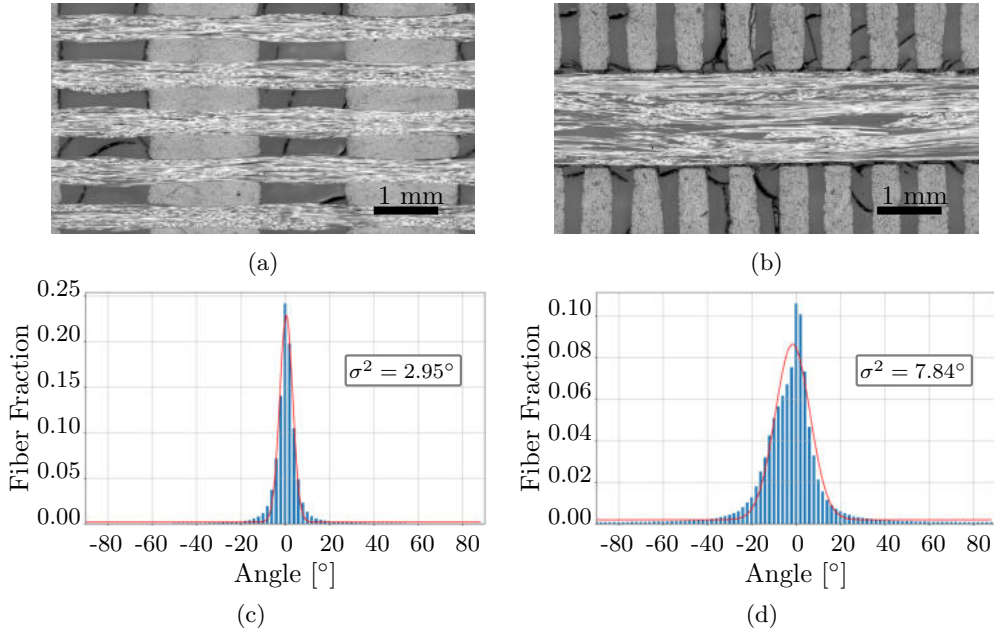


Figure B.1: A characterization of the waviness in sample A. Figures (a) and (c) show the waviness in a x-direction tow and Figure (b) and (d) show the waviness in a z-direction tow.

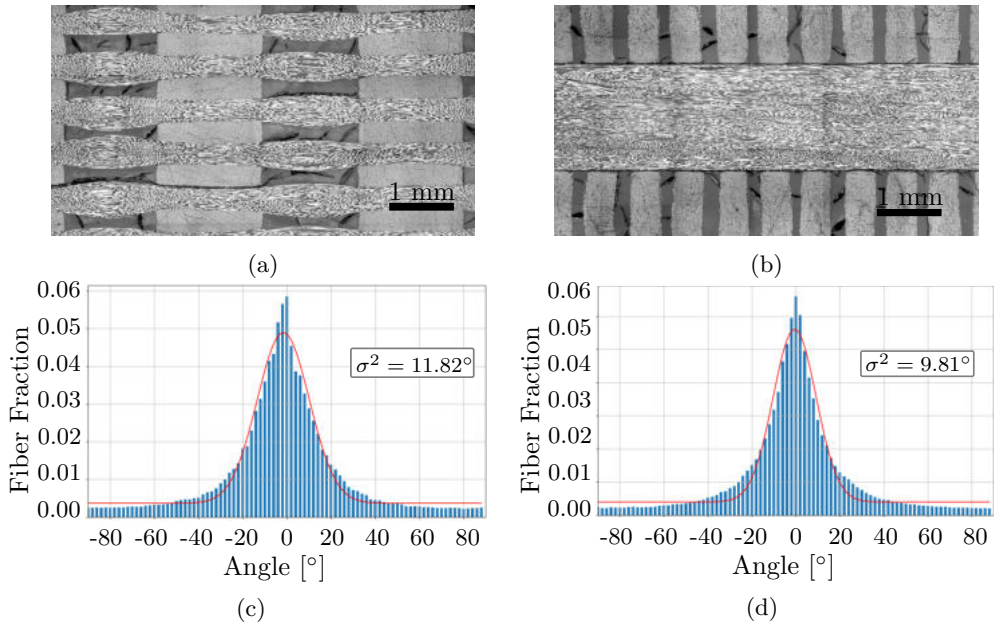


Figure B.2: A characterization of the waviness in sample B. Figures (a) and (c) show the waviness in a x-direction tow and Figure (b) and (d) show the waviness in a z-direction tow.

Bibliography

- [1] Composite Materials Handbook Series MIL-HDBK-17: Volume 3. Polymer Matrix Composites Material Usage, Design and Analysis.
- [2] V. Gupta, K. Anand, and M. Kryska. Failure mechanisms of laminated carbon-carbon composites–I. Under uniaxial compression. *Acta Metallurgica et Materialia*, 42(3):781–795, 1994.
- [3] J.M.J. Schormans, W. Wilson, J.J.C. Remmers, and V.S. Deshpande. Notch sensitivity in woven carbon-fiber reinforced plastics. *In preparation*, 2018.
- [4] L. Meza, J.M.J. Schormans, J.J.C. Remmers, and V.S. Deshpande. Capturing the inhibition of shear failure in 3d non-woven carbon fibre composites using crystal plasticity modeling. *In preparation*, 2018.
- [5] J.M.J. Schormans, L. Meza, J.J.C. Remmers, and V.S. Deshpande. On the enhanced ductility of 3d composites under compressive loading. *In preparation*, 2018.
- [6] N.V. De Carvalho, S.T. Pinho, and P. Robinson. Numerical modelling of woven composites: Biaxial loading. *Composites Part A: Applied Science and Manufacturing*, 43(8):1326–1337, 2012.
- [7] P. Tan, L. Tong, and G.P. Steven. Modelling for predicting the mechanical properties of textile composites–A review, 1997.
- [8] K.W. Gan, M.R. Wisnom, and S.R. Hallett. Effect of high through-thickness compressive stress on fibre direction tensile strength of carbon/epoxy composite laminates. *Composites Science and Technology*, 90:1–8, 2014.
- [9] N.V. De Carvalho, S.T. Pinho, and P. Robinson. Reducing the domain in the mechanical analysis of periodic structures, with application to woven composites. *Composites Science and Technology*, 71(7):969–979, 2011.
- [10] S. Sivashanker, N.A. Fleck, and M.P.F. Sutcliffe. Microbuckle propagation in a unidirectional carbon fibre-epoxy matrix composite. *Acta Materialia*, 44(7):2581–2590, 1996.
- [11] P. Berbinau, C. Soutis, and I.A. Guz. Compressive failure of 0 unidirectional carbon-fibre-reinforced plastic (CFRP) laminates by fibre microbuckling. *Composites Science and Technology*, 59(9):1451–1455, 1999.

BIBLIOGRAPHY

- [12] S.H. Lee and A.M. Waas. Compressive response and failure of fiber reinforced unidirectional composites. *International Journal of Fracture*, 100(3):275–306, 1999.
- [13] J. Lee and C. Soutis. A study on the compressive strength of thick carbon fibre–epoxy laminates. *Composites Science and Technology*, 67(10):2015–2026, 2007.
- [14] Rosen and B. W. Mechanics of composite strengthening. 1965.
- [15] A.S. Argon. Fracture of composites. *Treatise on Materials Science and Technology vol.1—Treatise on Materials Science and Technology vol.1*, pages 79—114—xii+346, 1972.
- [16] B. Budiansky and N.A. Fleck. Compressive Kinking of Fiber Composites: A Topical Review. *Applied Mechanics Reviews*, 47(6S):S246, 1994.
- [17] B. Budiansky and N.A. Fleck. Compressive failure of fibre composites. *Journal of the Mechanics and Physics of Solids*, 41(1):183–211, 1993.
- [18] S. Kyriakides, R. Arseculeratne, E.J. Perry, and K.M. Liechti. On the compressive failure of fiber reinforced composites. *International Journal of Solids and Structures*, 32(6-7):689–738, 1995.
- [19] S. Pimenta, R. Gutkin, S.T. Pinho, and P. Robinson. A micromechanical model for kink-band formation: Part I – Experimental study and numerical modelling, 2009.
- [20] T.J. Vogler and S. Kyriakides. On the initiation and growth of kink bands in fiber composites: Part I. experiments. *International Journal of Solids and Structures*, 38(15):2639–2651, 2001.
- [21] T.J. Vogler, S.-Y. Hsu, and S. Kyriakides. On the initiation and growth of kink bands in fiber composites. Part II: analysis. *International Journal of Solids and Structures*, 38(15):2653–2682, 2001.
- [22] A. Altmann, R. Taubert, U. Mandel, R. Hinterhoelzl, and K. Drechsler. A continuum damage model to predict the influence of ply waviness on stiffness and strength in ultra-thick unidirectional Fiber-reinforced Plastics. *Journal of Composite Materials*, 50(20):2739–2755, 2016.
- [23] F. Reifsnider, K.L. and Mirzadeh. Compressive Strength and Mode of Failure of 8H Celion 3000/PMR15 Woven Composite Material. *Journal of Composites Technology and Research*, 10(4):156–164, 1988.
- [24] M. Karayaka and P. Kurath. Deformation and Failure Behavior of Woven Composite Laminates. *Journal of Engineering Materials and Technology*, 116(2):222, 1994.
- [25] K.B. Breiling and D.O. Adams. Effects of Layer Nesting on Compression-Loaded 2D Woven Textile Composties. *Journal of Composite Materials*, 1996.
- [26] R.D. Hale and M. Villa. Influence of Opposing Wave Nesting in Compression-Loaded Composites. *Journal of Composite Materials*, 37(13):1149–1166, 2003.

- [27] N.V. De Carvalho, S.T. Pinho, and P. Robinson. An experimental study of failure initiation and propagation in 2D woven composites under compression. *Composites Science and Technology*, 71(10):1316–1325, 2011.
- [28] T. Ishikawa and T.-W. Chou. Stiffness and strength behaviour of woven fabric composites. *Journal of Materials Science*, 17(11):3211–3220, 1982.
- [29] P. Tan, L. Tong, and G.P. Steven. Micromechanics models for the elastic constants and failure strengths of plain weave composites. In *Composite Structures*, volume 47, pages 797–804. Elsevier, 1999.
- [30] N.V. De Carvalho, S.T. Pinho, and P. Robinson. Analytical modelling of the compressive and tensile response of woven composites. *Composite Structures*, 94(9):2724–2735, 2012.
- [31] S.V. Lomov, D.S. Ivanov, I. Verpoest, M. Zako, T. Kurashiki, H. Nakai, and S. Hirose. Meso-FE modelling of textile composites: Road map, data flow and algorithms. *Composites Science and Technology*, 67(9):1870–1891, 2007.
- [32] J.D. Whitcomb. Three-dimensional stress analysis of plain weave composites. 1989.
- [33] J.D. Whitcomb and X. Tang. Effective Moduli of Woven Composites. *Journal of Composite Materials*, 35(23):2127–2144, 2001.
- [34] M.G. Kollegal and S. Sridharan. Strength Prediction of Plain Woven Fabrics. *Journal of Composite Materials*, 34(3):240–257, 2000.
- [35] M. Zako, Y. Uetsuji, and T. Kurashiki. Finite element analysis of damaged woven fabric composite materials. *Composites Science and Technology*, 63(3-4):507–516, 2003.
- [36] H.S. Huang. Influence of phase shift on the responses of woven laminated composites. *Composite Structures*, 130:143–154, 2015.
- [37] S. Pimenta, R. Gutkin, S.T. Pinho, and P. Robinson. A micromechanical model for kink-band formation: Part II-Analytical modelling. *Composites Science and Technology*, 69(7-8):956–964, 2009.
- [38] J. Awerbuch and M.S. Madhukar. Notched Strength of Composite Laminates : Predictions and Experiments - A Review. *Journal of Reinforced Plastics and Composites of Reinforced*, 4(1):3–159, 1985.
- [39] M.P.F. Sutcliffe and N.A. Fleck. Effect of geometry on compressive failure of notched composites. *International Journal of Fracture*, 59(2):115–132, 1993.
- [40] M.R. Wisnom, S.R. Hallett, and C. Soutis. Scaling Effects in Notched Composites. *Journal of Composite Materials*, 44(2):195–210, 2009.
- [41] X. Xu, M.R. Wisnom, X. Li, and S.R. Hallett. A numerical investigation into size effects in centre-notched quasi-isotropic carbon/epoxy laminates. *Composites Science and Technology*, 111:32–39, 2015.

BIBLIOGRAPHY

- [42] S.R. Hallett, B.G. Green, W.G. Jiang, and M.R. Wisnom. An experimental and numerical investigation into the damage mechanisms in notched composites. *Composites Part A: Applied Science and Manufacturing*, 40(5):613–624, 2009.
- [43] F.P. van der Meer, C. Oliver, and L.J. Sluys. Computational analysis of progressive failure in a notched laminate including shear nonlinearity and fiber failure. *Composites Science and Technology*, 70(4):692–700, 2010.
- [44] P.P. Camanho, P. Maimí, and C.G. Dávila. Prediction of size effects in notched laminates using continuum damage mechanics. *Composites Science and Technology*, 67(13):2715–2727, 2007.
- [45] L.W. Chang, S.S. Yau, and T.W. Chou. Notched strength of woven fabric composites with moulded-in holes. *Composites*, 18(3):233–241, 1987.
- [46] J.L.Y. Tan, V.S. Deshpande, and N.A. Fleck. Failure mechanisms of a notched CFRP laminate under multi-axial loading. *Composites Part A: Applied Science and Manufacturing*, 77:56–66, 2015.
- [47] W. Tan and B.G. Falzon. Modelling the nonlinear behaviour and fracture process of AS4/PEEK thermoplastic composite under shear loading. *Composites Science and Technology*, 126:60–77, 2016.
- [48] C. Soutis, N.A. Fleck, and P.A. Smith. Failure Prediction Technique for Compression Loaded Carbon Fibre-Epoxy Laminate with Open Holes. *Journal of Composite Materials*, 25(11):1476–1498, 1991.
- [49] Z.C. Su, T.E. Tay, M. Ridha, and B.Y. Chen. Progressive damage modeling of open-hole composite laminates under compression. *Composite Structures*, 122:507–517, 2015.
- [50] N. Fleck, P. Jelf, and P. Curtis. Compressive Failure of Laminated and Woven Composites. *Journal of Composites Technology and Research*, 17(3):212, 1995.
- [51] S.V. Lomov, G. Huysmans, Y. Luo, R.S. Parnas, A. Prodromou, I. Verpoest, and F.R. Phelan. Textile composites: modelling strategies. *Composites Part A: Applied Science and Manufacturing*, 32(10):1379–1394, 2001.
- [52] I. Verpoest and S. Lomov. Virtual textile composites software : Integration with micro-mechanical, permeability and structural analysis. *Composites Science and Technology*, 65(15-16):2563–2574, 2005.
- [53] D.S. Ivanov, S.V. Lomov, S.G. Ivanov, and I. Verpoest. Stress distribution in outer and inner plies of textile laminates and novel boundary conditions for unit cell analysis. *Composites Part A: Applied Science and Manufacturing*, 41(4):571–580, 2010.
- [54] X. Tang and J.D. Whitcomb. Progressive Failure Behaviors of 2D Woven Composites. *Journal of Composite Materials*, 37(14):1239–1259, 2003.
- [55] Dassault Systmes. Abaqus-theoy manual version 6.14.

- [56] Q. Qiuling Wang and G.S. Springer. Moisture Absorption and Fracture Toughness of PEEK Polymer and Graphite Fiber Reinforced PEEK. *Journal of Composite Materials*, 23(5):434–447, 1989.
- [57] R. Hill. A Theory of the Yielding and Plastic Flow of Anisotropic Metals. *Proceedings of the Royal Society A: Mathematical, Physical and Engineering Sciences*, 193(1033):281–297, 1948.
- [58] S.L. Lemanski, J. Wang, M.P.F. Sutcliffe, K.D. Potter, and M.R. Wisnom. Modelling failure of composite specimens with defects under compression loading. *Composites Part A: Applied Science and Manufacturing*, 48:26–36, 2013.
- [59] C. Soutis, P.T. Curtis, and N.A. Fleck. Compressive Failure of Notched Carbon Fibre Composites. *Proceedings of the Royal Society A: Mathematical, Physical and Engineering Sciences*, 440(1909):241–256, 1993.
- [60] K. Marlett, Y. Ng, and J. Tomblin. Hexcel 8552 IM7 unidirectional prepreg 190 gsm & 35% RC qualification material property data report. 2011.
- [61] K.S. Chan, M.Y. He, and J.W. Hutchinson. Cracking and stress redistribution in ceramic layered composites. *Materials Science and Engineering: A*, 167(1-2):57–64, 1993.
- [62] R.J. Asaro. Crystal Plasticity. *Journal of Applied Mechanics*, 50(4b):921, 1983.
- [63] G.C. Jacob, J.F. Fellers, S. Simunovic, and J.M. Starbuck. Energy absorption in polymer composites for automotive crashworthiness. *Journal of Composite Materials*, 36(7):813–850, 2002.
- [64] A.P. Mouritz, E. Gellert, P. Burchill, and K. Challis. Review of advanced composite structures for naval ships and submarines. *Composite Structures*, 53(1):21–24, 2001.
- [65] C.C. Poe, H.B. Dexter, and I.S. Raju. Review of the NASA Textile Composites Research. *Journal of Aircraft*, 36(5):876–884, 1999.
- [66] D. Carolan, A. Ivankovic, A.J. Kinloch, S. Sprenger, and A.C. Taylor. Toughened carbon fibre-reinforced polymer composites with nanoparticle-modified epoxy matrices. *Journal of Materials Science*, 52(3):1767–1788, 2017.
- [67] I.M. Daniel, J.-J. Luo, P.M. Schubel, and B.T. Werner. Interfiber/interlaminar failure of composites under multi-axial states of stress. *Composites Science and Technology*, 69(6):764–771, 2009.
- [68] G.L. Farley and R.M. Jones. Crushing Characteristics of Continuous Fiber-Reinforced Composite Tubes. *Journal of Composite Materials*, 26(1):37–50, 1992.
- [69] P.M. Jelf and N.A. Fleck. Compression Failure Mechanisms in Unidirectional Composites. *Journal of Composite Materials*, 26(18):2706–2726, 1992.
- [70] T.J. Vogler and S. Kyriakides. On the axial propagation of kink bands in fiber composites : Part i experiments. *International Journal of Solids and Structures*, 36(4):557–574, 1999.

- [71] T. Huang, Y. Wang, and G. Wang. Review of the Mechanical Properties of a 3D Woven Composite and Its Applications. *Polymer-Plastics Technology and Engineering*, 57(8):740–756, 2018.
- [72] A.P. Mouritz, M.K. Bannister, P.J. Falzon, and K.H. Leong. Review of applications for advanced three-dimensional fibre textile composites. *Composites Part A: Applied Science and Manufacturing*, 30(12):1445–1461, 1999.
- [73] L. Tong, A.P. Mouritz, and M.K. Bannister. *3D fibre reinforced polymer composites*. Elsevier, 2002.
- [74] R. Kamiya, B.A. Cheeseman, P. Popper, and T.W. Chou. Some recent advances in the fabrication and design of three-dimensional textile preforms: A review, 2000.
- [75] S. Kazemahvazi, N. Khokar, S. Hallstrom, H.N.G. Wadley, and V.S. Deshpande. Confluent 3D-assembly of fibrous structures. *Composites Science and Technology*, 127:95–105, 2016.
- [76] S. Schmidt, S. Beyer, H. Knabe, H. Immich, R. Meistring, and A. Gessler. Advanced ceramic matrix composite materials for current and future propulsion technology applications. In *Acta Astronautica*, volume 55, pages 409–420, 2004.
- [77] R. Umer, H. Alhussein, J. Zhou, and W. Cantwell. The mechanical properties of 3D woven composites. *Journal of Composite Materials*, 51(12):1703–1716, 2017.
- [78] B.N. Cox, M.S. Dadkhah, and W.L. Morris. On the tensile failure of 3D woven composites. *Composites Part A: Applied Science and Manufacturing*, 27(6):447–458, 1996.
- [79] B.N. Cox, M.S. Dadkhah, W.L. Morris, and J.G. Flintoff. Failure Mechanisms of 3D Woven Composites in Tension, Compression and Bending. *Acta Mater. Mater*, 42(12):3967–3984, 1994.
- [80] B.N. Cox, M.S. Dadkhah, R.V. Inman, W.L. Morris, and J. Zupon. Mechanisms of compressive failure in 3D composites. *Acta Metallurgica Et Materialia*, 40(12):3285–3298, 1992.
- [81] S. Das, K. Kandan, S. Kazemahvazi, H.N.G. Wadley, and V.S. Deshpande. Compressive response of a 3D non-woven carbon-fibre composite. *International Journal of Solids and Structures*, 136-137:137–149, 2018.
- [82] A.G. Evans and W.F. Adler. Kinking as a mode of structural degradation in carbon fiber composites. *Acta Metallurgica*, 26(5):725–738, 1978.
- [83] M. Ansar, W. Xinwei, and Z. Chouwei. Modeling strategies of 3D woven composites: A review. *Composite Structures*, 93(8):1947–1963, 2011.
- [84] P. Tan, L. Tong, G.P. Steven, and T. Ishikawa. Behavior of 3D orthogonal woven CFRP composites. Part I. Experimental investigation. *Composites Part A: Applied Science and Manufacturing*, 31(3):259–271, 2000.

- [85] M.A. McGlockton, B.N. Cox, and R.M. McMeeking. A Binary Model of textile composites: III high failure strain and work of fracture in 3D weaves. *Journal of the Mechanics and Physics of Solids*, 51(8):1573–1600, 2003.
- [86] S. Song, A.M. Waas, K.W. Shahwan, X. Xiao, and O. Faruque. Braided textile composites under compressive loads: Modeling the response, strength and degradation. *Composites Science and Technology*, 67(15-16):3059–3070, 2007.
- [87] H. Huang and A.M. Waas. Compressive response of Z-pinned woven glass fiber textile composite laminates: Experiments. *Composites Science and Technology*, 69(14):2331–2337, 2009.
- [88] A. Puck and H. Schürmann. Failure analysis of FRP laminates by means of physically based phenomenological models. In *Failure Criteria in Fibre-Reinforced-Polymer Composites*. 1998.
- [89] F. Naya, C. González, C.S. Lopes, S. Van der Veen, and F. Pons. Computational micromechanics of the transverse and shear behavior of unidirectional fiber reinforced polymers including environmental effects. *Composites Part A: Applied Science and Manufacturing*, 92:146–157, 2017.
- [90] M. Vogler, R. Rolfes, and P.P. Camanho. Modeling the inelastic deformation and fracture of polymer composites – Part I: Plasticity model. *Mechanics of Materials*, 59:50–64, 2013.
- [91] M.R. Wisnom. The effect of fiber rotation in 45 tension test on measured shear properties. 26(1):25–32, 1995.
- [92] E.S. Shin and K.D. Pae. Effects of Hydrostatic Pressure on In-Plane Shear Properties of Graphite/Epoxy Composites. *Journal of Composite Materials*, 26(6):828–868, 1992.
- [93] P.J. Hine, R.A. Duckett, A.S. Kaddour, M.J. Hinton, and G.M. Wells. The effect of hydrostatic pressure on the mechanical properties of glass fibre/epoxy unidirectional composites. *Composites Part A: Applied Science and Manufacturing*, 36(2):279–289, 2005.
- [94] G.M. Vyas, S.T. Pinho, and P. Robinson. Constitutive modelling of fibre-reinforced composites with unidirectional plies using a plasticity-based approach. *Composites Science and Technology*, 71(8):1068–1074, 2011.
- [95] U. Mandel, R. Taubert, and R. Hinterhölzl. Mechanism based nonlinear constitutive model for composite laminates subjected to large deformations. *Composite Structures*, 132:98–108, 2015.
- [96] H. Cui, D. Thomson, A. Pellegrino, J. Wiegand, and N. Petrinic. Effect of strain rate and fibre rotation on the in-plane shear response of 45 laminates in tension and compression tests. *Composites Science and Technology*, 135(135):106–115, 2016.
- [97] N. Khokar. 3D-Weaving: Theory and Practice. *Journal of the Textile Institute*, 92(2):193–207, 2001.

BIBLIOGRAPHY

- [98] N. Khokar. Noobing: A nonwoven 3D fabric-forming process explained. *Journal of the Textile Institute*, 93(1):52–74, 2002.
- [99] N Malmgren. NM FW 3070 Datasheet, 2016.
- [100] N. Khokar. 3D fabric and a method and apparatus for producing such a 3D fabric, 2012.
- [101] J.Y. Cognard, L. Sohier, and P. Davies. A modified Arcan test to analyze the behavior of composites and their assemblies under out-of-plane loadings. *Composites Part A: Applied Science and Manufacturing*, 42(1):111–121, 2011.
- [102] P. Zhang, Z. Gao, Q. Zhang, A. Khattab, and G. Li. Fracture behavior characterization of arcan polycaprolactone based polymer composites prepared by polymerization induced phases separation. *Polymer Composites*, 2018.
- [103] C.F.A.I. Toray. T700S Data sheet No. CFA-005.
- [104] E. Totry, J.M. Molina-Aldareguía, C. González, and J. Llorca. Effect of fiber, matrix and interface properties on the in-plane shear deformation of carbon-fiber reinforced composites. *Composites Science and Technology*, 70(6):970–980, 2010.
- [105] Z. Hashin. Failure Criteria for Unidirectional Fiber Composites. *Journal of Applied Mechanics*, 47(2):329, 1980.
- [106] E. Totry, C. González, and J. Llorca. Failure locus of fiber-reinforced composites under transverse compression and out-of-plane shear. *Composites Science and Technology*, 68(3-4):829–839, 2008.
- [107] S. Rabinowitz, I.M. Ward, and J.S.C. Parry. The effect of hydrostatic pressure on the shear yield behaviour of polymers. *Journal of Materials Science*, 5(1):29–39, 1970.
- [108] J.C. Halpin and J.L. Kardos. The Halpin-Tsai equations: A review. *Polymer Engineering and Science*, 16(5):344–352, 1976.
- [109] T.W. Clyne. A compressibility-based derivation of simple expressions for the transverse Poisson’s ratio and shear modulus of an aligned long fibre composite. *Journal of Materials Science Letters*, 9(3):336–339, 1990.
- [110] R.J. Asaro and A. Needleman. Texture development and strain hardening in rate dependent polycrystals. *Acta Metallurgica*, 33(6):923–953, 1984.
- [111] A. W. Christiansen, E. Baer, and S. V. Radcliffe. The mechanical behaviour of polymers under high pressure. *The Philosophical Magazine: A Journal of Theoretical Experimental and Applied Physics*, 1971.
- [112] J. A. Sauer. Deformation, yield and fracture of polymers at high pressure. *Polymer Engineering & Science*.
- [113] K. Takahashi, Y. Kon, T. Yano, and T.-W. Chou. Effect of fiber waviness on elastic moduli of fiber composites. *Sen’i Gakkaishi*, 43(7):376–383, 1987.

-
- [114] L. E. Govaert, P. H. M. Timmermans, and W. A. M. Brekelmans. The influence of intrinsic strain softening on strain localization in polycarbonate: Modeling and experimental validation. *Journal of Engineering Materials and Technology*, 1999.
- [115] R. H. J. Peerlings, R. de Borst, W. A. M. Brekelmans, and J. H. P. de Vree. Gradient enhanced damage for quasi-brittle materials. *International Journal for Numerical Methods in Engineering*, 1996.

Acknowledgements

First of all I would like to thank Vikram and Joris, for accepting me as a PhD student and guiding me through my PhD project. I enjoyed working with you and I certainly learned a lot from you, both scientifically and personally. A special thank you also goes out to Lucas Meza for a smooth and fun collaboration on the 3DNOOBED studies. I would also like to thank the user committee members for their fruitful discussions during the project meetings and making this project possible.

I enjoyed being a member of the Mechanics of Materials group at the mechanical engineering department and I would like to thank all the staff members for their help whenever I needed it. A thank you goes out to Leo for letting me (ab)use the cluster and the simulation licenses, without ever stopping my simulations.

It was a privilege to spend four years in room 4.13. It may not always have been the most productive office, but it certainly the most eccentric office. I would like to thank Stefan, Maqsood, Siavash, Sandra, Rody, Mohsen, Vahid, Steyn, Salman, Mirka and Luv for making it such a nice place to work. Thank you Jeroen for taking the cover photograph of the thesis.

I have great appreciation for my friends and family for actually taking my mind off work and always being there for me. I would like to finish by thanking my wife Marlies and my daughter Julia. You can not imagine the amount of happiness you bring to my life and how proud I am to be your husband and father.

Curriculum Vitae

Jim Schormans was born on 23-7-1988 in Heerlen, The Netherlands. After finishing his pre-university education in 2006 at the Eijkhagen college in Landgraaf, The Netherlands he studied Mechanical Engineering at the Eindhoven University of Technology, receiving his bachelor's degree in 2010. In the year between his bachelor's and master's studies, he was the technical manager of the formula student racing team of the Eindhoven University of Technology. In 2011 he continued his masters's study and as a part of his master track he performed an internship at Philips research. In May 2014 he received his Master's degree on the thesis: "Modeling Hertzian cone cracks with a partition of unity based cohesive zone model" under the supervision of dr. ir. J.J.C. Remmers and prof. V.S. Deshpande. Under the same supervisors, he started his PhD project in the mechanics of materials group in 2014. This research is part of the HTSM-STW project "Physics based modeling of failure in textile composites under complex stress states" (project number 13322). The results of his PhD project are presented in the thesis: "Deformation and failure of woven and 3D composites".